Novel Fabrication Strategies for Multifunctional Hydrogel Particles

A dissertation submitted by

Christina L. Lewis

in partial fulfillment of the requirements for the degree of

Doctor of Philosophy
in
Chemical Engineering

TUFTS UNIVERSITY

May 2011

ADVISER:

PROFESSOR HYUNMIN YI

Abstract

Three fabrication strategies for poly (ethylene glycol) (PEG) -based microparticles and their utility for exploiting the advantages of viral nanotemplates and DNA oligonucleotides are presented in this dissertation:

1. *Nucleic Acid Hybridization Assembly of Viral Nanotemplates on Microparticles*

   A flow lithography technique known as stop-flow lithography (SFL) was used to fabricate microparticles with discrete regions for sample identification and patterned assembly of functionalized tobacco mosaic virus (TMV) nanotemplates. TMV nanotemplates were programmed with linker DNA, complementary to the probe DNA in the assembly region of the microparticles. The hybridization-based assembly yielded specific, programmable, and spatially selective assembly of TMV nanotemplates on encoded hydrogel microparticles and demonstrates a novel high throughput route to create multiplexed and multifunctional viral-synthetic hybrid microentities.

2. *Microparticles Containing Functionalized Viral Nanotemplates*

   Functionalized viral assemblies were uniformly distributed throughout hydrogel microparticles by direct embedding with a microfluidic flow-focusing device and UV photopolymerization. Fluorescence and confocal

microscopy images showed uniform distribution of the TMV nanotemplates. Microparticles containing TMV-templated palladium (Pd) nanoparticles exhibited catalytic activity for the dichromate reduction reaction. The results reveal that microparticles provide a stable and simple-to-handle carrier for TMV nanotemplates and address a critical challenge of 3D assembly of functionalized viral hybrid nanomaterials.

3. *DNA-Conjugated Microparticles via Replica Molding (RM)*

DNA-conjugated microparticles were fabricated using a soft-lithographic batch processing-based technique, known as RM. A humidity controlled environment was found to minimize the negative effects of rapid evaporation and ensure uniformity across batch fabricated microparticles. It was also found that PEG-diacrylate concentration effects hybridization and target DNA penetration depth. Additionally, the effects of probe DNA and photoinitiator concentration on target DNA hybridization and particle formation were examined. Finally, sequence-specificity and responsiveness down to single nanomolar concentrations was determined. The results demonstrate a simple, robust, and scalable batch procedure for manufacturing highly uniform hybridization assay particles in a well-controlled manner. Additionally, this work illustrates a novel batch fabrication technique, which offers advantages over the traditional, continuous (microfluidic) fabrication methods for DNA-conjugated microparticles.

Together, these results identify multiple simple and well-controlled fabrication strategies for PEG-based, functional hydrogel microparticles, which contribute to the advancement and application of functional biomaterials.

ACKNOWLEDGMENTS

Throughout this endeavor, I have been surrounded by special mentors, colleagues, friends, and family, who have provided inspiration, support, and guidance to make this work possible. I would like to first acknowledge my dissertation adviser, Professor Hyunmin Yi, for continuous encouragement, patience, and motivation. I would also like to acknowledge my dissertation committee members, Professor David Kaplan, Professor Pat Doyle, and Professor Dan Ryder, for constructive criticism and guidance. I am grateful for the support of the Yi lab members, especially Amy Manocchi, Cheryl Goldwasser, Jennifer Rego, Cuixian Yang, and Jihae Sohn. I would also like to acknowledge all of my family and in-laws, most importantly, my husband, Brian, who has provided constant encouragement and demonstrated everlasting patience throughout this entire journey. Finally, I would like to acknowledge Orin Mei, for offering a new perspective in the final three years of this work.

TABLE OF CONTENTS

LIST OF FIGURES

LIST OF TABLES

1 INTRODUCTION

The objective of the work presented in this dissertation was to fabricate functional hydrogel microparticles in a high-throughput, well-controlled, and robust manner. A variety of methods have been established for the fabrication of hydrogel microparticles bearing unique, and mostly customizable features, such as chemical anisotropy, complex shapes, core/shell structures, magnetic capabilities, or thermosensitivity [1-4]. The methods range from batch formats, such as photolithography or template-based printing to continuous formats, such as microfluidics [2, 5]. Despite these advances there still exists a critical need for rapid and well-controlled routes to fabricate multifunctional microparticles. The focus of this work was to harness the useful characteristics of hydrogel microparticles following batch and continuous fabrication while also enhancing their functionality with high capacity viral nanotemplates and DNA oligonucleotides.

Assembling viral nanotemplates with hydrogel microparticles in a programmable, selective, and facile manner under mild conditions is a challenge. Individually, viral nanotemplates and hydrogel microparticles each have unique features, as described in Sections 1.3 and 1.2, respectively. However, assembly of these individual components into a structured hierarchical arrangement provides means to exploit their individual advantages together as one unit. This challenge is addressed in this dissertation by hierarchically assembling Tobacco Mosaic

Virus (TMV) nanotemplates onto hydrogel microparticles via nucleic acid hybridization (Chapter 2). Patterned assembly of TMV via nucleic acid hybridization has been accomplished previously on chitosan surfaces [6] and in a microarray format [7], but this work is the first achievement of TMV nanotemplate assembly on hydrogel microparticles in a programmable and selective manner, to our knowledge.

Encapsulation of functionalized viral nanotemplates in a 3D hydrogel network is also a challenge. Packaging functionalized viral nanotemplates in a 3D, high capacity format provides opportunity for improved kinetics and reactivity with the components of interest, such as metal nanoparticles. The challenge arises, in part, from aggregation and stability issues with metal [8] and viral [9] nanoparticles. In this dissertation, this challenge is addressed by directly embedding functionalized TMV nanotemplates in hydrogel microparticles with a microfluidic fabrication procedure (Chapter 3). Fluorescence and confocal microscopy results confirm the distribution of the functionalized TMV nanotemplates throughout the hydrogel network of the microparticles. Microparticles containing metalized viral nanotemplates provide catalytic activity for the dichromate reduction reaction.

Others have indirectly contributed to this challenge. Nam et al. [10] have fabricated porous polymer microgels containing genetically engineered M13 virus scaffolds as nanostructured templates to function as photocatalysts for light-driven water oxidation. However, these virus scaffolds were functionalized after they were encapsulated in the microgels, presenting a significant challenge of

determining whether or not the functionality was specific to the virus or non-specifically conjugated to both the virus and microgel. Li et al. [11] assembled TMV and M13 bacteriophage with polymers to form 3D core-shell composite structures. While this self-assembly procedure yielded 3D composite structures, it is not high-throughput and the viruses are not functionalized. Directly embedding functional viral nanotemplates in hydrogel microparticles with a microfluidic procedure provides a significant contribution to the existing challenge of encapsulation of functionalized viral nanotemplates while also exploiting the utility of hydrogel microparticles.

While certain limitations exist with microfluidic fabrication methods of hydrogel microparticles, such as the requirement of rapid polymerization without deformation, liquid properties (e.g. viscosity) bound by the need for consistent flow, or adherence to channel walls [12-14], soft-lithographic fabrication of polymeric structures via replica molding (RM) has gained substantial attention due to many inherent advantages rising from the batch-processing based nature of the fabrication procedure [14-16]. These advantages include simple, robust, and inexpensive procedures [15] as well as scalability [17] and reliable duplication of complex structures with nanometer resolution [15, 16]. An alternative batch-processing based procedure for hydrogel particle fabrication is photolithography, which provides high-throughput fabrication with well-defined shapes down to the submicrometer level [17]. Meiring et al. [18] have demonstrated fabrication of shape-encoded hydrogel particle biosensor array platforms using photolithography. While offering straightforward and well-established

procedures, equipment cost and cumbersome recovery for photolithographic fabrication presents hurdles for simple and robust routes to produce particles. A majority of recent studies using a similar soft lithographic RM technique, known as particle replication in nonwetting templates (PRINT), have focused mainly on nanoscale fabrication of polymeric hydrogel particles in an effort to harness the simplicity and robustness of the RM procedure for drug delivery applications [19-22]. However, fabrication of uniform probe DNA-conjugated hydrogel particles with dimensions relevant to high throughput biosensing (i.e. 10-100 μm) via RM has not been demonstrated. Thus, a novel batch-processing based fabrication technique for DNA-conjugated microparticles using the well-known RM technique is also presented in this dissertation (Chapter 4), offering multiple advantages over the traditional microfluidic fabrication methods for DNA-conjugated microparticles.

Potential applications of the functional hydrogel microparticles presented in this dissertation include high-throughput biosensing, catalysis, or environmental remediation. This introductory chapter describes the benefits and utility of hydrogel substrates in the context of multiplexed assays. A description of the broad applications and features of hydrogel microparticles, viral-based nanotemplates, and DNA oligonucleotides is also presented. An overview of this dissertation is provided at the end of this chapter.

1.1 SOLID AND HYDROGEL SUBSTRATES FOR MULTIPLEXED ASSAYS

1.1.1 Solid Substrates for Planar and Suspension Arrays

Detection of multiple target molecules from a complex mixture, known as multiplexed assays, is traditionally carried out in two array formats: planar or suspension. As shown in Figure 1.1, planar arrays consist of high density microspots of capture molecules on a rigid surface at spatially discrete locations while suspension arrays consist of particle-based supports to which probe molecules are covalently coupled [23]. Identification of planar arrays relies on x,y positions on their platform where internal fluorophores have traditionally been used to identify suspension array samples [24]. Following target hybridization, chemiluminescent reporter molecules are traditionally used to provide signal, which is then analyzed to quantify target binding [25, 26]. Electrochemiluminescence has also been used to quantify target binding in planar arrays [27]. Similarly, fluorophore labels for targets followed by fluorescence sorting with quantification are used to measure target binding for suspension arrays [23, 24]. Label-free approaches, such as surface plasmon resonance (SPR) or microcantilevers, are also use to quantify target binding for suspension arrays [28].

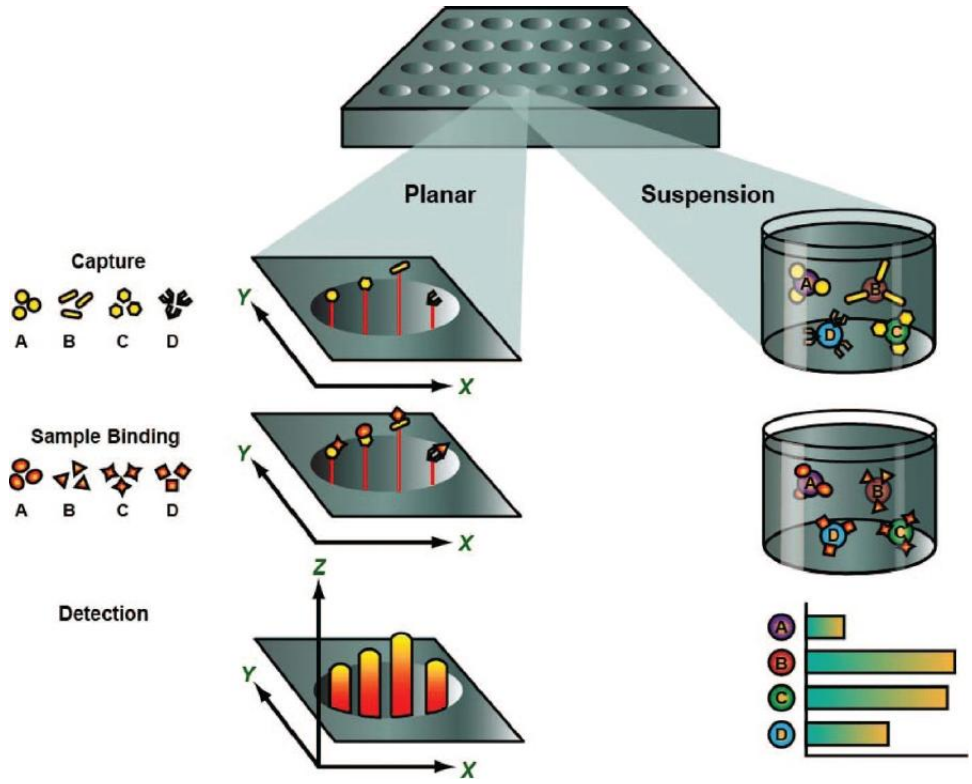

Figure 1.1. Differences between planar and suspension array formats. This figure was reproduced from Ellington et al. [23]. Planar arrays formats consist of spotted capture molecules on a rigid surface at spatially discrete locations while suspension formats consist of particle-based supports to which capture molecules are covalently coupled.

The traditional platform for planar arrays is a solid surface such as a glass slide, silicon wafer, or quartz wafer [29]. Advantages of these platforms are minimal background fluorescence and stability through stringent washes. GeneChips by Affymetrix are widely known commercially available in situ-synthesized, high-density planar arrays that use oligonucleotide probes. Roche NimbleGen and Agilent Technologies also manufacture high-density oligonucleotide planar arrays. While these technologies have demonstrated success in the microarray field [30], planar arrays on solid platforms can pose

critical limitations for rapid and cost-efficient assays, such as long incubation times, low probe titers, and extensive equipment and software needs [31].

Commercially available particle-based suspension arrays, such as Luminex xMAP^{TM} liquid array technology [24], consist of solid polystyrene bead or microsphere supports. These 3D platforms offer high throughput biosensing with low sample volume and rapid detection via scanning [29]. The suspension arrays also have increased precision over planar formats as a result of multiple independent measurements within each microsphere population [23]. While particle-based suspension arrays offer advantages over planar arrays, in addition to simplicity, affordability and clear success within the field of microarrays (in 2008 Luminex obtained FDA clearance for first infectious-disease suspension bead array), their solid bead substrates do interfere with the kinetics of hybridization between the probe and target molecules [32-34].

1.1.2 Hydrogel Substrates for Planar and Suspension Arrays

More recently, hydrogel substrates have been investigated as the base platform for both planar and suspension arrays [18, 26, 34-37]. The motivation for using hydrogel substrates over solid substrates was to address the low signal levels observed when probe molecules were confined to a solid substrate surface and to seek improved kinetics of hybridization between the probe and target molecules. The loss of biomolecule integrity as a result of stringent immobilization procedures in addition to a rigid environment not conducive for capture-target interactions has also been a large concern with solid substrates as microarray platforms [29, 35]. The interference of glass substrates affects both

thermodynamic and kinetic characteristics at the formation of hybridized complexes [34].

Significant effort has been devoted to investigating advantages of hydrogel substrates over solid substrates. The 3D immobilization volume of hydrogel substrates provides increased capacity of capture molecules and a hydrophilic environment, which, together, lead to improved assay sensitivity in comparison glass substrates [25]. Specifically, polyacrylamide gels were found to provide 100 times increased greater capacity for immobilization than 2D glass supports [38]. Fluorescence signals and mutation discrimination efficiency is also higher for gels in comparison to surface oligonucleotide microchips despite slower hybridization kinetics [34]. Additionally, molecular interactions between gel immobilized probe and target oligonucleotides are similar to those in solution while hydrogels provide nanoenvironments, which increase complex formation between interacting biomolecules [39, 40]. Finally, storage of glass-based oligonucleotide microchips at room temperature was 2 months while gel-based microchips lasted for 1 year under the same conditions. In summary, hydrogel platforms offer many advantages over solid substrates for multiplexed assays. These features are further examined and utilized in the context of hydrogel microparticles for the work presented in this dissertation.

1.2 HYDROGEL MICROPARTICLES

1.2.1 Advantages and Utilities

Hydrogel microparticles offer readily usable and stable 3D networks for a wide range of functional material applications. In contrast to 2D surfaces, the highly porous networks of hydrogel microparticles can improve biomolecular interactions between the probe molecules and targets of interest [39] and offer a hydrophilic environment with more favorable solution kinetics than 2D surfaces [40]. For nucleic acid hybridization-based assays, hydrogel microparticles feature the benefits described in Sections 1.1.1 and 1.1.2 for particle-based platforms and hydrogel substrates, respectively. These advantages include higher immobilization capacities of probe molecules, improved limits of detection, signal-to-noise ratios, sensitivity, selectivity, and rapid hybridization [32, 41, 42]. Beyond nucleic acid hybridization-based assays, hydrogel microparticles conjugated with DNA may be applied in a variety of other applications, which exploit the utility of DNA oligonucleotides, as described in Section 1.4. The ability to customize specific microparticle features, such as magnetic capabilities [4, 43], further expands their potential applications. For example, particles containing magnetic nanoparticles may provide an alternative means for separation from bulk solution, patterning, or self-assembly. Additionally, hydrogel microparticles may also serve as a stabilizing platform for viral or metal nanoparticles, which tend to suffer from stability and aggregation problems [8, 9].

1.2.2 Radical Chain Photopolymerization

Photoinitiated curing with UV irradiation is commonly employed as part of hydrogel microparticle fabrication procedures. The main advantages of photoinitiated curing are the rapid polymerization rates possible with intense illumination and the spatial resolution of the polymerization, which only occurs within the regions exposed to UV [44]. The ability to control the initiation rates through the source of radicals, light intensity, and temperature in addition to the regions for polymerization enables production of polymer materials having tailored properties. One limitation of photopolymerization is the penetration of light through a thickness of material. However, for the hydrogel microparticles considered in this work, the maximum particle thickness is 50 μm, so the attenuation of UV light through the microparticles is considered minimal [45, 46]. Two major class of UV-curable resins, differing by their polymerization mechanism are: 1) photoinitiated radical polymerization of acrylates and 2) photoinitiated cationic polymerization of expoxides and vinyl ethers [45]. Almost all monomers containing a carbon-carbon double bond undergo radical polymerization while cationic polymerization is limited to those monomers or prepolymers with electron-releasing substituents, such as alkoxy, phenyl, vinyl, and 1,1-dialkyl [47]. Cationic polymerizations are not sensitive toward atmospheric oxygen where radical polymerization reactions are inhibited by oxygen, which reacts with the radical species to form chain terminating peroxide molecules [45, 48]. Oxygen inhibition is useful for some microparticle fabrication techniques [12, 13, 49], while it is undesirable in others, such that an

environment free of oxygen is used to fabricate particles [19]. The base polymerization mechanism for each of the three microparticle fabrication techniques presented in this dissertation is radical chain photopolymerization. The reaction mechanism and governing kinetic equations for radical chain photopolymerization is described in the remainder of this subsection.

Radical chain polymerization is a chain reaction consisting of a sequence of three events: initiation, propagation, and termination. When an inhibitor is present, such as oxygen described above, an inhibition event should also be considered. Photoinitiated polymerization reactions occur when radicals are produced by UV light irradiation of the reaction system [47]. A general reaction mechanism illustrating these four sequences of events with photoinitiator, I, radical species, R, monomer or prepolymer, M, and inhibitor, Z, is shown in Figure 1.2. Each initiator molecule forms two radical species following exposure to UV light. The rate constants for each reaction are represented by k with a subscript specifying the individual reactions.

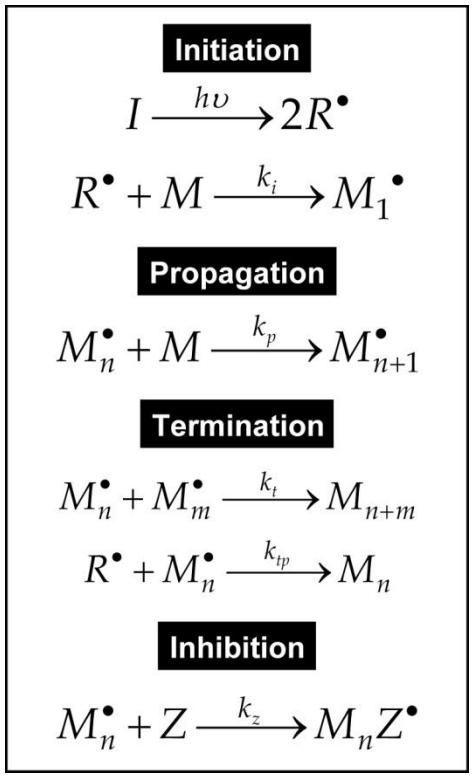

Figure 1.2. General reaction mechanism for photoinitiated radical chain polymerization.
The reaction occurs through a sequence of four events: initiation, propagation, termination, and inhibition. The chemical species, which are part of these events include photoinitiator, I, radical, R, monomer or prepolymer, M, and inhibitor, Z. Each initiator molecule forms two radical species following exposure to UV light ($h\upsilon$). The rate constants for each reaction are represented by k with a subscript specifying the individual reactions.

The initiation event involves two reactions. The first initiation reaction forms two radical species via photolysis. The second initiation reaction involves the addition of a radical species to the first monomer or prepolymer molecule to produce the chain-initiating radical, $M_1^{\bullet}$. During propagation, successive additions of monomer or prepolymer molecules forms growing polymer chains identical to the previous, but larger by one monomer unit. Propagation with growth of the chain to high polymer proportions takes place rapidly with rate constant (k_p) values ranging between 10^2 and 10^4 L mol^{-1} s^{-1} [47]. At termination,

the propagating polymer chain stops growing. Bimolecular termination may occur by coupling, to form one chain or disproportionation, to form two chains. For coupling, propagating radical chains react with each other. For disproportionation, a hydrogen radical that is beta to one radical center is transferred to another radical center to form two polymer molecules, one saturated and one unsaturated [47]. The polymerization kinetics for crosslinked systems is not strongly influenced by the termination mode [50], so the bimolecular termination modes are lumped into one reaction with rate constant, k_t, as shown in Figure 1.2. A second termination mechanism is primary radical termination, where a primary radical reacts with a growing polymer chain to form dead polymer. The rate constant for this reaction, k_{tp}, differs from k_t because both reactions have different chemistries and different species mobilities [50]. Typical termination constants range between 10^6 and 10^8 L mol^{-1} s^{-1} [47], which is order of magnitudes greater than propagation rate constants. During inhibition, an inhibitor, such as oxygen or an intentionally added inhibitor, reacts with a growing polymer chain to form a relatively unreactive species. It is important to note that an inhibited growing polymer chain, $M_nZ^{\bullet}$, may react with monomer or prepolymer to reform an actively growing polymer chain, but the rate of this reinitiation reaction is significantly lower (orders of magnitude) than the rate of initiation, k_i. Therefore, this specific reaction has not been accounted for as a third reaction within the mode of initiation. Additionally, another assumption in the reaction mechanism is that the inhibited growing polymer chain terminates without regeneration of inhibitor, Z.

The rate of polymerization is equivalent to the rate of monomer or prepolymer disappearance and is governed by the rates of initiation, R_i, and propagation, R_p, as shown in Equation 1.

Equation 1

$$\frac{-d[M]}{dt} = R_i + R_p$$

Since the number of monomer or prepolymer molecules reacting in the initiation step is much less than the number in the propagation step, the rate of polymerization may be closely approximated by assuming $R_p >> R_i$, so the rate of polymerization may be represented by the rate of propagation, as shown in Equation 2. The monomer or prepolymer concentration is represented by [M] and the concentration of all chain radicals is represented by [$M^{\bullet}$].

Equation 2

$$\frac{-d[M]}{dt} = R_p = k_p[M^{\bullet}][M]$$

Applying the steady-state approximation eliminates [$M^{\bullet}$] from Equation 2 as radical concentrations are difficult to measure. This assumption implies that the rate of change of the radical concentration is zero during the course of the polymerization, such that the rates of initiation, R_i, and termination, R_t, of radical species are equivalent, as shown in Equation 3. The use of the factor 2 in this initiation and termination rate equation follows a generally accepted convention for reactions destroying radicals in pairs [47].

Equation 3

$$R_i = R_t = 2k_t[M^\bullet]^2$$

Rearrangement of Equation 3 by solving for [M$^\bullet$] in terms of R_i, and then substituting the resulting equation into Equation 2 provides the rate of polymerization, R_p, in terms of rate constants for propagation, k_p, and termination, k_t, the rate of initiation, R_i, and monomer or prepolymer concentration, [M], as shown in Equation 4.

Equation 4

$$R_p = k_p[M]\left(\frac{R_i}{2k_t}\right)^{1/2}$$

The rate of initiation, R_i, is a function of the quantum yield of the photoinitiator, ø, the molar extinction coefficient, ε, concentration of photoinitiator, [PI], and light intensity at depth z, I_z, as shown in Equation 5. The factor of 2 in this equation accounts for the production of two radicals for each initiator molecule undergoing photolysis.

Equation 5

$$R_i = 2\phi\varepsilon[PI]I_z$$

I_z is a volumetric light intensity at depth z, as shown in Equation 6, and is determined by considering the Beer-Lambert law and integrating the surface area intensity of adsorbed light at distance z, as described by Odian and Lee et al. [47, 51]. In this equation, I_o represents the incident light intensity at the outer surface of the reaction system.

Equation 6

$$I_z = I_o(10^{-\varepsilon[PI]z})$$

Substituting Equations 5 and 6 into Equation 4 provides an equation for the rate of photoinitiated radical chain polymerization at a layer at depth z from the surface of a reaction system, as shown in Equation 7. Similarly, this equation represents the theoretical rate of polymerization, in terms of the pertinent variables, for forming hydrogel microparticles from the base prepolymer solutions for each of the three fabrication techniques described in this dissertation. As mentioned earlier in this subsection, attenuation of UV light through the microparticles is considered minimal with the maximum microparticle thickness of 50 μm. Thus, the rate of photoinitiated radical chain polymerization for the hydrogel microparticles described in this dissertation may be assumed constant if the fabrication procedures were carried out in an oxygen free environment.

Equation 7

$$R_p = k_p[M]\left[\frac{\phi\varepsilon I_o[PI](10^{-\varepsilon[PI]z})}{k_t}\right]^{1/2}$$

However, the fabrication procedures were not carried out in an oxygen free environment and the derivation of Equation 7 does not include the kinetics of oxygen inhibition. It is well-known that the presence of atmospheric oxygen effects the polymerization kinetics within PDMS microfluidic devices [46] as well as for microscale patterning of hydrogels, such as microcontact printing [52]. For fabrication of hydrogel microparticles within PDMS microfluidic devices or micromolds, both of which are used for the work presented in this dissertation, oxygen affects the photopolymerization via diffusion within the PDMS devices. Thus, the degree of oxygen inhibition is not the same throughout the cross-section of the hydrogel microparticles. The outer surfaces of the microparticles have the greatest exposure to oxygen while the interior regions have less to minimal exposure. The inhibitory effects of oxygen on the polymerization of hydrogel microparticles are non-uniform and cannot be accounted for by the preceding derivation of the theoretical rate of photoinitiated radical chain polymerization, R_p.

Others have specifically examined the effects of oxygen inhibition on photopolymerization of thin films [53, 54], within microfluidic devices [46], and for microscale patterning of hydrogels [52]. These studies suggest that oxygen inhibition significantly affects the polymerization kinetics at a depth of approximately 10 μm beginning at the surface exposed to oxygen. Based on these findings from others, the interior regions (excluding the 10 μm exterior shell) of the hydrogel microparticles described in this dissertation do not suffer from

oxygen inhibition. Yet, it is important to note that oxygen inhibition is important for the microfluidic fabrication of the hydrogel microparticles described in Chapters 2 and 3 of this dissertation, where the presence of oxygen provides a non-polymerized lubricating layer within the microfluidic device, enabling the microparticles to flow. This lubricating layer is also described by others in more detail [13, 46]. Additionally, Chapters 2 and 4 of this dissertation describe how hydrogel mesh size of microparticles is important with regard to the assembly of viral nanotemplates on microparticles and also the penetration of target DNA within the microparticles for hybridization with probe DNA. The results presented in these chapters show that viral nanotemplate assembly and target DNA penetration occur only within the outer 10 μm region of the microparticle surfaces, where oxygen inhibition affects the microparticle polymerization kinetics and consequently, their physical features, such as the hydrogel mesh size of the exterior portion of the microparticles.

1.2.3 General Prepolymer Solution Composition

The prepolymer solution components used for each of the hydrogel microparticle fabrication strategies presented in this dissertation are listed in Table 1.1. The base component of the crosslinked hydrogel microparticles is poly (ethylene glycol) (PEG), well known for its hydrophilic, biocompatible, and non-fouling characteristics [55]. In its prepolymer form at a molecular weight (MW) of 700, and with two double bonds per molecule, poly (ethylene glycol) diacrylate (PEG-DA) crosslinked the hydrogel microparticles in the presence of the photoinitiator known as Darocur 1173. Non-reactive PEG at a MW of 200 was

also used in some of the prepolymer solutions, in part, to assist with the solubility of the photoinitiator. For the replica molding work described in Chapter 4, hybridization signals were significantly higher when non-reactive PEG 200 was included in the prepolymer solution. DNA containing a methacrylate modification at the 5' end was included in the prepolymer solution so that the methacrylate copolymerized with the PEG-DA prepolymer to chemically conjugate DNA within the hydrogel matrix. This DNA modification and the methacrylate copolymerization reaction is described further in Section 1.2.4. Tris-EDTA buffer was included in the prepolymer solution based on the work of Pregibon et al. [37], where DNA hybridization signals were higher when this buffer was included in the prepolymer solution for hydrogel microparticles.

Table 1.1. Prepolymer Solution Composition for PEG-Based Hydrogel Microparticles.

Prepolymer Solution Component	Chemical Structure	Total Volume (%)
Poly (ethylene glycol) diacrylate (PEG-DA), MW 700	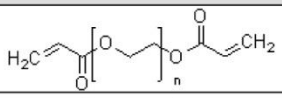	20-50
Poly (ethylene glycol), MW 200 (PEG 200)	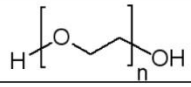	0-10
2-Hydroxy-2-methylpropiaphenone, Darocur 1173, (Photoinitiator)	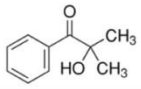	2-5
Probe DNA with Acrydite™ modification at 5' end	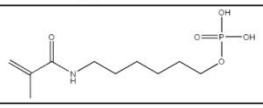	0-10
Tris-EDTA (TE) Buffer	N/A	28-58

*Images were reproduced from the product image provided by the manufacturers [56, 57].

Upon exposure to UV light, Darocur 1173 forms two radical species as shown in Figure 1.3. One of the radicals is a benzoyl and the other is a hydroxyalkyl. The benzoyl radicals are believed to have higher reactivity to initiate the polymerization of acrylate monomers, where the hydroxyalkyl radicals are believed to have higher reactivity to initiate the copolymerization of vinyl ethers and maleate monomers based on studies of the efficiencies of these specific radical species [58, 59].

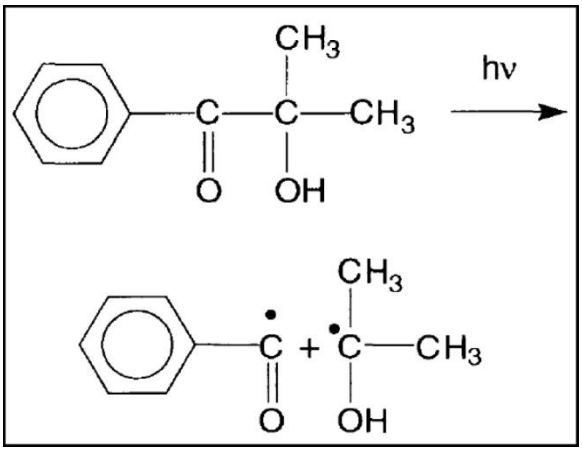

Figure 1.3. Radical species of photoinitiator, Darocur 1173.
This figure was adapted from Decker et al. [58].

A crosslinking polymerization reaction scheme of a benzoyl radical with a diacrylate monomer or prepolymer, such as PEG-DA, is shown in Figure 1.4. Acrylates are considered the most reactive monomers. Their high crosslink densities show well-designed physical properties depending on the length and chemical structure of the crosslink segments [44]. A MW of 700 for PEG-DA was chosen for this work because it was found to have faster reaction kinetics and

significantly less background signal in comparison to lower MW PEG-DA prepolymers for fabrication of nucleic acid hybridization-based hydrogel microparticles [37].

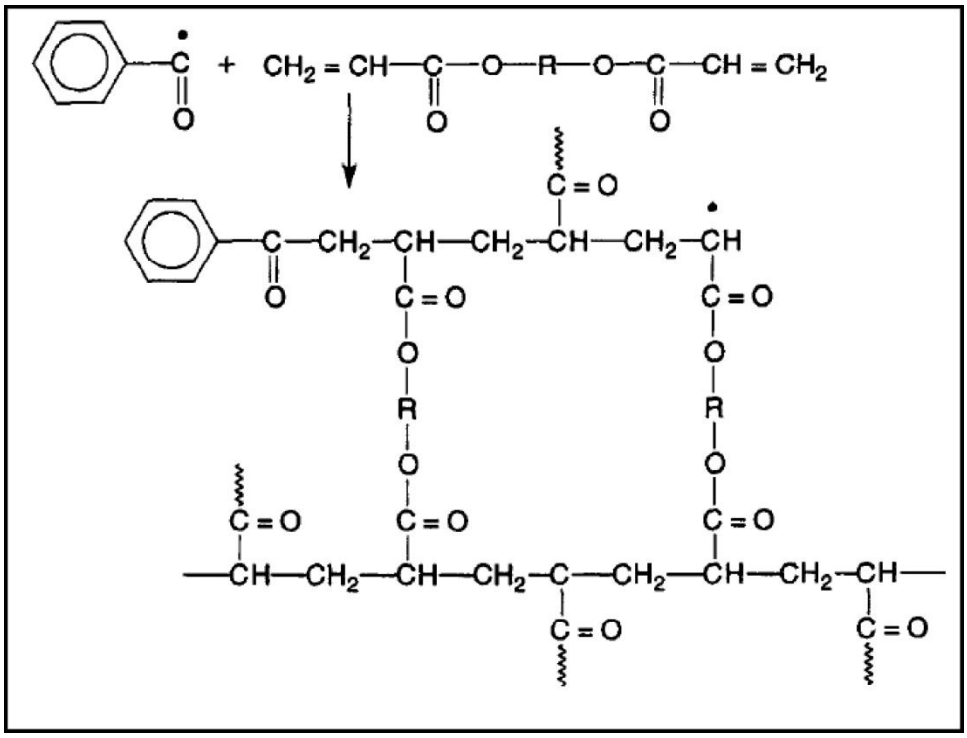

Figure 1.4. Crosslinking polymerization of a benzoyl radical with a diacrylate monomer or prepolymer.
This figure was adapted from Decker [44] and illustrates the crosslinking polymerization of the PEG-based hydrogel microparticles from PEG-DA prepolymer, following reaction with the benzoyl radical species from photoinitiator Darocur 1173.

As shown in Figure 1.4, the benzoyl radical of from Darocur 1173 reacts with a diacrylate monomer or prepolymer by opening the π-bond at one of the carbon-carbon double bonds of the diacrylate to form a new radical [47]. Since there are two double bonds for each diacrylate monomer or prepolymer, the polymerization proceeds to form a crosslinked network. If the monomer or

prepolymer contained only one double bond, successive additions of more monomer or prepolymer molecules via radical chain polymerization would create a long linear chain rather than a crosslinked network. It is also important to note that as a result of two available double bonds for a diacrylate monomer or prepolymer, termination may occur via entrapment in addition to coupling or disproportionation, as described previously in Section 1.2.2. Termination by entrapment refers to the trapping of radicals within the polymer matrix and is an issue for highly crosslinked networks [60, 61]. Zhu et al. [62] describe how radical trapping effects the kinetics of propagation for dimethacrylate-based resins.

1.2.4 Conjugating DNA with Hydrogel Microparticles

Hydrogel microparticles may also be chemically conjugated with DNA oligonucleotides via a proprietary small molecule attachment chemistry developed by Mosaic Technologies Inc. For this procedure, an acrylamide group is directly attached to the 5'-end of each oligonucleotide, containing a 6-carbon linker arm, at the time of synthesis using and acrylic-phosphoramidite, referred to as Acrydite^{TM} [63, 64]. The Acrydite-modified DNA may copolymerize with other acryl groups while the DNA oligonucleotide functionality remains available for hybridization with complementary sequences. Figure 1.5 shows the structure of Acrydite-modified DNA and illustrates its ability to copolymerize with acrylamide.

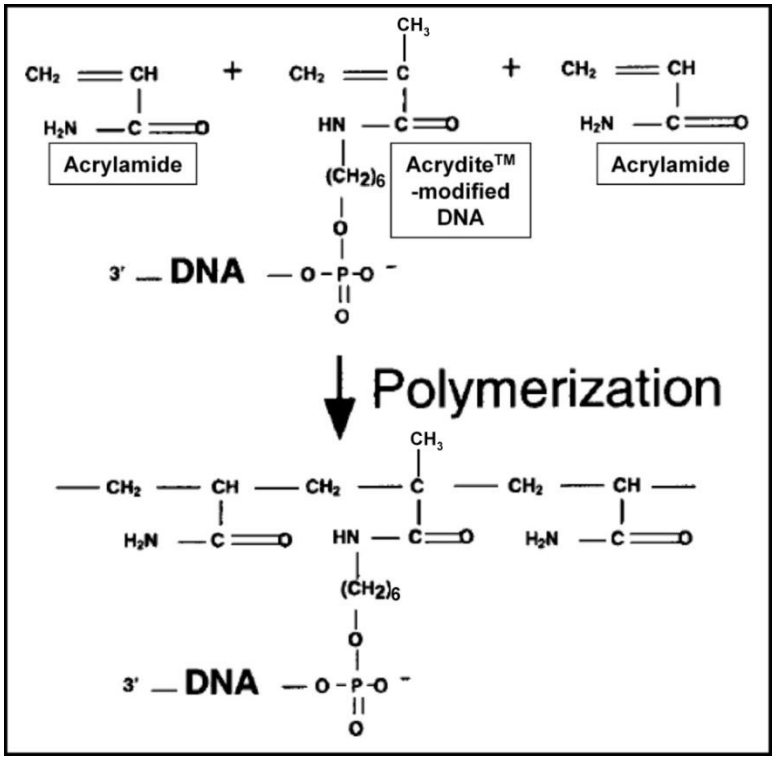

Figure 1.5. Schematic diagram showing the chemical structure of Acrydite™-modified DNA and its copolymerization with acrylamide. This figure was adapted from Rehman et al. [65].

Similarly, Acrydite™-modified DNA was copolymerized within the hydrogel network of the PEG-based microparticles through the free radical chain photopolymerization reaction described in Section 1.2.2. For this, an initiator molecule may react with the carbon-carbon double bond of the Acrydite group to form a reactive DNA species available for copolymerization. Alternatively, a reactive monomer or prepolymer species (chain-initiating species) may react with the carbon-carbon double bond of the Acrydite group for copolymerization within the crosslinked network. Since the Acrydite group is present on only the 5' end of DNA, the 3' end of the DNA is not conjugated within the crosslinked network and remains free and available for subsequent DNA hybridization. This

copolymerization procedure is part of the microparticle fabrication procedures described in Chapters 2 and 4 of this dissertation.

It is important to consider the difference in rates of polymerization between the reactive species of the Acrydite-modified DNA, methacrylate, and the acrylate groups of PEG-DA. As shown in Figure 1.5, the carbon-carbon double bond of Acrydite-modified DNA contains a methyl group where the carbon-carbon double bond of PEG-DA (Table 1.1 and Figure 1.4) does not. This methyl group is the structural difference between methacrylate and acrylate and contributes to significant differences between their respective rates of polymerization. It is well-known that the rate of polymerization, R_p, for methacrylate is much less than that for acrylate. Anseth et al. [66] quantified the difference in R_p over time for methacrylate and acrylate, as shown in Figure 1.6.

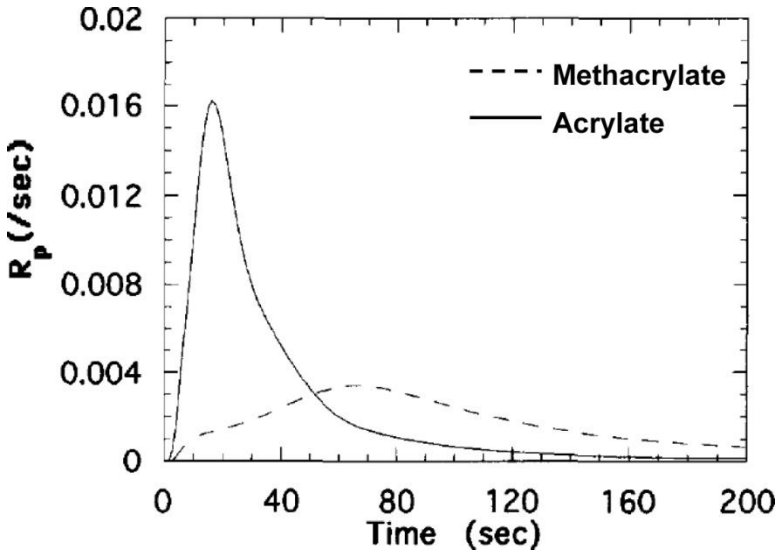

Figure 1.6. Rate of polymerization, R_p, for Methacrylate and Acrylate versus time.
This figure was adapted from Anseth et al. [66].

The difference between the polymerization rates is attributed to the increased reactivity of the acrylate groups and the increased stiffness of the methacrylate polymers [66]. Despite this large difference in rate of polymerization, the results presented in Chapters 2 and 4 of this dissertation show that methacrylate-modified DNA copolymerized with the acrylate prepolymer to chemically conjugate DNA within the hydrogel microparticle matrices. Pregibon and Doyle [67] found that 20 to 25% of Acrydite-modified DNA was incorporated in hydrogel microparticles with 30 to 35 % (v/v) of PEG-DA in the prepolymer solution and fabricated via microfluidics. These results suggest that the amount of probe DNA incorporated in the hydrogel microparticles studied in Chapter 2 of this work is similar as the prepolymer solution composition and fabrication technique were similar as well. However, it is important to note that increasing the probe incorporated in the microparticles may be possible if an alternative base prepolymer was used (e.g. methacrylate) containing a similar rate of polymerization as the Acrydite-modified probe DNA.

Another important consideration is the potential damage of DNA by high intensity UV light. It is well-known that UV can damage DNA and potentially affect its hybridization capability. One report on UVA damage to DNA is by Jiang et al. [68]. The authors reported that after 1.3 MJ/m^2 of UVA (365 nm) irradiation, 90% of supercoiled DNA sample remained supercoiled while 11% relaxed to a circular form. Relaxation of supercoiled DNA is representative of DNA damage by UV. Specifically, one single stranded DNA break will relax its

superhelical structure to a circular form permanently while one double stranded break will open the circular plasmid to a linear form.

For the hydrogel microparticles presented in this dissertation, a radiometer was used to quantify the intensity of UV during the photopolymerization procedures. It was found that the maximum intensity of UVA (365 nm) used to fully polymerize the microparticles was 186 kJ/m^2. This value is several orders of magnitude smaller than that used by Jiang et al. which damaged 11% of a DNA sample. Based on this comparison, we believe that the probe DNA used in this study is not damaged or altered in any way when exposed to UVA during the photopolymerization procedures.

1.3 VIRAL-BASED NANOTEMPLATES

1.3.1 General Structure and Features

Viruses generally consist of coat protein subunits and a nucleic acid, such as DNA or RNA [69]. The coat protein subunits assemble together to form a highly symmetrical and homogenous capsid nanoparticle, which purpose is to protect the nucleic acid that provides the genetic information for replication [70]. These biologically occurring viral nanoparticles are well known for their monodisperse, rigid, and unique structural architectures that have proven to be versatile substrates for the creation of novel materials in applications such as electronics, energy devices, or even pharmaceuticals by coupling to synthetic chemistry or genetic manipulation [70-78]. They have also gained substantial

attention as nanoscale templates for material synthesis [71, 79-86]. Mass production of viruses is generally rapid. They occur in a variety of shapes and sizes, which range from spherical [87-89], filamentous [10, 90, 91], and rodlike [92-94], to engineered assemblies [95, 96], some of which are shown in Figure 1.7.

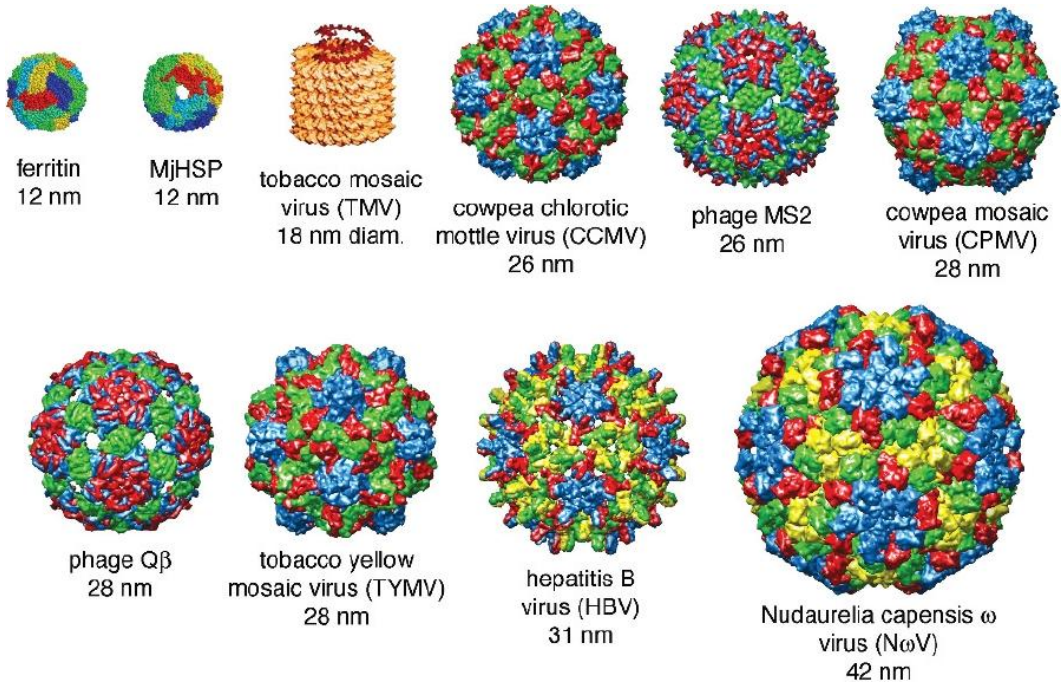

Figure 1.7. Model structures of viral nanoparticles and protein cages.
This figure was reproduced from Manchester et al. [97]. The protein cage examples include ferritin and *Methanococcus jannaschii* heat shock protein (MjHSP). Bacteriaphage capsids MS2 and Qβ are also shown along with several other viral nanoparticles.

Importantly, nanoparticles of viral origin can be fabricated to display a defined number of precisely arranged amino acids or coupling molecules on their surface through coat protein mutagenesis [72, 77], which may be conjugated downstream with peptides, antibodies, or enzymes in well defined spatial arrangements on the

nanometer scale [98-100]. This feature enables a unique advantage by providing decorated nanotemplates with distinctly spaced functional molecules at high density, as shown in Figure 1.8. Additionally, Soto et al. [101] demonstrated that a virus scaffold provided significant signal enhancement and increased assay sensitivity in comparison to commonly used detection methods for microarray assays, suggesting the capability of the high density templating capability of viral nanoparticles.

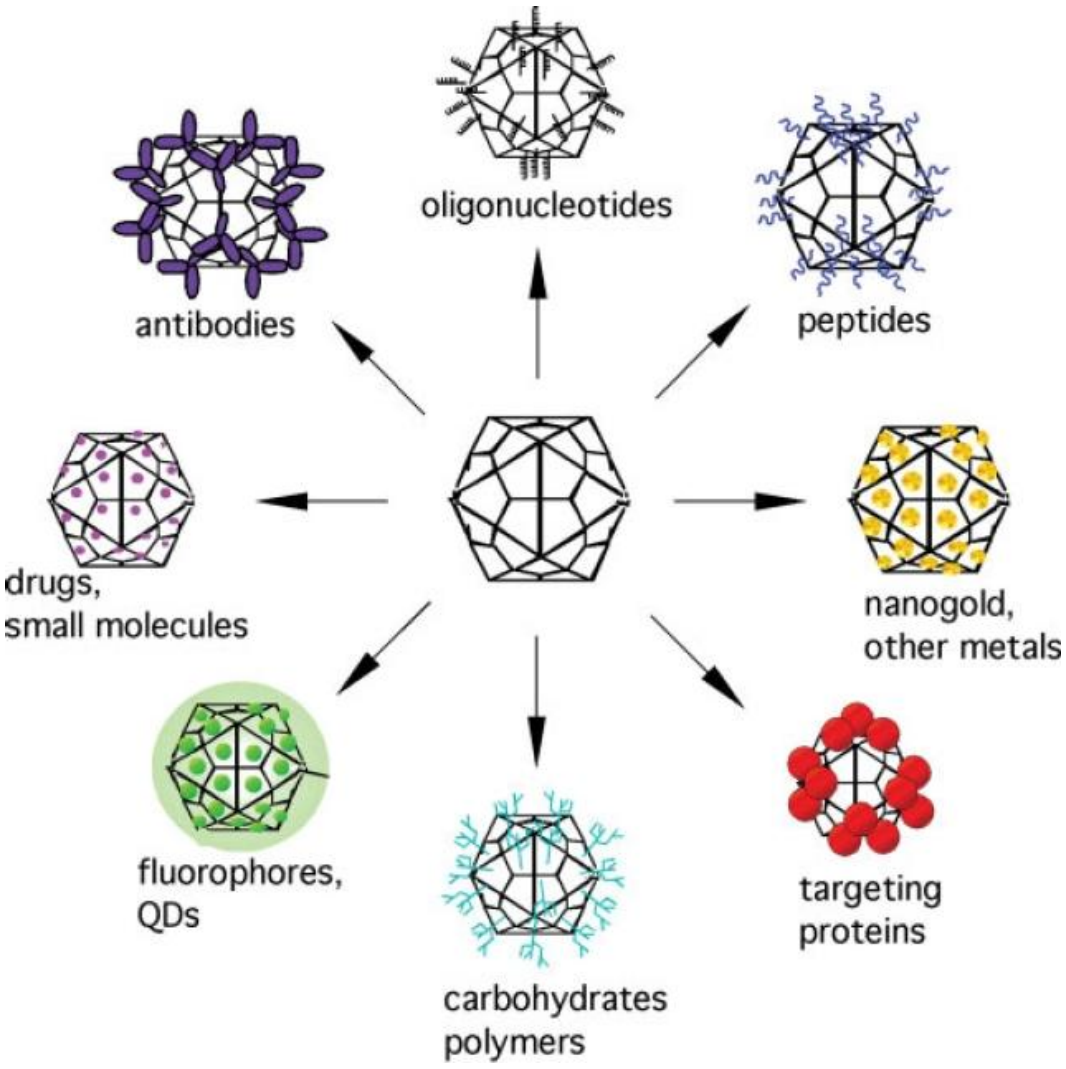

Figure 1.8. Applications of viral nanoparticles.
This figure was reproduced from Singh et al. [77] where the center structure depicts a viral nanotemplate, which may be utilized as a scaffold for a variety of different applications, as illustrated.

1.3.2 Tobacco Mosaic Virus

Tobacco Mosaic Virus (TMV) offers an attractive nanotemplate that provides high density covalent coupling sites with precise nanometer scale spacing. A wild type TMV virion consists of approximately 2130 identical coat

proteins helically wrapped around a 6.4 kb positive strand of genomic mRNA, making it an 18 nm diameter and 300 nm long rigid nanotube with a 4 nm diameter inner channel [102]. TMV also possesses several unique properties as nanotemplates such as simple mass production [103], a well defined structure [102, 104-106], and extraordinary stability. For example, TMV has been shown to be stable under various harsh conditions: temperatures up to 90 °C, extreme pHs (2-10) and organic solvents (80% ethanol, methanol, and DMSO) [103, 107, 108]. The coat proteins are rich in hydroxyl and carboxyl groups, making the hydrophilic virion negatively charged at pHs greater than 3.5, its isoelectric point (pI) [109]. Furthermore, the ability to confer surface functionalities via genetic manipulation [110] makes TMV an attractive choice compared to inorganic nanotubes. TMV has been exploited in creating a wide range of organic-inorganic hybrid materials [111, 112] and has also been applied in functional digital memory devices [113], battery electrodes [114, 115], and used for synthesis of metal nanoparticles [6, 116, 117]. Assembly of TMV [6, 7] in a hierarchical manner would provide means to fully harness its unique potential as a nanotemplate while also overcoming the aggregation challenges frequently confronted with functionalized nanoparticles [9]. Hydrogel microparticles offer highly porous 3D networks for immobilizing functionalized viral assemblies while still maintaining the function and structure of the hybrid nanostructures. In this dissertation, Chapter 2 describes a method for hierarchically assembling TMV onto hydrogel microparticles while Chapter 3 describes a method for

encapsulating TMV within microparticles to provide functional nanomaterials in a readily deployable 3D format.

1.3.3 Fluorescent Labeling Genetically Modified TMV

The genetically modified TMV nanotemplates, referred to as TMV1cys, used for the work presented in this dissertation possesses one cysteine residue on the outer surface of each coat protein, adding precisely spaced and high density thiol functionality. A molecular model (generated with UCSF Chimera software, see Section 2.2.5) of TMV1cys is shown in Figure 1.9. The red dots represent the cysteine residues genetically displayed on the outer surface of each coat protein (~2130 identical coat proteins per virion). An AFM topographical image of TMV1cys nanotemplates is shown in Chapter 2 of this dissertation (Figure 2.1b).

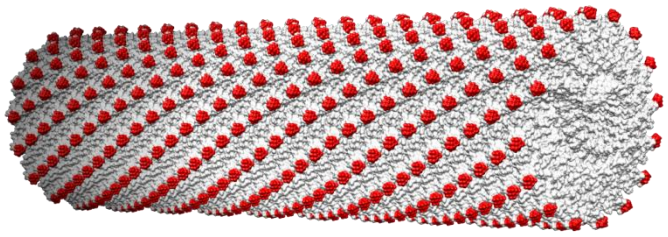

Figure 1.9. Molecular model of TMV1cys.
This model was generated with UCSF Chimera software (Section 2.2.5). The red dots represent cysteine residues genetically displayed on the outer surface of each coat protein, adding precisely spaced thiol functionality on the TMV nanotemplate.

In order to assess the assembly of TMV with microparticles via nucleic acid hybridization (Chapter 2) and to evaluate the distribution of TMV following

their encapsulation within microparticles (Chapter 3), TMV1cys was fluorescently labeled with fluorescein-5-maleimide. For the labeling reaction, the maleimide groups react specifically with sulfhydryl groups when the pH of the reaction mixture is between pH 6.5 and 7.5, to form stable thioether linkages that are not reversible [118]. The chemical structure of fluorescein-5-maleimide and the chemical reaction of maleimides toward thiols is shown in Figure 1.10.

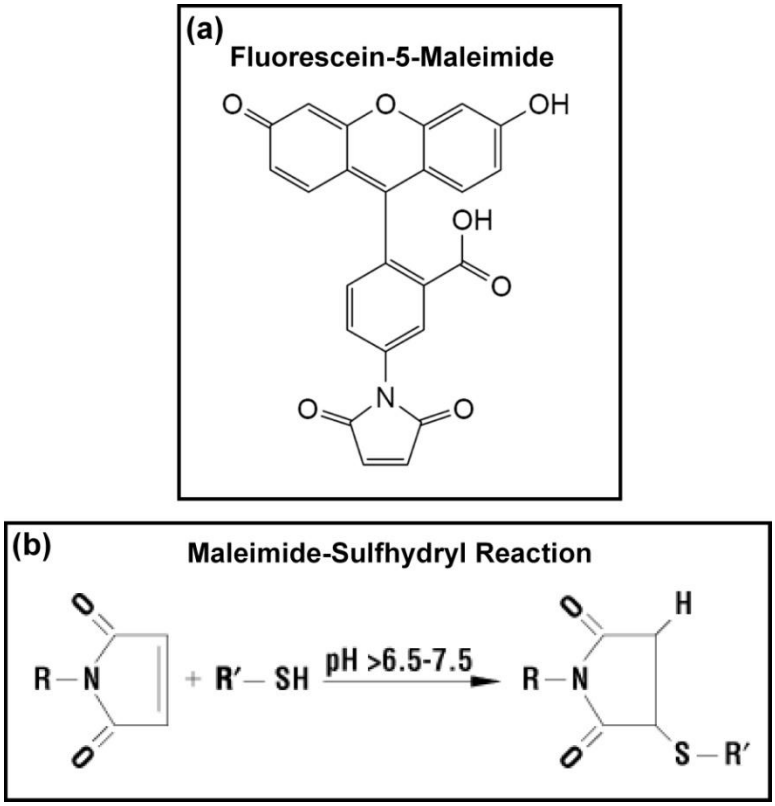

Figure 1.10. (a) Chemical structure of fluorescein-5-maleimide and (b) the maleimide-sulfhydryl reaction scheme.
The fluorescein-5-maleimide chemical structure image was reproduced from Thermo Scientific's product instructions [119]. The maleimide-sulfhydryl reaction scheme image was reproduced from Thermo Scientific's technical information provided on their website [118].

1.4 DNA OLIGONUCLEOTIDES

DNA oligonucleotides are synthesized strands of nucleotides containing a specific number of the well known nucleic acid bases thymine, adenine, cytosine, and guanine. Their size depends on the number of bases forming the DNA oligomer. Some are composed of 5 bases while others can extend up to 200 bases [57]. Since each nucleic acid base form a base pair with its complementary base, thymine with adenine and cytosine with guanine, DNA oligonucleotides can hybridize with complementary sequences to form DNA helices. Synthesis of DNA oligomers and their hybridization with complementary targets forms the basis for nucleic acid-based biosensors [120]. The remarkable recognition properties of DNA oligonucleotides and their structural features also make them extremely reliable for patterning materials with nanoscale precision [121]. Additionally, they have been used to precisely position a variety of functional molecules including proteins, nanoparticles, and small molecules into specifically designed patterns or nanoarchitectures [122-124]. Conjugation of DNA with metal, semiconductor, and polymer nanoparticles has been applied for use in nanodevices and catalysts [125] while future applications include nanoelectronics, nanoarrays for sensing, and alternative drug delivery techniques [123, 124, 126]. Specific areas of research, including supramolecular DNA assembly, DNA directed assembly, and DNA origami, have also evolved by using DNA oligonucleotides as the base technological component. Applications of these technologies include DNA patterning to control photonic processes [127], biosensors [128, 129], and the creation of 3D nanoarchitectures [130]. Thus,

DNA oligonucleotides provide significant potential in numerous applications by functioning as "glue" to merge functional molecules in a programmable and patterned assembly format. In this dissertation, DNA oligonucleotides are chemically conjugated into the matrix of hydrogel microparticles via continuous (Chapter 2) and batch fabrication (Chapter 4) to provide microparticles with the multitude of functional features just described as well as for nucleic acid-based hybridization assays.

1.5 DISSERTATION OUTLINE

Three fabrication strategies for poly(ethylene glycol) (PEG)–based microparticles assembled with TMV nanotemplates or DNA oligonucleotides in a continuous or batch format are presented in this dissertation, which is organized as follows:

Chapter 2 describes nucleic acid-based hybridization of TMV nanotemplates with encoded microparticles fabricated by a microfluidic technique known as stop-flow lithography (SFL). The significance of this work arises from the selective assembly of hybrid materials, which includes TMV nanotemplates and encoded microparticles.

Chapter 3 describes microfluidic fabrication of microparticles containing functionalized TMV nanotemplates. The work presented in this chapter addresses a critical challenge of 3D assembly of functionalized viral hybrid nanomaterials.

Chapter 4 describes a batch fabrication procedure, replica molding (RM), for DNA-conjugated microparticles. The work presented in this chapter illustrates a novel technique, which offers advantages over the traditional, continuous (microfluidic) fabrication methods for DNA-conjugated microparticles.

Chapter 5 summarizes the findings and describes future work that may be completed to further improve the functional microparticle fabrication methods presented.

2 NUCLEIC ACID HYBRIDIZATION-BASED ASSEMBLY OF VIRAL NANOTEMPLATES ON ENCODED MICROPARTICLES

2.1 INTRODUCTION

Structurally and chemically complex hybrid materials are needed for high end applications in renewable energy, electronics, computing, diagnostics, medicine and analytical chemistry [131-136]. To create materials with properties that transcend those of individual components, hierarchical assembly of units tailored across nanometer and micrometer length scales is highly desired [137]. Methods used to synthesize hierarchically assembled materials include direct or synergistic templating, self-assembly, photochemical patterning, electrodeposition, microcontact printing, and nanolithographic techniques [137-139]. These methods often involve a series of complex steps or have limited ability in controlling spatial resolution while maintaining full integrity of the individual components. Therefore, a facile method for hierarchically assembling hybrid materials in a programmable and selective manner under mild conditions is needed. Combining TMV nanotemplates with encoded microparticles containing discrete regions of different functionalities to create multifaceted hybrid materials may have significant potential in a broad range of applications including high throughput sensing.

In this chapter, hierarchical assembly of TMV nanotemplates onto encoded microparticles is demonstrated, as shown in Figure 2.1. The schematic diagram of Figure 2.1a depicts genetically modified TMV1cys nanotemplates, which possess one cysteine residue on the outer surface of each coat protein that serve as covalent coupling sites for fluorescein-5-maleimide, as described in Section 1.3.3. Following the fluorescent labeling reaction, the TMV nanotemplates were partially disassembled to expose the 5'end genomic RNA via sucrose gradient ultracentrifugation under alkaline pH. Since coat protein-RNA interactions are weakest at the 5'end of the viral RNA, mild alkaline treatments and centrifugation can be used to mimic cellular conditions in order to partially disassemble the virus and expose the 5'end of its genome [6]. Figure 2.1c shows that these labeled and partially diassembled TMV nanotemplates form a discrete band while unreacted fluorescein dye remains at the top of the sucrose gradient. Next, the TMV nanotemplates were programmed via hybridization with linker DNA consisting of two regions: one complementary to TMV's 5'end RNA and the other complimentary to the microparticle's probe DNA sequence. This conferred the probe DNA sequence-specific assembly address to the TMV (Table 2.1).

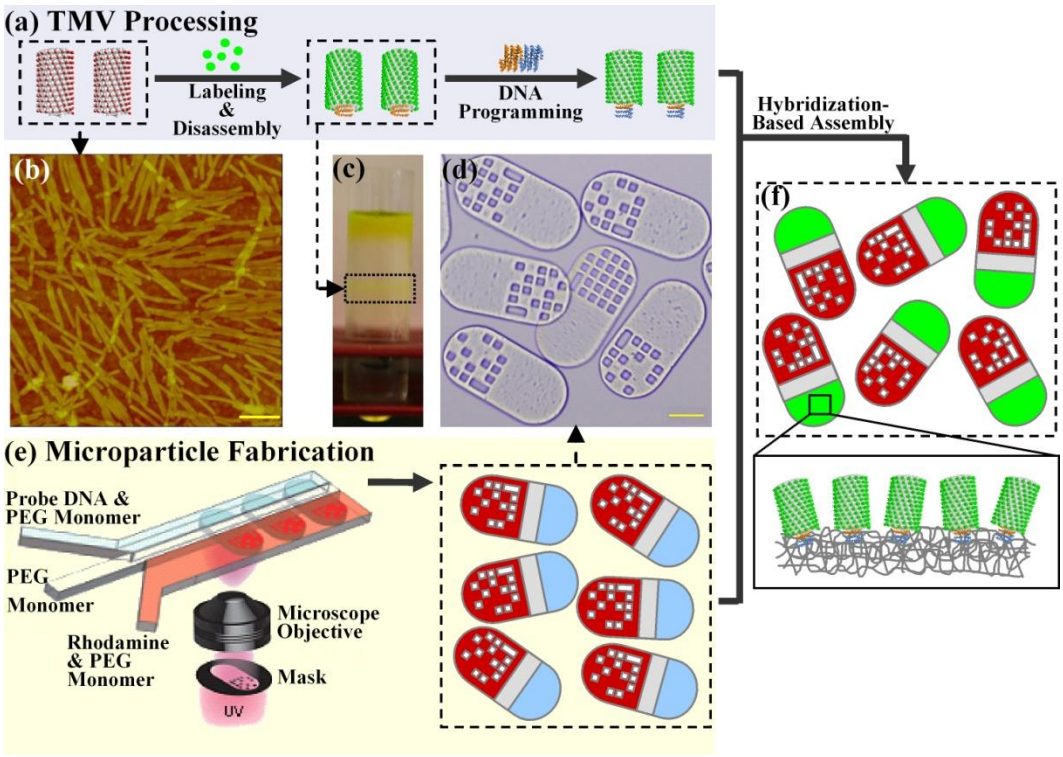

Figure 2.1. Procedure for hierarchical assembly of TMV nanotemplates onto PEG-based microparticles.
(a) Schematic diagram depicting the labeling, disassembly, and programming of TMV1cys. The TMV models were generated from UCSF Chimera software (Section 2.2.5) and represent approximately one tenth of the total TMV virion. The red dots represent cysteine residues genetically displayed on the outer surface of each TMV1cys coat protein (~2130 identical proteins per virion), adding precisely spaced thiol functionality for covalent conjugation of fluorescent markers. Partial disassembly followed by hybridization with linker DNA confers probe DNA-sequence specific assembly address. (b) Atomic Force Microscopy (AFM) topographical image of TMV nanotemplates. The yellow bar represents 300 nm. (c) Sucrose gradient containing fluorescently labeled TMVs as a discrete band (boxed) separated from unreacted fluorescein dye at the top of the sucrose gradient. (d) Brightfield micrograph of encoded microparticles. The yellow bar represents 50 μm. (e) Schematic diagram of stop-flow lithography (SFL) [12, 37] for production of encoded microparticles containing probe DNA. (f) Formation of nanobio-synthetic hybrid microentities following hybridization based assembly of TMVs with microparticles.

The PEG based microparticles consisting of the encoded, control, and probe DNA regions were fabricated in a microfluidic device via stop-flow lithography (SFL), as shown in the schematic diagram of Figure 2.1e. SFL [12] is a

photolithography based microfluidic technique that enables rapid and continuous production of various shaped microparticles using diacrylate chemistry and patterned UV crosslinking through a photomask containing the desired microparticle shape. The regions of different functionality are copolymerized seamlessly within each microparticle by a single exposure to UV. Benefits of the SFL technique include rapid and continuous production of monodisperse and biocompatible microparticles in a high throughput manner. This simple microfluidic technique affords the ability to create microparticles consisting of spatially discrete regions containing encoded identity information and covalently attached probe DNAs. The encoded region may be used to distinguish the microparticles from one another with over a million different codes available allowing immense multiplexing capability [37]. The region containing covalently attached probe DNAs provides a platform for selectively patterning TMV.

A brightfield micrograph of these microparticles is shown in Figure 2.1d. Hybridization based assembly of the labeled and programmed TMVs with the encoded microparticles containing probe DNA creates nanobio-synthetic hybrid microentities, as shown in Figure 2.1f. Fluorescence microscopy, AFM, and confocal microscopy results clearly illustrate facile assembly of TMV nanotemplates onto microparticles with high spatial and sequence selectivity. Since proteins and antibodies can be covalently linked to TMV via its high density thiol surface functionality, we envision that this facile assembly strategy can be readily exploited for a variety of biotechnological applications such as high throughput, multiplexed protein sensing [88, 140].

The work presented in this chapter was completed in collaboration with Wui Siew Tan, who fabricated all of the microparticles used to obtain the results. Nick Horelik acquired the AFM images. Dan Pregibon provided helpful guidance with this work. My contribution to this work involved fluorescently labeling and programming the TMV nanotemplates and hybridizing them with the microparticles. I also completed all of the imaging work except for that completed with AFM. The chapter content was reproduced from Tan, Lewis, Horelik, Pregibon, Doyle, Yi, *Langmuir*, 2008 [141].

2.2 MATERIALS AND METHODS

2.2.1 TMV1cys and Fluorescent Labeling

TMV1cys was provided as a generous gift from James Culver, University of Maryland Biotechnology Institute, Center for Biosystems Research. Purified TMV1cys was incubated at room temperature for 2 h with 10-fold molar excess of fluorescein-5-maleimide (Biotium, Hayward, CA) in 100 mM Tris-buffer, pH 7.0. Fluorescein-labeled virus was separated by centrifugation in a 10-40% sucrose gradient [6, 7] at 48,000 g for 2 h while the pH was adjusted to 8.0 to partially remove coat protein subunits from the 5'ends of the viral genome. Partially disassembled virions were pelleted by centrifugation for 40 min at 106,000 g. Pelleted viruses were resuspended in 5 × saline sodium citrate (SSC) buffer (75 mM sodium citrate, 750 mM sodium chloride, pH 7.0).

2.2.2 Microparticle Fabrication

PEG microparticles were synthesized as previously described [37]. Briefly, poly(ethylene glycol) diacrylate (PEG-DA Mn=700, Aldrich) was mixed with 2.5% (v/v) of 2-Hydroxy-2-methylpropiophenone photoinitiator (Darocur 1173, Aldrich), 33% (v/v) of TE buffer (10 mM Tris pH 8.0 (Rockland Immunochemicals, Inc., Gilbertsville, PA), and 1 mM EDTA (OmniPur)) containing 0.01% (v/v) of 10% (w/w) sodium dodecyl sulfate (SDS, Invitrogen). This base prepolymer mixture was mixed in a 9:1 volume ratio with 1 part of TE solution containing Acrydite^{TM} modified probe DNAs, blue food dye (to visualize the co-flowing prepolymer streams using bright-field microscopy), or Rhodamine B (Polysciences Inc., Warrington, PA). DNA probes (IDT Technologies, Coralville, IA) were modified with a reactive Acrydite^{TM} group and an 18-carbon spacer. Three different sequences were used in this study, as shown in Table 2.1. Final prepolymer mixtures contained either (a) 50 µM DNA-Acrydite^{TM} modified probe DNA (C1, C2 or C3) (b) 1% (v/v) blue food dye or (c) 0.1 mg/ml of Rhodamine B. The prepolymer mixtures were co-flowed through microfluidic PDMS devices made by traditional soft lithographic methods. Channels were designed with one to three 100 µm wide channels, which converged into a single 200 to 400 µm wide channel allowing co-flow of up to three different prepolymer streams to create microparticles with up to three distinct regions. The thickness of each stream was controlled by adjusting the relative pressure on each of the inlet channels, which were connected to a pressure source (regulated by a pressure valve, Controlair Inc., Amherst, NH). Using an inverted Zeiss Axiovert 200

microscope with a 100 W HBO mercury lamp and photomasks inserted in the field-stop position, PEG microparticles were polymerized by 75 ms bursts of wide-excitation ultraviolet (UV) light from a 11000v2 UV filter set (Chroma Technology Corp., Rockingham, VT). A computerized stop-polymerize-flow sequence of ~1 s was cycled to obtain thousands of microparticles in less than 20 min. The resulting microparticles were 30 μm thick and of shapes projected from the photomask. Using a 20 × optical objective, photomasks were designed to form the 180 × 90 μm encoded microparticles shown in Figure 2.1d. These microparticles (3 types) were made using three co-flowed streams, shown in Figure 2.1e with probe DNA C1, C2, or C3, each containing a different encoded region. Microparticles were cleaned of unreacted prepolymer with three different rinse solutions: TE buffer containing 0.1% (v/v) Tween 20 surfactant, PEG-DA prepolymer, and TE buffer containing 1% (v/v) Tween 20 surfactant. The rinses were completed with ~1 mL of rinse solution, vortexing, centrifugation, and aspiration of supernatant. Microparticles were stored in TE buffer containing 1% Tween 20 surfactant at 4 °C before use in hybridizations.

Table 2.1. Single Stranded DNA Sequences

Name	5'end	Sequence	3'end
Probe DNA Conjugated within the Microparticles			
C1	Acrydite-C18	ATGATGATGATGATGATG	---
C2	Acrydite-C18	TTTTTCGGCAGGTCGGTAAC	---
C3	Acrydite-C18	CACTACCGATACGTACTCAG	---
Fluorescently Labeled Single Stranded DNA Hybridized with Microparticles			
C3'	FITC*	CTGAGTACGTATCGGTAGTG	---
Linker DNA Hybridized with TMV and Microparticles			
C2'	---	GTTTGTTGTTGTTGGTAATTGTTG*TTTTT*GTTACC GACCTGCCGAAAAA†	---

*FITC: fluorescein isothiocyanate.
†The detailed sequence description entails: TMV 5'end Complementary Sequence Spacer Address-specific Sequence.

2.2.3 Hybridization Based Assembly of TMV Nanotemplates

For address specific programming of labeled and partially disassembled TMV, 10-fold molar excess of linker DNA (IDT Technologies, Coralville, IA) was added to fluorescein-labeled TMV solutions and incubated at 30 °C for 2 h. The linker DNA consisted of two regions: one complementary to TMV's 5' end RNA and the other complimentary to the microparticle's probe DNA sequence, as shown in Table 2.1. To remove the unbound linker DNA, mixtures were centrifuged at 106,000 g for 40 min in 5 × SSC buffer. The fluorescein-labeled single stranded (ss) DNA, described in Table 2.1, was purchased from Gene Probe Technologies Inc. (Gaithersburg, MD). For assembly of TMV, both the programmed TMV nanotemplates and fluorescein-labeled ssDNA were resuspended in 5 × SSC buffer containing 0.01% (v/v) Tween 20 and hybridized with the microparticles overnight at 37 °C. The final TMV and ssDNA concentrations in the hybridization solution were ~50 to 100 nM. The

microparticles were then rinsed several times with 2 × SSC buffer containing 0.01% (v/v) Tween 20.

2.2.4 Imaging Analysis

Brightfield and fluorescence micrographs were captured with an Olympus (Center Valley, PA) BX51 upright microscope equipped with an Olympus DP70 microscope digital camera and a standard green filter set, 31001 from Chroma Technology Corp. (Bellows Falls, VT). The fluorescence images were evaluated with the fluorescence intensity profile function from ImageJ software [142]. AFM images were obtained using a Dimension 3100 AFM (Digital Instruments, Santa Barbara, CA) with a Nanoscope IV Controller operated in dry tapping mode with a scan rate of 0.5 Hz and moderate amplitude setpoints. Tap300 silicon probes (Budget Sensors, Sofia, Bulgaria) were used at approximately 300 Hz. The AFM images were analyzed using Nanoscope software version 6.00. Confocal images were acquired on a Leica DMIRE2 microscope with a TCS SP2 scanner (Wetzlar, Germany) equipped with a 63 × (NA 1.2) water immersion objective and analyzed at 488 nm excitation and 500 to 530 nm emission. Samples were placed on number 1.5 cover glass within a PDMS well. The depth scan increment was 1 μm with a scan thickness of ~155 nm. Analysis was performed with the Leica Confocal Software (Wetzlar, Germany).

2.2.5 Molecular Modeling

The TMV molecular graphics images were produced using the UCSF Chimera package (http://www.cgl.ucsf.edu/chimera) [143-145] from the Resource

for Biocomputing, Visualization, and Informatics at the University of California, San Francisco (supported by NIH P41 RR-01081). The base structure of TMV (PDB ID: 2tmv) [146] used in the molecular graphics images was obtained from the Research Collaboratory for Structural Bioinformatics Protein Data Bank (RCSB PDB, http://www.pdb.org/) [147].

2.3 RESULTS AND DISCUSSION

2.3.1 Assembly of TMV Nanotemplates onto Encoded Microparticles

We first demonstrate hierarchical assembly of fluorescein-labeled TMV nanotemplates onto microparticles via nucleic acid hybridization. The microparticles were fabricated in a microfluidic device via stop-flow lithography (SFL) [12], as shown in Figure 2.1e, and consisted of three discrete regions: an encoded region containing Rhodamine B, a middle negative control region, and a probe DNA region. TMV nanotemplates were labeled with fluorescein maleimide, which forms a covalent thioether bond with the genetically displayed cysteine's thiol groups. These labeled TMVs were partially disassembled to expose the 5'end genomic RNA then programmed with linker DNAs via hybridization to confer the probe DNA sequence-specific address. These labeled and programmed TMVs were incubated with microparticles for hybridization based assembly and examined with a fluorescence microscope, as shown in Figure 2.2.

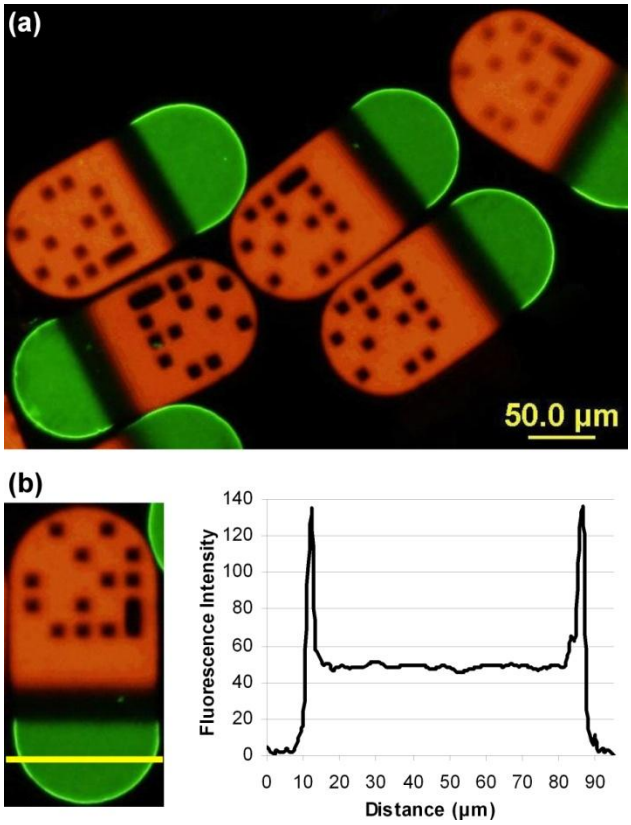

Figure 2.2. Hierarchical assembly of fluorescein-labeled TMV nanotemplates onto microparticles via nucleic acid hybridization.
(a) Overlay fluorescence image of fluorescein-labeled TMV1 nanotemplates onto Rhodamine B labeled and encoded microparticles. Three regions define the 180 × 90 × 30 µm microparticles: an encoded region containing Rhodamine B, a middle negative control region, and a probe DNA region. (b) Fluorescence intensity plot across the TMV assembled region shown by the yellow line.

As shown in the fluorescence micrograph of Figure 2.2a, fluorescein-labeled TMVs readily assembled onto the probe DNA region of the microparticles. Importantly, the encoded and middle control regions of the microparticles showed minimal non-specific binding (from TMV-conjugated fluorescein), demonstrating high spatial selectivity. Figure 2.2a also shows the reproducibility of both the particle fabrication process and TMV assembly. The fluorescence intensity profile plot in Figure 2.2b shows a uniform TMV assembly

density on the microparticles, as the fluorescence intensity is nearly constant across the TMV region of the microparticles, excluding the edges. Since the TMVs are unable to penetrate far into the microparticles, their localization near the surface of the probe DNA region is expected and results in the bright edges seen when microparticles are lying flat and viewed top-down as shown in Figure 2.2a. Combined, these results demonstrate the highly uniform and multifunctional nature of the microparticles, and the creation of viral-synthetic microentities via hybridization-based assembly of TMV nanotemplates with encoded microparticles.

2.3.2 Sequence Specific Assembly of TMV with Microparticles

To directly demonstrate the sequence specificity of the assembly procedure, fluorescein-labeled and linker DNA (C2') programmed TMV nanotemplates were incubated with a mixture of microparticles, as shown in Figure 2.3. This microparticle mixture contained three types, as shown in Figure 2.3a, each with different codes and probe DNA sequences (C1, C2,and C3). The fluorescence micrograph of Figure 2.3b clearly shows that TMVs assembled only onto the microparticles containing the matching probe DNA sequence (C2). Importantly, minimal fluorescence in the probe DNA area of the non-specific microparticles demonstrates the highly selective nature of the hybridization-based assembly. This result confirms that the assembly event occurs via sequence specific hybridization, suggesting the feasibility of simultaneous "one-pot" assembly of multiple TMV conjugates with a large number of microparticle types, each containing a different barcode and probe DNA sequence. Additionally, the

encoded region enables identification of the DNA sequence derived functionality, suggesting the potential for a high throughput screening capability. Similarly, site-specific assembly of TMV conjugates carrying multiple functionalities to multiple regions on a single particle can also be envisioned. The latter could readily be achieved using the versatility of the SFL process that allows production of microparticles with more than one DNA probe region containing different probe DNA sequences.

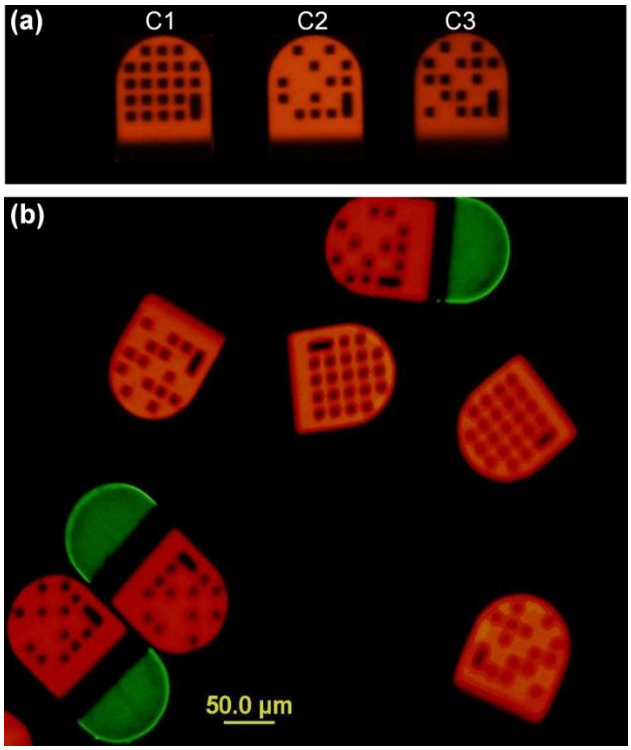

Figure 2.3. TMV nanotemplates hybridized with a mixture of three different microparticle types.
(a) Three microparticle types, all differing by the barcode and probe DNA sequence embedded within the microparticles. (b) Fluorescence overlay image showing fluorescein-labeled TMV assembled onto only the microparticles containing the matching DNA sequence, C2.

2.3.3 Atomic Force Microscopy (AFM) of TMV on Microparticles

AFM has been extensively employed in studying biological materials, especially TMVs on solid substrates. These efforts have led to the elucidation of various fundamental properties including mechanical strengths [148], conductivity [149], and flexoelectricity [150] to list a few. Here, AFM was used to physically confirm the presence of TMV nanotemplates on the microparticles and examine the structural integrity of assembled TMVs. For this, the TMV-assembled microparticles were extensively rinsed, dried under ambient conditions for 5 days, and examined with tapping mode using a standard silicon tip. The phase contrast AFM image of Figure 2.4 clearly shows that TMV nanotemplates are assembled on the microparticles with high density and have maintained their full structural integrity. Further, the encoded and negative control regions were also examined via AFM, and did not show a significant number of TMVs (images not shown). Additionally, despite the extensive rinsing and drying conditions necessary for AFM sample preparation, the microparticle-assembled TMVs retained their structure, demonstrating the stability of these hybridized TMV nanotemplates. Overall, this result clearly confirms the presence and structural integrity of TMV nanotemplates assembled on microparticles.

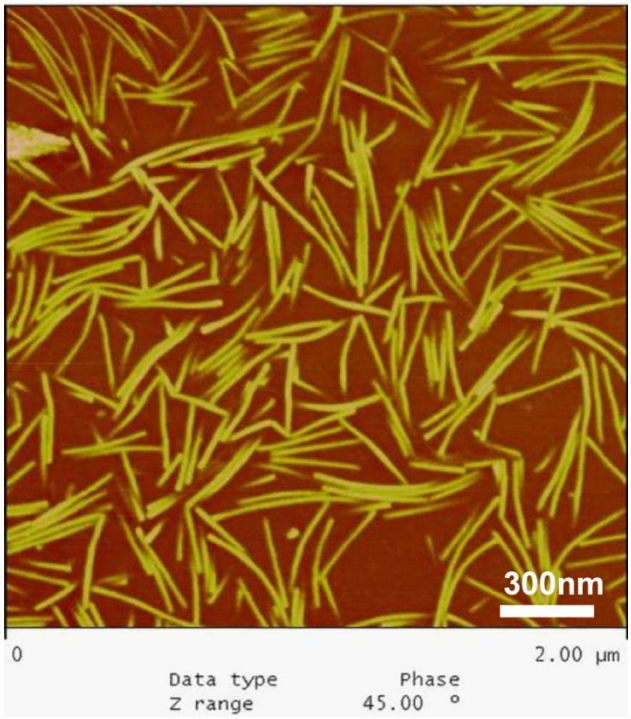

Figure 2.4. AFM phase contrast image of TMV assembled onto encoded microparticles.

2.3.4 Confocal Microscopy of TMV Assembled Microparticles

As shown in Figure 2.5, we employed confocal microscopy to examine detailed 3-D assembly features of the TMV-and fluorescein labeled ssDNA-assembled microparticles. As shown in the schematic diagram of Figure 2.5a and the brightfield micrograph of Figure 2.5b, the microparticles used for this evaluation contained two spatially discrete probe DNA regions coding different sequences and separated by a negative control region. These microparticles were incubated in a solution containing two fluorescein labeled species: fluorescein labeled TMV programmed with linker DNA complementary to the round region (C2) and fluorescein labeled ssDNA complementary to the rectangular region (C3).

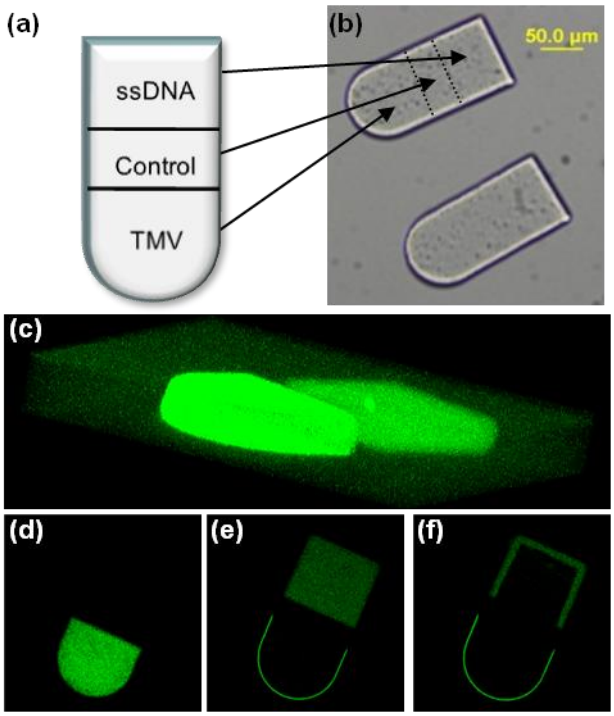

Figure 2.5. One-pot assembly of fluorescein-labeled TMV and ssDNA onto discrete regions of multifunctional particles.
(a) Schematic diagram showing the three regions of the multifunctional microparticles: the TMV-complimentary (round edge) and ssDNA-complimentary (straight edge) regions are separated by a middle negative control region. (b) Brightfield image of the multifunctional microparticles. The yellow bar represents 50 µm. (c) Reconstituted 3-D confocal image of a multifunctional microparticle following hybridization with the fluorescein-labeled TMV and ssDNA. (d-f) Confocal z-scan images of TMV and ssDNA hybridized microparticles at the surface (d) several micrometers below the surface (e), and center (f).

A z-scan analysis on these microparticles clearly shows the difference in the 3-D assembly feature between the two regions, as shown in Figures 2.5c to f. First, the three-dimensional reconstituted image of Figure 2.5c shows the difference in spatially selective assembly and in material characteristics between the TMV-assembled and DNA-assembled regions. The TMV-assembled region shows bright fluorescence at the very outer surface of the microparticles, and

minimal fluorescence within the microparticle matrix. This result occurs because the large size of the TMV (~300 nm) prevents deep penetration into the hydrogel matrix of the particle. In contrast, the DNA assembled region shows more dispersed fluorescence near the particle surface. This results occurs because the smaller size of the fluorescein labeled DNA (~10 to 14 nm) allows it to diffuse deeper into the hydrogel, and correlates well with previously reported results for a similar system [37]. This difference in the penetration depth is further demonstrated in the z-scan images of Figures 2.5 at the surface (d), several micrometers below the surface (e), and at the center (f). Figure 2.5d, taken at the top surface of the microparticle shows that TMVs are assembled only onto the circular region with high fluorescence intensity, while the rectangular ssDNA region shows minimal fluorescence. As the z-scan layer moves a few micrometers toward the microparticle center, Figure 2.5e shows that the TMV layer is confined to the outer surface whereas the fluorescein labeled DNA layer just starts to appear. Finally, Figure 2.5f, taken at the microparticle center, shows that the TMVs are mainly assembled within the outer ~2 μm region of the microparticles with high fluorescence while DNA penetrates several micrometers deeper. Importantly, these confocal microscopy results illustrate the high fluorescein-templating density of the TMV nanotemplates given the same fabrication condition and thus probe DNA density in the two regions. The difference in fluorescence intensities of the TMV bound region versus the ssDNA bound region reflects the high fluorescein-templating density of the TMV nanotemplates. Since numerous fluorescein molecules are conjugated to each

TMV while only one fluorescein molecule is attached to each ssDNA, the amount of fluorescence per DNA binding event is multifold for TMV compared to ssDNA. Furthermore, the two probe DNA regions do not show any overlapping assembly characteristics, strongly suggesting the sequence specificity of the sequence design and assembly procedures. Together, these results illustrate the potential for integrating TMVs and SFL in creating multifaceted hybrid materials.

2.4 CONCLUSIONS

The fluorescence microscopy results reported in this study illustrated both the spatially selective and sequence specific nature of the assembly process. High spatial selectivity is afforded by the fidelity of the sequence specific DNA hybridization used in the assembly process and holds potential for one-pot assembly of multiple TMV conjugates to different encoded microparticles or to different regions on a single microparticle. In addition, the assembly and particle fabrication processes were shown to be very reproducible. The AFM images clearly showed that the TMV nanotemplates are assembled on the microparticles with high density and full structural integrity despite the extensive rinsing and drying required to prepare samples for AFM analysis. The confocal microscopy results demonstrated the feasibility of one-pot assembly between multiple TMV conjugates and a large number of microparticle types, each containing a different barcode and probe DNA sequence. The confocal microscopy images also showed the high fluorescein-templating density of the TMV nanotemplates and that these nanotemplates are assembled on the microparticle surface. Combined, these

results represent a novel high throughput route to create multiplexed and multifunctional viral-synthetic hybrid microentities in mild aqueous conditions. We expect that the integration of viral nanotemplates and the rapid SFL technique will have significant potential in creating complex structures for a broad range of applications. For example, one could envision protein sensing with antibody conjugated TMVs assembled onto encoded microparticles. The multiplexing capability of such protein-viral-synthetic hybrid materials would enable high throughput analysis of analytes [37].

3 MICROFLUIDIC FABRICATION OF MICROPARTICLES CONTAINING FUNCTIONALIZED VIRAL NANOTEMPLATES

3.1 INTRODUCTION

Despite recent advances in catalytic applications [10, 91, 151] and 2D assembly strategies [7, 152-154], facile routes to assemble functionalized viral nanotemplates in a readily usable and stable 3D format while harnessing their unique features have not been demonstrated. As mentioned in Chapter 1, this challenge arises in part from aggregation and stability issues with metal [8] and viral [9] nanoparticles. Yet, uniform distribution of functionalized viral nanotemplates in a stable and readily accessible 3D format providing facile handling of these hybrid nanoentities is highly desired to exploit their advantages.

Hydrogel microparticles offer highly porous 3D networks for immobilizing functionalized viral assemblies while still maintaining the function and structure of the hybrid nanostructures. Moreover, the hydrophilic nature of hydrogels should allow for a wide range of applications in aqueous environments. Additionally, microfluidics offers a rapid and efficient route to fabricate monodisperse hydrogel particles [2], with strong potential for precise tuning of microparticle size and morphology [155]. This potential to control the structure and size of particles is important for engineering specific features, such as

anisotropy, large surface areas, or light-scattering properties [43, 156]. Thus, microfluidic fabrication of hydrogel microparticles provides a reproducible and consistent procedure for uniformly distributing functionalized viral assemblies in a readily usable 3D format that should address critical challenges in 3D assembly of functionalized viral hybrid nanomaterials.

A microfluidic fabrication procedure to rapidly produce functionalized viral-synthetic hybrid microparticles is presented in this chapter. As shown in Figure 3.1, genetically modified TMV templates (TMV1cys) were either labeled with fluorescent markers via covalent conjugation on genetically displayed cysteine groups (Section 1.3.3) [6, 7, 141], or decorated with palladium (Pd) nanoparticles [151, 157], as shown in Figure 3.1a. A microfluidic flow-focusing device was used to encapsulate functionalized TMV nanotemplates within microparticles, as shown in Figure 3.1b. TMV-poly(ethylene glycol) diacrylate (PEG-DA) solution is the dispersed phase in this two-phase flow process, which rapidly forms approximately 500 droplets per minute within a continuous phase of mineral oil. Photopolymerization of the droplets with UV light forms PEG-based hydrogel microparticles. Fluorescently labeled TMV provided a means to evaluate the distribution of the TMV nanotemplates within the microparticles via fluorescence or confocal microscopy. Catalytic activity from the particles containing Pd-TMV complexes is demonstrated via the dichromate reduction reaction, a simple yet important model reaction for facile environmental cleanup of toxic chemicals [151]. Finally, Janus microparticles with two sides differing in chemistry and functionality were fabricated. These particles contain magnetic

nanoparticles embedded in one side, which enable simple separation of the microparticles from bulk solution. Combined, these results demonstrate rapid microfluidic fabrication of functional viral-hydrogel composite microparticles enabling exploitation of nanofunctional materials, such as metal nanoparticles, in a readily deployable 3D format.

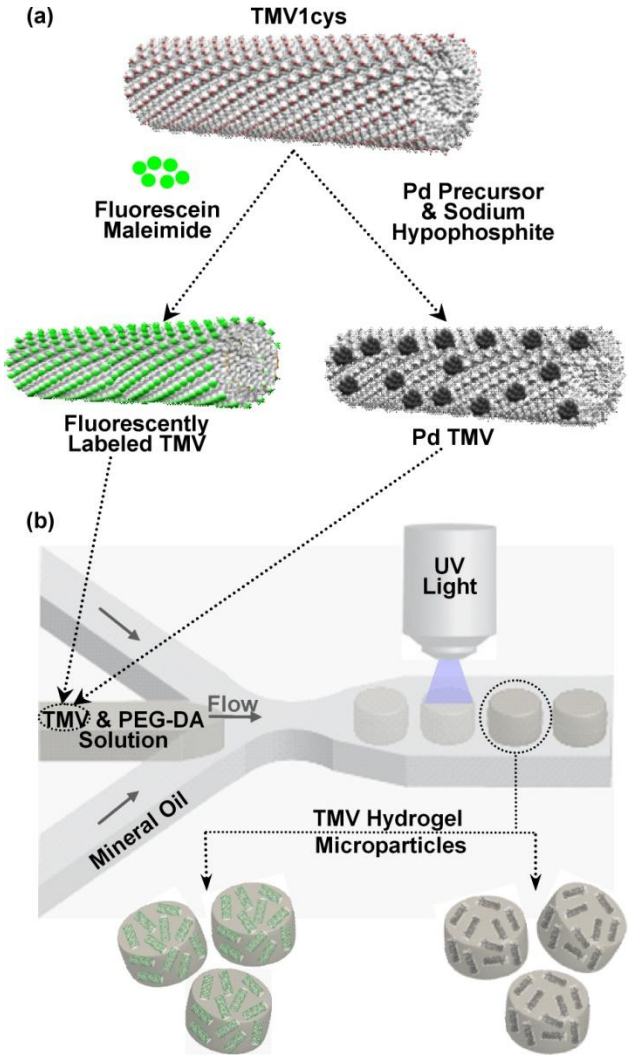

Figure 3.1. Fabrication procedure for microparticles containing fluorescently labeled TMV or palladium (Pd) -TMV complexes.
(a) Chimera model images (Section 3.2.1) representing approximately one fifth of an entire TMV1cys virion. The red dots represent cysteine residues genetically displayed on the outer surface of each coat protein (~2130 identical proteins per virion). TMV1cys is readily labeled with fluorescein maleimide at the cysteines or metalized with Pd nanoparticles via electroless plating. (b) Schematic diagram of the microparticle fabrication procedure with a microfluidic flow-focusing device (40 × 50 μm, height × width, at the region following droplet formation). The dispersed droplet phase is a TMV-PEG solution and the continuous phase is mineral oil. Droplets are photopolymerized with UV light providing PEG-based hydrogel microparticles (~50 μm diameter) containing fluorescently labeled TMV or Pd-TMV complexes.

The results presented in this chapter were obtained, in part, from collaboration with Dr. Yan Lin, Cuixian Yang, and Kai Yuet. Dr. Lin fabricated the microparticles containing Pd-TMV complexes with assistance from Amy Manocchi. Cuixian Yang completed the catalytic activity studies. Kai Yuet provided much assistance with building the droplet-based particle fabrication system used to produce the results. I was responsible for transferring the droplet-based particle fabrication procedure from the Doyle lab at MIT to the Yi lab at Tufts University. As such, I set up the microfluidic system on an upright microscope while implementing appropriate modifications since the original system was set up on an inverted microscope. This included determining the appropriate thickness of the PDMS microfluidic channels and tuning the UV light intensity to ensure appropriate polymerization of the droplets to form microparticles. I then determined the suitable conditions for distribution of fluorescently labeled TMV nanotemplates with the prepolymer solution. I also found the appropriate ratio between the continuous and dispersed phase flow rates to form the TMV-prepolymer droplets within the microfluidic device, which could be photopolymerized to form microparticles containing TMV. Much of this chapter was reproduced from Lewis, Lin, Yang, Manocchi, Yuet, Doyle, Yi, *Langmuir*, 2010 [158].

3.2 MATERIALS AND METHODS

3.2.1 TMV1cys

The creation of TMV1cys is described previously [6]. To generate concentrated TMV1cys for this work, healthy tobacco plants were infected with TMV1cys and then purified as described by Gooding et al. [159]. The TMV molecular graphic images were produced using the UCSF Chimera package as described in Section 2.2.5. TMV1cys was fluorescently labeled as described in Sections 1.3.3 and 2.2.1 and the fluorescein-labeled and pelleted viruses were resuspended in TE buffer (10 mM Tris, pH 8.0, Sigma-Aldrich and 1 mM EDTA, Sigma-Aldrich).

3.2.2 Microparticle Fabrication

Microfluidic channels were initially designed using AutoCAD 2009 (Autodesk, Inc., San Rafael, CA) and then translated into silicon master molds by the Stanford Microfluidic Foundry (http://www.stanford.edu/group/foundry/). The microchannel dimensions in the region following droplet formation was 40 × 50 μm (height × width). Poly(dimethylsiloxane) (PDMS)-based microfluidic devices were prepared by soft lithography [160] with the silicon master molds. Briefly, Sylgard 184 Silicone Elastomer by Dow Corning (Midland, MI) was poured into the silicon master mold, degassed, and cured according to the manufacturer instructions. The final thickness of the PDMS slab containing the microchannels was approximately 5 mm. The channels were then sealed onto

PDMS coated glass slides which were partially cured for 30 min at 65 ºC, and then cured for an additional 2 h at 65 ºC.

The continuous phase of this two-phase microfluidic procedure was mineral oil from Sigma (St. Louis, MO) containing 3% (v/v) emulsifier, ABIL EM 90, from Evonik Industries (Parsippany, NJ). The fluorescently labeled TMV and PEG-DA solution consisted of 55% (v/v) fluorescently labeled TMV in TE buffer, 40% poly(ethylene glycol) diacrylate (PEG-DA), M_n=700, Sigma, and 5% 2-hydroxy-2-methylpropiophenone, photoinitiator (PI), Sigma. The final concentration of fluorescently labeled TMV was 0.6 mg/mL. The PEG-DA solution not containing TMV and used to form the Janus particles in Figure 3.3b consisted of 54% TE buffer, 39% PEG-DA, 2% blue food dye, and 5% PI. The Pd-TMV-PEG-DA solution used to form the particles, as shown in Figure 3.4c, consisted of 25% PEG-DA, 15% PEG (M_w=200), Sigma, 5% PI, and 55% Pd-TMV complex solution (3 mM sodium tetrachloropalladate (II) (Na_2PdCl4, 99.998%, Pd precursor, Sigma), 15 mM sodium hypophosphite ($NaPH_2O_2$, precursor reducer, Sigma), and 0.3 mg/mL TMV in 0.01 M phosphate buffer). The Pd-TMV-PEG-DA solution used to produce the side of the Janus particles containing Pd-TMV, as shown in Figure 3.4f, consisted of 40% PEG-DA, 5% PI, and 55% Pd-TMV complex solution, as described above. The magnetic nanoparticle-PEG-DA solution used to produce the magnetic side of the Janus particles, as shown in Figure 3.4f, consisted of 40% PEG-DA, 5% PI, 25% DI water, 10% DI water containing 0.5% Tween 20, and 20% magnetic nanoparticle solution EMG-508 from Ferrotec Corporation (Bedford, NH).

The mineral oil and the preparticle solutions were separately introduced to the microchannels through 18-gauge Intramedic Luer-Stub adapters by Becton Dickinson, and Company (Franklin Lakes, NJ) and Tygon tubing by Saint-Gobain Performance Plastics (Paris, France) connected to a common pressure source. Pressures ranging between 0 and 69 kPa were used to control the fluid flow rate through the microchannels. Type 700-BD manual pressure regulators by Control Air (Amherst, NH) and DPG1000B-30G digital pressure gauges by Omega (Stamford, CT) were used to control and monitor the pressure directed to the microchannels. The UV light source was provided by a 100 W mercury lamp and an 11000v3 UV filter set by Chroma Technology Corp. (Bellows Falls, VT). For microparticle photopolymerization within the PDMS microchannels, UV light was focused onto a specific location within the channel through an Olympus (Center Valley, PA) long working distance 20 × objective with a NA of 0.4 on an Olympus BX51 upright microscope.

Following photopolymerization, the microparticles were collected in reservoirs located at the end of the microchannels. The particles were transferred from this reservoir into an Eppendorf tube with a pipette. The particles were briefly centrifuged to separate them from the mineral oil and remaining PEG prepolymer solution. The particles were then removed from the bottom of the Eppendorf tube with a pipette, transferred to a new tube, and washed several times with DI water containing 0.5% (v/v) Tween 20 (Sigma, St. Louis, MO). The washing procedure consisted of pipetting the DI water solution into the tube

containing the particles, vortexing, and centrifugation before removing the DI water supernatant.

3.2.3 Imaging Analysis

Brightfield and fluorescence micrographs and confocal images were captured as described in Section 2.2.4. For the confocal images, a series of z-scan images with a depth scan increment of 3 µm were collected from the ~40 µm thick cross-section of the disc shaped microparticles containing fluorescently labeled TMV. Compilation of this image series provided a reconsitutued 3-D image, as shown in Figure 3.2e. The z-scan image captured at the particle center is shown in Figure 3.2f. Transmission Electron Microscope (TEM) images were collected using a JEOL 2100 TEM operated at 200 kV. TEM samples were prepared by placing the Pd-TMV complex solution on a TEM grid and allowing the solution to settle for two minutes. The grid was then placed on filter paper to wick away the liquid.

3.2.4 Catalytic Activity for Dichromate Reduction

The reaction conditions and the procedure for determining the conversion and apparent first-order rate constant for dichromate reduction were followed as described previously [151]. Briefly, the 0.3 mL reaction solutions consisted of 0.1 mM potassium dichromate ($K_2Cr_2O_7$, 99.5%, Sigma, St. Louis, MO), which was the source of Cr (VI), and 100 mM sodium formate (HCOONa, 99%, Fisher), which was the electron donor for the dichromate reduction. The ionic equations for the redox reaction are shown in Equations 8 and 9 [161].

Equation 8

$$Cr_2O_7^{2-} + 14H_3O^+ + 6e^- \leftrightarrow 2Cr^{3+} + 21H_2O$$

Equation 9

$$HCOO^- + H_2O \leftrightarrow CO_2 + H_3O^+ + 2e^-$$

The dichromate reduction reactions were carried out in Eppendorf tubes with continuous stirring. At specific time points, samples of the reaction supernatant were evaluated at 350 nm, characteristic of the adsorption of Cr(VI) ions, with an Evolution 300 UV-visible Spectrophotometer (Thermo Scientific, Waltham, MA) to determine the concentrations of Cr(VI). The extent of the catalytic reduction, expressed as percent conversion, was determined with Equation 10, where $[Cr(VI)]_o$ represents the initial concentration and [Cr(VI)] represents the concentration at a specific time point.

Equation 10

$$\text{Conversion}(\%) = \frac{[Cr(VI)]_o - [Cr(VI)]}{[Cr(VI)]_o} \times 100$$

Based on the large concentration difference between sodium formate and potassium dichromate, the sodium formate concentration was assumed constant throughout the reaction period. Thus, the reaction of Equations 8 and 9 followed pseudo first-order kinetics. A first-order rate constant, as shown in Equation 11,

was estimated via the linear regression of ln([Cr(VI)]/[Cr(VI)]$_o$) vs. reaction time, as shown in Equation 12.

Equation 11

$$r = -\frac{d[Cr(VI)]}{dt} = k_1[Cr(VI)]$$

Equation 12

$$\ln\frac{[Cr(VI)]}{[Cr(VI)]_o} = -k_1 t$$

3.3 RESULTS AND DISCUSSION

3.3.1 Microfluidic Fabrication of TMV-PEG Microparticles

We first demonstrate rapid microfluidic fabrication of viral-synthetic hybrid microparticles, as shown in Figure 3.2. For this, TMV1cys was fluorescently labeled at the genetically displayed cysteine residues via covalent conjugation with thiol-reactive fluorescein maleimide (Figure 3.1a). The labeled TMVs were then purified using sucrose gradient centrifugation [141], and mixed with PEG-DA solution. TMV-PEG particles were formed by a continuous microfluidic procedure with a poly (dimethyl-siloxane) (PDMS)-based flow-focusing device (FFD) and UV photopolymerization, as shown in Figure 3.1b. The brightfield and fluorescence micrographs of Figures 3.2a and b show the formation of highly uniform microparticles as well as uniform distribution of

TMV within the particles (approximately 50 pg TMV per particle). Importantly, the images of particles without fluorescently labeled TMV in Figures 3.2c and d do not show fluorescence, confirming that the fluorescence in Figure 3.2b is from fluorescently labeled TMV. While the conditions employed in this study consistently produced ~50 μm diameter particles, there are various means to control droplet sizes in FFDs (see Christopher et al. [162] for a thorough review on this subject). Briefly, the droplet size is largely dictated by dimension of the channel supplying the monomer or prepolymer stream and larger flow rates in the focusing mineral oil will lead to smaller droplets. Confocal microscopy was next employed to evaluate the dispersion of TMV throughout the particles. Both the reconstituted 3-D and z-scan (captured at the particle center) images of the TMV-encapsulated microparticles in Figures 3.2e and f confirm uniform distribution of TMVs throughout the microparticles. Combined, these results illustrate rapid microfluidic fabrication of hybrid microparticles containing fluorescently labeled TMV nanotemplates that are uniformly distributed throughout PEG matrices, via FFD droplet-based particle formation.

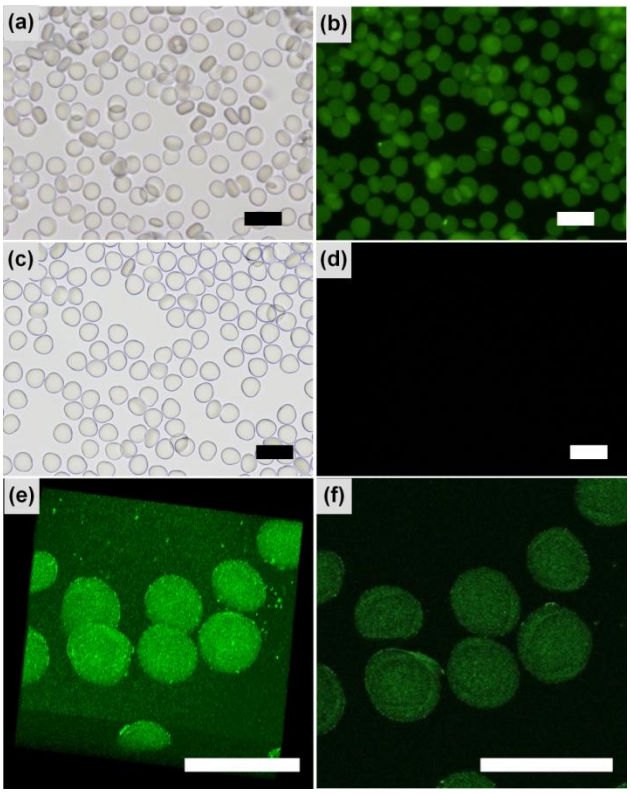

Figure 3.2. Microparticles containing fluorescently labeled TMV nanotemplates.
(a,c) Brightfield and (b,d) fluorescence micrographs of microparticles with and without fluorescently labeled TMV, respectively. (e) Reconstituted 3-D and (f) center z-scan confocal images of microparticles containing fluorescently labeled TMV. The scale bars represent 100 μm.

3.3.2 Fabrication of Janus Microparticles with TMV

Next, we demonstrate fabrication of Janus microparticles containing fluorescently labeled TMV nanotemplates, as shown in Figure 3.3. A microfluidic FFD specific for the fabrication of Janus microparticles contains two separate polymer streams that form each side of the Janus particles, as illustrated in the schematic diagram of Figure 3.3a. For this study, one stream contained PEG-DA solution while the other contained fluorescently labeled TMV within PEG-DA solution. The Janus particle fabrication procedure takes advantage of

laminar flow by photopolymerizing the Janus droplets before significant mixing occurs within the droplets. The brightfield micrograph of Figure 3.3b shows Janus particles with equally consistent particle fabrication similar to that for the non-Janus particles shown in Figures 3.2a and c. The fluorescence micrograph of Figure 3.3c clearly shows that only one side of the Janus particles contains uniform fluorescence. This result confirms both spatial confinement and uniform distribution of the encapsulated TMV afforded by the laminar nature of the microfluidic flow. Combined with the generality of this covalent conjugation scheme of the fluorescent marker molecules (e.g. rhodamine [6], Cy3^{TM} and Cy5^{TM} [7], and fluorescein [141]) to the cysteines, the result shown here suggests a simple means to fabricate hybrid particles with multiple small molecule components in spatially discrete regions within a single entity. Overall, this result demonstrates rapid and consistent fabrication of Janus particles as well as the ability to form multifunctional particles with discrete regions of encapsulated TMV nanotemplates.

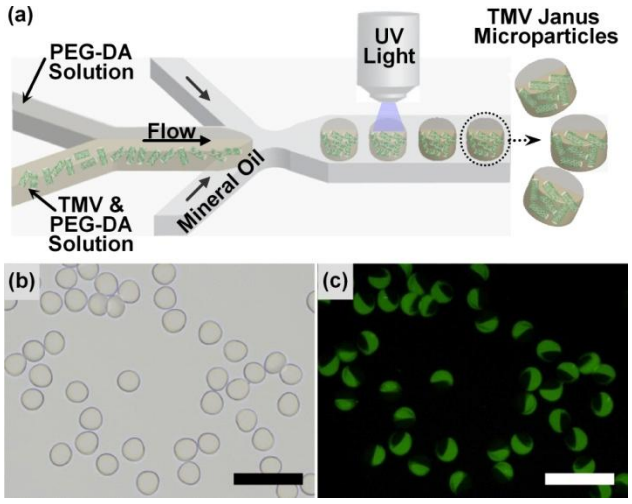

Figure 3.3. Microfluidic fabrication of Janus microparticles containing fluorescently labeled TMV nanotemplates.
(a) Schematic diagram of Janus particle synthesis in a microfluidic flow-focusing device. (b) Brightfield and (c) fluorescence micrographs of Janus microparticles with one side of the particles containing fluorescently labeled TMV.

3.3.3 Fabrication of Microparticles with Pd-TMV Complexes

As shown in Figure 3.4, we next demonstrate microfluidic fabrication of hybrid microparticles with TMV-templated palladium (Pd) nanoparticles directly embedded in the PEG-based polymer matrix. Pd nanoparticles formed with (Figure 3.4a) and without (Figure 3.4b) TMV nanotemplates are shown for identical conditions of 3 mM Pd precursor and 15 mM hypophosphite reducer. Average particle sizes are drastically different in these two cases (5 nm versus 10 nm), clearly demonstrating the utility of TMV templates, which provide ample adsorption sites for particle nucleation leading to substantially smaller particles [117]. Furthermore, the Pd nanoparticles spontaneously aggregated (Figure 3.4b) in the absence of TMV nanotemplates or surfactants under the synthesis conditions employed. Meanwhile, Pd-TMV complexes remained well-dispersed

and the TMV nanotemplates maintained their overall tubular structure. In addition, the Pd-TMV complex has shown to be highly stable through extensive rinsing, drying, and prolonged storage under ambient conditions [157].

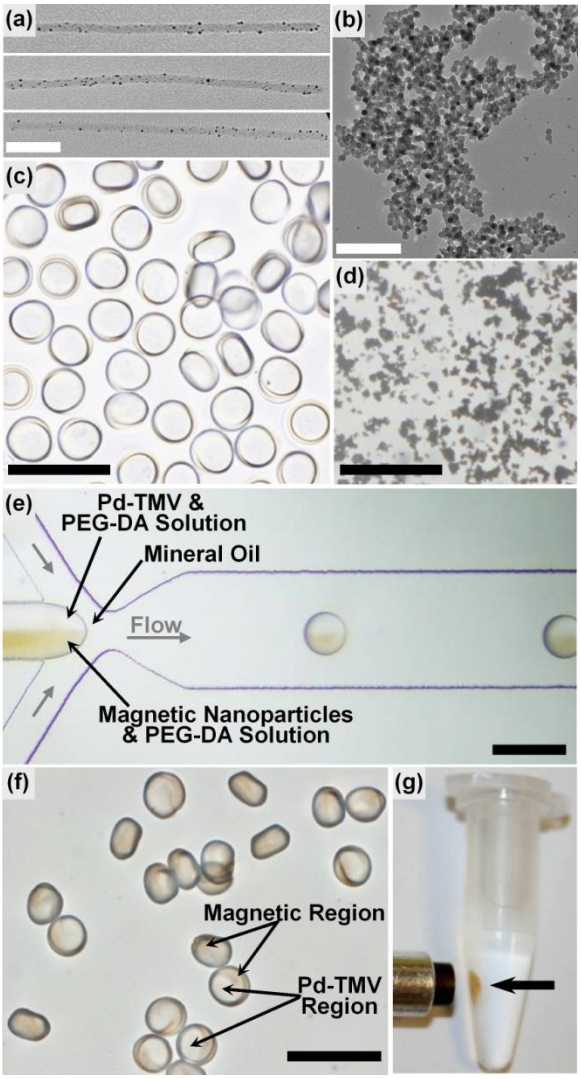

Figure 3.4. Microfluidic fabrication of palladium (Pd) -TMV-PEG-hybrid microparticles.

TEM images of Pd nanoparticles formed (a) on TMV nanotemplates and (b) in bulk solution without TMV. Brightfield micrographs of (c) microparticles containing Pd-TMV complexes, (d) Pd nanoparticle aggregates in a microfluidic device, (e) microfluidic flow-focusing device (FFD) specific for fabrication of Janus microparticles, and (f) Janus microparticles containing Pd-TMV and magnetic nanoparticles. (g) Photograph of Janus particles attracted to a small magnet. The white scale bars in (a) and (b) represent 100 nm and the black scale bars in (c) to (g) represent 100 µm.

The brightfield micrograph of Figure 3.4c shows PEG hydrogel microparticles containing Pd-TMV complexes (approximately 25 pg TMV per particle) with high consistency and uniformity similar to fluorescein-conjugated TMV-PEG particles (Figures 3.2a and 3.3b). Meanwhile, Figure 3.4d shows that Pd-PEG mixtures without TMV templates quickly precipitated and clogged the microfluidic device before photopolymerization. This observation further confirms the advantage of TMV as a nanotemplate, which enables uniform distribution of the Pd nanoparticles within the microparticles without any visible phase segregation.

In Figures 3.4e to g, the multifunctional capability of Janus microparticles containing Pd-TMV and magnetic nanoparticles in two distinct phases is demonstrated. A microfluidic FFD containing two separate streams of different polymer solutions for fabrication of Janus particles (Figure 3.3a) was employed to co-flow Pd-TMV-PEG-DA solution and a magnetic nanoparticle-PEG-DA solution to form droplets. As shown in Figure 3.4e, the laminar nature of the microfluidic flow enables the Pd-TMV-PEG-DA stream (clear) and magnetic-PEG-DA stream (brown) to remain separated. These droplets were photopolymerized with UV light to form multifunctional Janus microparticles as shown Figure 3.4f.

While the Janus particle symmetry does not remain consistent throughout polymerization, each polymer phase containing Pd-TMV complexes or magnetic nanoparticles remains as discrete regions within the particles, as indicated by the arrows in Figure 3.4f. We believe this subtle flaw rises from a difference in the

rate of polymerization between the two streams. Importantly, these Janus microparticles can provide a multifunctional capability that combines the potential applications of Pd-TMV complexes and magnetic nanoparticles in one entity. For example, Figure 3.4g shows simple magnetic separation of these particles via the magnetic nanoparticles within the hydrogel matrix on one side of the particles. Overall, these results demonstrate rapid fabrication of uniform PEG microparticles containing Pd-TMV complexes as well as magnetic nanoparticles via direct embedding with a microfluidic FFD.

3.3.4 Catalytic Activity of Pd-TMV-PEG Hybrid Microparticles

Finally, the Pd-TMV complexes encapsulated in PEG microparticles provided catalytic activity for the dichromate reduction reaction, as shown in Figure 3.5. Different quantities of microparticles containing Pd-TMV complexes were resuspended into 0.3 mL reaction mixtures of 0.1 mM dichromate, the source of Cr(VI), and 100 mM sodium formate, the electron donor for dichromate reduction, to carry out the reaction. A UV-visible spectrophotometer was employed to monitor the reaction at 350 nm, the absorption maximum of dichromate ion as reported in a previous study [151]. The conversion of dichromate catalyzed by microparticles with a range of Pd loading (1-3 μg) was determined over a 1 h time period, as shown in Figure 3.5a. Microparticles with the largest quantity of Pd (3.1 μg) yielded 92% conversion within 30 min and reached near-complete conversion within 1 h. Meanwhile, lower Pd loading yielded slower conversion as expected. Furthermore, the Pd-TMV microparticle batch yielding 2 μg of Pd and aged for 1 week in ambient conditions exhibited

comparable conversion to freshly prepared particles, strongly indicating the stability of the microparticles. The bottom two curves in Figure 3.5a show that both negative control samples (TMV-PEG and PEG microparticles) yielded no catalytic activity under the conditions examined. This clear difference in the conversion rate demonstrates the catalytic activity of the microparticles containing Pd-TMV complexes.

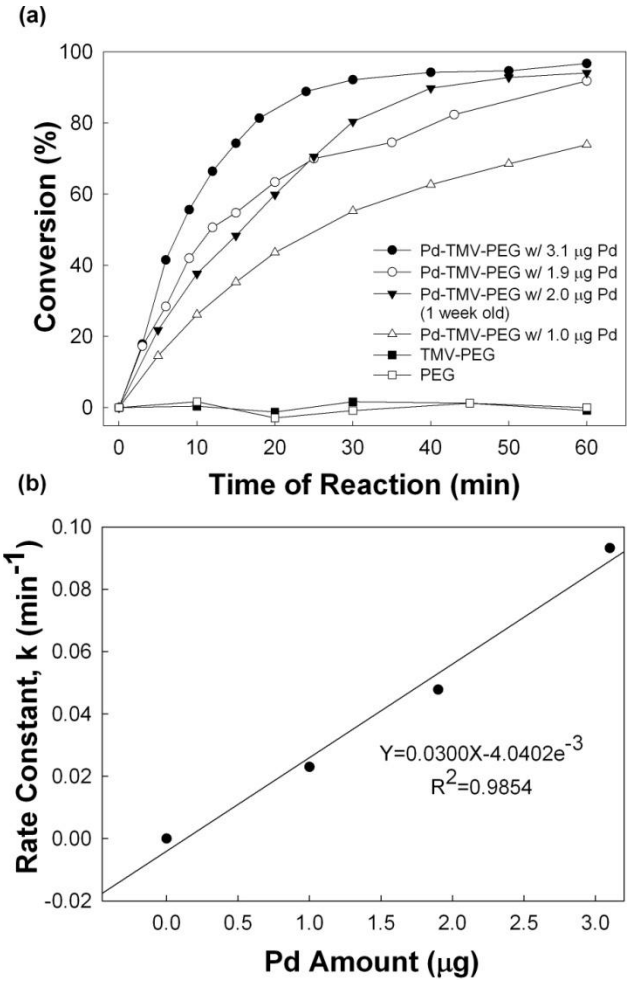

Figure 3.5. Catalytic activity of PEG microparticles containing Pd-TMV complexes for dichromate reduction.
(a) Conversion of dichromate catalyzed by microparticles containing 1-3 μg of Pd from the Pd-TMV complexes. (b) Plot of first-order reaction rate constants, k (min^{-1}) versus the total quantity of Pd within the microparticles from the Pd-TMV complexes. Straight line represents data fitting result from the linear regression.

To further quantify the catalytic versus Pd amount, a first-order kinetics analysis was conducted to determine the reaction rate constants, k (min^{-1}) and to further quantify the catalytic activity versus Pd amount, as previously reported [151]. As shown in Figure 3.5b, the reaction rate constants exhibited a linear relationship to the Pd loading amount. In addition, all of the conditions examined

followed simple first-order batch reaction kinetics (data not shown), suggesting the utility of the microscale carriers for controlled catalyst loading. Furthermore, the rate constants shown in Figure 3.5b exhibit comparable or higher values than surface-displayed Pd nanoparticles reported previously in a similar study [151], suggesting uniform distribution of Pd-TMV complexes that appeared to be readily accessible to the reactants. In summary, the dichromate reduction reaction study demonstrates the catalytic activity and stability of microparticles containing Pd-TMV complexes. These results indicate that the microparticles provide a stable and simple-to-handle carrier for Pd-TMV complexes while the TMV nanotemplates provide a platform for facile synthesis and dispersion of small and catalytically active Pd nanoparticles.

3.4 CONCLUSIONS

A procedure for encapsulating functionalized TMV nanotemplates in hydrogel microparticles was presented in this chapter. These particles offer highly porous 3D networks for immobilizing functionalized viral assemblies while still maintaining the function and structure of the hybrid nanostructures. Additionally, microfluidics offers an efficient route to rapidly fabricate monodisperse hydrogel particles along with the ability to precisely tune microparticle size and morphology.

To generate the viral-synthetic hybrid microstructures, droplets of functionalized TMV nanotemplates suspended in a PEG-DA solution were first formed with a microfluidic flow-focusing device, and then photopolymerized with

UV light to form microparticles. Uniform distribution of TMV nanotemplates throughout the microparticles was confirmed with fluorescence and confocal microscopy images of microparticles containing fluorescently labeled TMV. The functionality of TMV nanotemplates following encapsulation within microparticles was also confirmed through the dichromate reduction reaction, where microparticles containing Pd-TMV complexes provided catalytic activity. Finally, the potential fabrication of multifunctional microparticles was illustrated through Janus microparticle formation, which contained magnetic nanoparticles embedded in one side. It was shown that these Janus particles could be easily separated from bulk solution with a magnet. Overall, these results demonstrate a method for immobilizing functional viral assemblies in a readily usable and stable 3D format. Combined with enhanced thermostability of Pd-TMV complexes [163], this fabrication method presents robust and stable viral-synthetic hybrid entities offering unique advantages in applications such as catalysis or biosensing where well-dispersed and readily accessible functionalities from nanomaterials are highly desired.

4 DNA-CONJUGATED MICROPARTICLES VIA REPLICA MOLDING

4.1 INTRODUCTION

While microfluidics provides rapid and continuous fabrication of hydrogel microparticles, the procedure has limitations. These include the requirement of rapid polymerization without deformation (maximum exposure time is on the order of milliseconds), low viscosity preparticle solution properties as a result of the need for consistent flow within the microfluidic channels, and minimal adherence to channel walls to prevent clogging of the microfluidic devices [12-14]. Alternatively, photolithographic batch-fabrication provides high-throughput fabrication with well-defined shapes down to the submicrometer level though it is costly and requires extensive equipment and software needs, as described in Chapter 1. Meanwhile, soft-lithographic fabrication of polymeric structures via replica molding (RM) has gained substantial attention due to many inherent advantages rising from the batch-processing based nature of the fabrication procedure, as also described in Chapter 1. RM advantages include such as a simple, robust, and inexpensive procedures as well as scalability and reliable duplication of complex structures with nanometer resolution. Fabrication of uniform probe DNA-conjugated hydrogel microparticles with dimensions relevant to high throughput biosensing has not been demonstrated via RM. As such, the

results in this chapter demonstrate batch-fabrication of DNA-conjugated hydrogel microparticles via RM and highlight several critical parameters important for ensuring robust, uniform, consistent and well-controlled fabrication.

As shown in the schematic diagram of Figure 4.1a, fabrication of ssDNA-conjugated poly(ethylene glycol) (PEG)-based microparticles via RM consists of first placing preparticle solution into PDMS micromolds (Step 1). Step 2 involves covering the filled micromolds with a PDMS-coated glass cover. Next, the micromolds are exposed to UV light for photopolymerization (Section 1.2.2) as shown in Step 3 of Figure 4.1a. Finally, Step 4 depicts resulting microparticles of different shapes for hybridization with target nucleic acids in either a 2D in-mold or 3D suspension array format. As shown in the fluorescence micrograph and SEM image of Figures 4.1b and c, practically unlimited dimensions and shapes of uniform particles can be fabricated in a single batch.

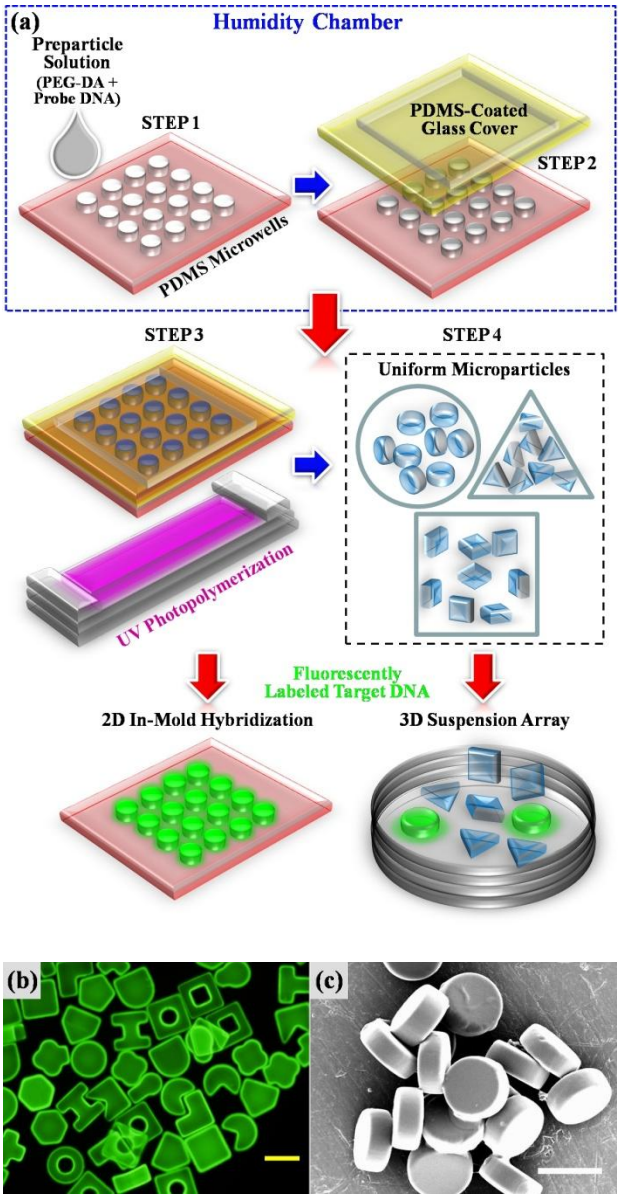

Figure 4.1. DNA–conjugated microparticle fabrication via replica molding (RM) for hybridization assays.
(a) Schematic diagram illustrating the batch-processing based RM procedure for production of DNA-conjugated microparticles. (b) Fluorescence micrograph of various shaped microparticles upon hybridization with fluorescently labeled target DNA. The yellow scale bar represents 100 μm. (c) Scanning Electron Microscopy (SEM) image showing consistent shape and dimension of disc-shaped microparticles fabricated via RM. The white scale bar represents 50 μm.

Critical parameters required for robust, uniform, consistent, and well-controlled fabrication of ssDNA-conjugated PEG-based microparticles include humidity as well as PEG-diacrylate (DA), probe DNA, and photoinitiator (PI) concentrations. Their effects on the overall fluorescence and penetration depth of target DNA are examined via fluorescence and confocal microscopy. First, minimizing rapid evaporation is found to be an important factor for uniformity. Second, PEG-DA concentration was found to substantially impact the penetration depth of target DNA, leading to significant differences with the accessibility of probe DNA. Third, optimal fabrication conditions are found to yield consistently uniform particles and femtomole quantity detection. Combined, these findings represent a significant step toward simple and robust procedures to manufacture highly uniform and high capacity nucleic acid hybridization assay particles in a controlled manner. We envision that the results and the fabrication methods presented in this study can be readily adapted to a variety of other systems for facile fabrication of potent biosensing or functional particles.

The work presented in this chapter was completed in collaboration with Chang-Hyung Choi, who fabricated all of the microparticles used in this study. Dr. Yan Lin also provided helpful guidance during the early stages of this work. My contribution to this work consisted of completing all of the hybridization experiments between the microparticles and fluorescently labeled target DNA. I also completed all of the imaging work, which included fluorescence and confocal microscopy, as well as scanning electron microscopy (SEM). All of the problem solving and strategizing for this work involved equal contribution between Mr.

Choi and myself. Mr. Choi's main contribution was knowledge and experience with particle fabrication while my main contribution was knowledge and experience with DNA hybridization with microparticles. The chapter content was reproduced from Lewis, Choi, Lin, Lee, Yi, *Analytical Chemistry*, 2010 [164].

4.2 MATERIALS AND METHODS

4.2.1 Materials and Experimental Conditions

Poly(ethylene glycol) diacrylate (PEG-DA, M_n=700), PEG (M_w=200), and 2-hydroxy-2-methylpropiophenone (Darocur 1173, photoinitiator (PI)) were purchased from Sigma-Aldrich (St. Louis, MO). Probe DNA sequences (Table 4.1) with a 5' end Acrydite™ modification were purchased from Integrated DNA Technologies (Coralville, IA) and target DNA sequences (Table 4.1) with a 5'end fluorescein isothiocyanate (FITC) modification were purchased from Gene Probe Technologies (Gaithersburg, MD). All of these materials were used without further purification.

Table 4.1. Probe and Target DNA Sequences for the Microparticle Shapes

Shape	Probe DNA Sequences*
Circle	5'-ATG ATG ATG ATG ATG ATG-3'
Square	5'-CAC TAC CGA TAC GTA CTC AG-3'
Triangle	5'-TTT TTC GGC AGG TCG GTA AC -3'

Shape	Target DNA Sequences†
Circle	5'-CAT CAT CAT CAT CAT CAT-3'
Square	5'-CTG AGT ACG TAT CGG TAG TG-3'
Triangle	5'-GTT ACC GAC CTG CCG AAA AA-3'

*Probe DNA sequences are all Acrydite™ modified at the 5'end.
†Target DNA sequences are all modified with fluorescein isothiocyanate (FITC) at the 5'end.

The composition of the preparticle solution was as follows: 20-60% (v/v) PEG-DA, 10% PEG 200, 0.5-3% PI, 10% Probe DNA (1-100 μM final concentration), and 18-58% TE Buffer (10 mM Tris, pH 8.0, Sigma-Aldrich and 1 mM EDTA, Sigma-Aldrich) containing 0.02% (v/v) of 10% (w/w) sodium dodecyl sulfate (SDS, Sigma-Aldrich). The humidity controlled environment consisted of a plastic glove box (Thermo Fisher Scientific) containing a 0.5 gallon ultrasonic humidifier. The humidity was manually controlled based on readings from a standard laboratory Traceable™ hygrometer/thermometer (VWR). An environment of 90% relative humidity was maintained for microparticle fabrication.

4.2.2 Microparticle Fabrication

The four major steps of soft lithography, as described by others [16], were followed to prepare the microparticles. Briefly, AutoCAD was used to design the shaped patterns. High-resolution printing was used to generate photomasks on

transparency films for fabrication of silicon masters with photolithography. PDMS elastomeric micromolds were formed with Sylgard 184 (Dow Corning) following a 48 h cure at 65 °C. Finally, microparticles were fabricated from the PDMS elastomeric micromolds via replica molding (RM).

The details of the RM procedure used for this work are as follows: Preparticle solution (~75 μL) was first placed on the surface of the PDMS micromolds (1600 wells per 1 cm × 1 cm mold). Disposable plastic pipette tips were then used to rub the molds to remove air bubbles in the microwells. The excess preparticle solution was simply removed by a pipette tip and reserved for reuse in subsequent batches of particles requiring the same preparticle formulation. The filled PDMS micromolds were then sealed with a glass slide coated with a thin layer of PDMS obtained via spin-coating for 30 s at 2000 rpm. A square section (same size as the microwell square region within the micromold) of PDMS was removed from the glass slide to provide a small gap between the glass surface and the top portion of the microwells. The sealed micromolds were then placed on an aluminum mirror (Thorlabs, Newton, NJ) and exposed to 365 nm UV light with an 8 W handheld UV lamp (Spectronics Corp., Westbury, NY) for 15 min. The polymerized particles were released from the microwells by first physically bending the mold, then placing water containing 0.5% (v/v) Tween 20 on the mold surface. The microparticles were collected by pipetting up and down a few times before transferring into a storage vial. Particle removal with water was repeated 3 times for complete collection of particles.

4.2.3 Hybridization Procedure

Before hybridization, microparticles were rinsed with 5 × saline sodium citrate (SSC) buffer (75 mM sodium citrate, 750 mM sodium chloride, pH 7.0) containing 0.05% (v/v) Tween 20. The rinsing process involved pipetting the particles in solution to mix, then allowing particles to settle to the tube bottom. The supernatant was removed and the wash procedure was repeated 4 times. For hybridization, the microparticles (maximum number of particles per batch ~1000) were placed in solution with 200 nM target DNA (Table 4.1) in a total volume of 100 μL. Following hybridization for 30 min on a rotator at room temperature, unbound target DNA was rinsed 5 times using the rinsing procedure described above with gravity settling. This 30 min hybridization provided sufficient time for consistent signals [37, 165], while hybridization of short DNA strands in hydrogel formats is rapid and reaches saturation within 10 min (data not shown).

4.2.4 Imaging Analysis

The hybridized microparticles were visualized with an Olympus BX51 microscope and a confocal microscope, as described in Section 2.2.4. The depth scan increment was 3 μm for the z-scan confocal images shown in Figure 4.3.

4.2.5 Estimation of the Rate of Water Evaporation

As described by McHale et al. [166], evaporation is the diffusion of a volume of fluid, V, through a liquid-vapor interface where the rate of evaporation is defined as Equation 13. This vector field surface integral consists of the dot product of the gradient of C with a unit vector normal to the interface. The

gradient of C represents the vector coordinate components of the concentration of water. Overall, this integral represents the flux of water at the liquid-vapor interface of the evaporating sample. The diffusion coefficient of water vapor in air is represented by D and the density of water is represented by ρ.

Equation 13

$$\frac{dV}{dt} = -\frac{D}{\rho}\int_S (\nabla \mathrm{C} \cdot \mathrm{n})\, dS$$

The evaporating samples considered for this work are individual droplets (~400 pL in volume containing 60% (v/v) water) of preparticle solution within the microwells of the PDMS micromolds. Assuming the concentration gradient is radially outward and equal to $\Delta C_{sat\text{-}i}/R$, where $\Delta C_{sat\text{-}i}$ is the concentration difference between the surface of the interface and the air and R is the radius of a hemispherical droplet, the equation simplifies to Equation 14.

Equation 14

$$E = \frac{2\pi D}{\rho}\Delta C_{sat-i} R$$

The evaporation rate is proportional to the radius and not the surface area of a droplet. However, Berthier et al. [167] found an exact solution for steady-state evaporation of a flat disk by using an equivalent radius, R_{eq}, for R in Equation 14. The equation for R_{eq} is shown as Equation 15, where S represents surface area.

Equation 15

$$R_{eq} = \frac{2\sqrt{S}}{\pi^{3/2}}$$

The application of this equation may be extended to accommodate compact shapes of surface area, S, as well [167].

Equations 14 and 15 were used to determine the rate of evaporation for water at both ambient (15% relative humidity) and 90% relative humidity conditions, for a flat disc with a radius of 50 µm. The water vapor saturation concentration, C_{sat}, was estimated as a function of temperature (20ºC), using an empirical fit provided by Berthier et al. [167]. Additional constants used to calculate the rate of evaporation were the diffusion coefficient of water vapor in air, 2.5×10^{-5} m^2/s, and the density of water, 997,700 g/m^3 (20ºC). The time for all of the water present in each of microwells (60% of the preparticle solution) within the PDMS molds to evaporate was determined with the evaporation rate value and the estimated volume of water in the preparticle solution (60% of 400 pL).

4.2.6 Equilibrium Binding Model

An equilibrium binding relationship between two complementary oligomers within hydrogel microparticles may be described by the following equation:

Equation 16

$$T + P \Leftrightarrow TP$$

where T represents target, P represents probe, and TP represents the double stranded complex. This relationship has been considered by others previously [33, 37]. Assuming $[T]_o >> [P]_o$, Equation 17 is obtained with equilibrium constant, K_d.

Equation 17

$$[TP] = \frac{[P]_o[T]_o}{K_d + [T]_o}$$

The initial target DNA concentration in the bulk solution is represented as $[T]_o$ while the initial probe DNA concentration and the target-probe duplex in the hydrogel matrix of the particles are represented as $[P]_o$ and [TP], respectively. A double reciprocal plot (also known as a Lineweaver-Burk plot) may be generated to determine the constants K_d and $[P]_o$ from the linearized equation, as shown in Equation 18.

Equation 18

$$\frac{1}{[TP]} = \frac{K_d}{[P]_o[T]_o} + \frac{1}{[P]_o}$$

It is important to note that $[P]_o$ represents the probe concentration within the microparticles and not bulk concentration.

To generate the dashed red curve of Figure 4.8g, the experimental data was first plotted as a double reciprocal plot, described by Equation 18, where the fluorescence intensity was assumed to be proportional to the double stranded complex, [TP]. From this plot, the constants K_d and $[P]_o$ were found to be 228 nM and 139 nM, respectively. These constants were then used with Equation 17 to generate the dashed red curve shown in Figure 4.8g. At low target concentrations, the assumption $[T]_o >> [P]_o$ is no longer valid and the response was linear under the conditions examined for this work. As such, the dashed red line in the inset of Figure 4.8g was generated from a linear fit of the low target concentration data.

4.3 RESULTS AND DISCUSSION

4.3.1 Minimizing Negative Effects from Evaporation

One of the most important practical considerations toward monodisperse microparticle fabrication by replica molding (RM) is preventing rapid evaporation of small volume fluids. As shown in Figure 4.2a, probe DNA-conjugated microparticles prepared in ambient laboratory conditions (15% relative humidity, 21 ℃) appear similar in brightfield micrographs (and SEM image of Figure 4.1c). Yet, the fluorescence micrograph in Figure 4.2b reveals significant non-uniformity upon hybridization with fluorescently labeled target DNA.

Fluorescence micrographs of particles in molds following in-mold hybridization with target DNA shows that this non-uniformity arises largely from rapid evaporation of water in the preparticle solution, particularly at the outer region of the molds (Figure 4.2c). Specifically, a substantial portion of water in the 400 pL PEG-DA/probe DNA mixture can evaporate from each microwell within seconds at ambient conditions [168]. For this system, evaporation mainly occurs during removal of excess preparticle solution and before placement of a PDMS-coated glass slide to seal the microwells (Figure 4.1a, between Step 1 and 2). As a result, the time spent between Steps 1 and 2 at ambient conditions has substantial impact on the uniformity and fluorescence; for example, samples exposed in ambient conditions for 5 s had dramatically higher uniformity than those exposed for 30 s (data not shown). Evaporation of a small fraction of water may lead to substantial loss of overall fluorescence by consequentially increasing the PEG-DA concentration in the preparticle solution (shown in Figure 4.3).

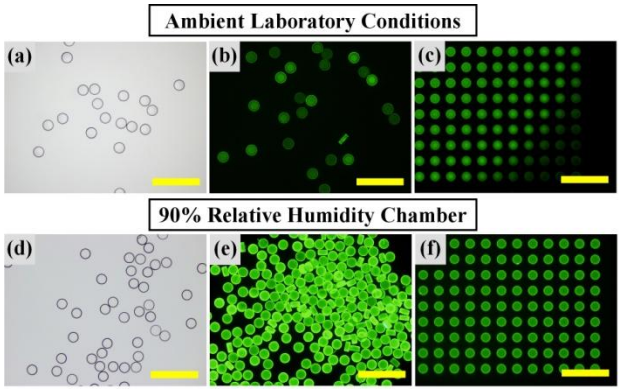

Figure 4.2. Minimizing negative effects from evaporation.
Brightfield micrographs (a,d) show similar appearances from particles prepared under different environments. Fluorescence micrographs following hybridization with fluorescently labeled target DNA (b,e) illustrate how evaporation of water from microwells within the micromolds significantly affects the overall fluorescence and uniformity. Fluorescence micrographs following in mold-hybridization with fluorescently labeled target DNA (c,f) identifies major sources of nonuniformity, and illustrates a simple method for examining detailed microparticle formation and characteristics based on their locations within molds. Scale bars represent 500 μm.

To quantify the effects of evaporation on the RM fabrication technique for hydrogel microparticles, the time for water to evaporate from the preparticle solution mixture within the microwells of the PDMS micromolds in the ambient conditions of the lab was estimated as described in Section 4.2.5. The preparticle solution contained 60% water, mainly from the probe DNA solution and TE buffer. Since each microwell contained ~400 pL of preparticle solution, approximately 240 pL of the preparticle solution was water. At ambient conditions, this volume of water was found to evaporate in 8 s. Since this evaporation time is for pure water, the actual evaporation time of water from the preparticle solution is longer because the other 40% of the preparticle solution consisted mainly of the prepolymer, PEG-DA, and PEG, each having much lower

vapor pressures than water (Raoult's law). Both edge and array effects of the 1600 microwell PDMS mold also impact the actual evaporation rate of water within each individual microwell. For example, Berthier et al. [167] describe how the diffusion of water vapor not only limits the evaporation rate of a liquid, but also the homogenization of the environment. Microwells located at the edge of the micromold will undergo extensive evaporation in comparison to the interior wells of the mold, especially when the ratio of the evaporating surface relative to the total surface of the micromold increases. The overall concentration gradient driving the evaporation is greatest at the edges of the micromold [167, 169]. This information explains why micromolds, which were exposed in ambient conditions for 5 s had dramatically higher uniformity than those exposed for 30 s, as mentioned previously.

Completing Steps 1 and 2 of Figure 4.1a in a high humidity chamber (90% relative humidity) yielded highly uniform fluorescence upon hybridization, particularly for particles on the outer edge of the mold, as shown in Figures 4.2d to f. At 90% relative humidity, the evaporation time for 240 pL of pure water is approximately 70 s (Section 4.2.5). This evaporation time is substantially longer than the 8 s required for the same volume of water to evaporate in ambient lab conditions, suggesting that the 90% relative humidity chamber was sufficient for minimizing evaporation of water from the preparticle solution during Steps 1 and 2 of the fabrication procedure shown in Figure 4.1a. Additionally, implementing use of a humidity chamber as part of the fabrication strategy was straightforward and may be tailored for large scale fabrication without arduous or costly

equipment. Condensation of water on or within the micromold at the 90% relative humidity condition was not observed to be problematic for the RM fabrication procedure.

The results shown in Figure 4.2 also suggest that in-mold hybridization (Figures 4.2c and f) with target DNA as small marker molecules may provide a simple route to examine detailed microparticle formation and characteristics based on their locations within the mold. Standard optical microscopy and SEM are the most common tools used to evaluate the features and characteristics of microparticles. Additionally, microparticles fabricated in a batch format are usually removed from their respective molds prior to analysis. However, examination of microparticles based on their location when fabricated in a mold may be useful as we found with evaporation of our system.

While RM offers an inherently simpler and more robust particle fabrication procedure than flow lithography techniques, exposure to low humidity environments during fabrication results in dramatically poor uniformity as well as probe DNA conjugation capacity, two important aspects for facile biosensing. Combined, these results illustrate a simple means to minimize negative effects of rapid evaporation for improved uniformity, and suggest the potential utility of in-mold hybridization for evaluating microparticles.

4.3.2 Effects of PEG-DA Concentration on Target DNA Hybridization

We next examined the effect of PEG-DA concentration on total fluorescence and penetration depth upon hybridization with target DNA, as shown in Figure 4.3. For this, probe DNA-conjugated particles were fabricated with a

range of PEG-DA concentrations (20-60% (v/v)) while all of the additional components in the preparticle solution remained identical. Upon hybridization with 200 nM complementary target DNA, total fluorescence and 2D profiles of the particles were examined via fluorescence and confocal microscopy.

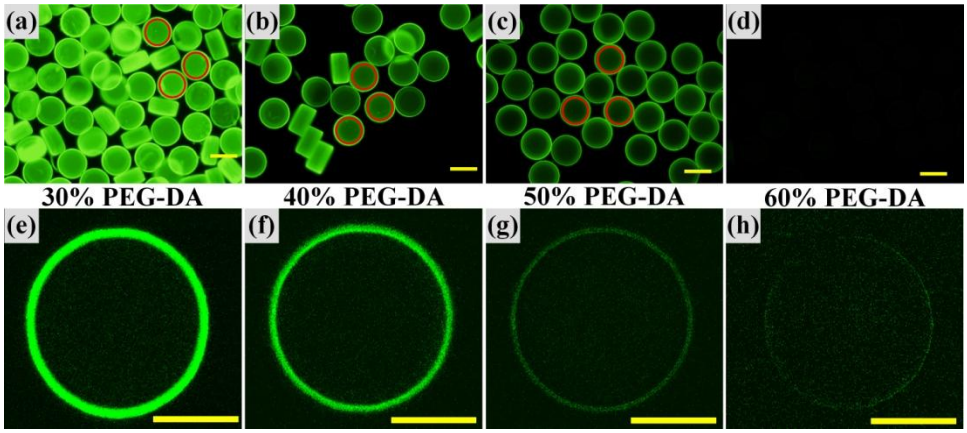

Figure 4.3. Effects of PEG-DA concentration on target DNA hybridization. Fluorescence micrographs (a-d) and confocal z-scan images (e-h) of microparticles following hybridization with target DNA. Scale bars represent 100 μm (a-d) and 50 μm (e-h). Red circles (a-c) represent particle center areas used for fluorescence intensity quantification (Figure 4.4).

The fluorescence micrographs in Figures 4.3a to d show that lower PEG-DA concentration yields brighter fluorescence, with 30% PEG-DA providing the highest and 60% PEG-DA providing negligible fluorescence. Formation of particles containing 20% PEG-DA was incomplete (data not shown). Importantly, fluorescence intensity was relatively uniform among the particles under all the PEG-DA conditions examined, confirming the benefit of simple humidity control (Figure 4.2). In-depth examination of particle fluorescence via confocal microscopy revealed significant differences in the target DNA penetration depth as shown in the 3 μm z-scan images obtained at the center of

each particle (Figures 4.3e to h). Specifically, target DNA appears to penetrate 6 μm into the microparticles containing 30% PEG-DA while fluorescence is confined only to the outer surface of 60% PEG-DA particles. In addition, the fluorescence intensity of these z-scan images differs for each PEG-DA concentration tested, with 30% PEG-DA particles showing the brightest fluorescence.

Increasing the concentration of PEG-DA (and therefore the number of carbon-carbon double bonds) increases the crosslinking density of the hydrogel network, leading to smaller mesh sizes [47]. In this study, fluorescently labeled target DNA served as a small model molecule (6 kDa and linear) to semi-quantitatively examine the hydrogel mesh size. This contour length of this fluorescently labeled ssDNA molecule when fully stretched is approximately 10 to 14 nm in size based on a unit length of 5 to 7 Å for each nucleotide [170-173]. When fully crosslinked, the mesh size of PEG-DA hydrogels is approximately 1 nm [174, 175].

Since oxygen inhibition affects the polymerization kinetics within the exterior 10 μm shell region of the hydrogel microparticles, as described in Section 1.2.2, the crosslinking density and mesh size of the exterior region of the hydrogel microparticles are also affected. The results shown in Figure 4.3 suggest that the mesh size of the exterior shell of these hydrogel microparticles is sufficient to enable diffusion of fluorescently labeled DNA molecules to hybridize with the chemically conjugated complementary probe DNA for PEG-DA concentrations between 30 and 60%. Yet the concentration of PEG-DA directly affects the

quantity and depth of target DNA hybridization. Additionally, since oxygen inhibition does not occur beyond the 10 µm outer shell region of the microparticle, the mesh size is not large enough for the fluorescently labeled target DNA to penetrate deeper within the interior portion of the microparticles.

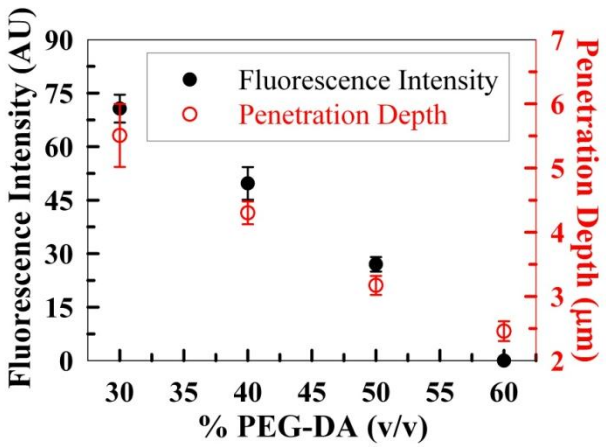

Figure 4.4. Quantitative comparison of fluorescence intensity and penetration depth of target DNA versus PEG-DA concentration.
Error bars represent standard deviation from 5 particles.

To further assess the effects of PEG-DA concentration on the fluorescence intensity and penetration depth quantitatively, average results were plotted as shown in Figure 4.4. Cropped center regions of the microparticles (~98 µm in diameter) were used to quantify the fluorescence intensity in order to avoid artifacts from the outer edges where more surface area from the sidewalls (50 µm height) provides stronger fluorescence (red circles of Figures 4.3a to c). Both data sets exhibit similar linear behavior, with 30% PEG-DA showing the brightest fluorescence and deepest penetration. Similarly, high PEG-DA concentration provides the lowest fluorescence intensity and minimal penetration where target

DNA hybridization is confined to the surface of the particles. For all the cases evaluated, the fluorescence is strictly confined to the 10 μm outer region of the microparticles.

Additionally, these hybridization density and penetration results contrast that for microparticles fabricated via flow lithography, where the presence of oxygen at particle surfaces is critical for continuous operation of microfluidic devices [17, 32, 64, 65]. The requirement of inhibited photopolymerization at the particle surfaces by oxygen diffusion through PDMS for flow lithography processes leads to limited probe DNA density on the particle surfaces. This suggests a potential advantage of the batch processing-based RM technique that allows for high capacity probe DNA conjugation on the microparticle surfaces while not being limited by the constraints posed by the need of continuous flow in microfluidic channels. In conclusion, the results in Figures 4.3 and 4.4 illustrate how PEG-DA concentration affects hybridization density of target DNA as well as its penetration into microparticles.

4.3.3 Effect of Probe DNA Concentration

As shown in Figure 4.5, we next examined the effects of probe DNA concentration on target DNA hybridization. For this, microparticles were prepared with six different concentrations of probe DNA from 1 to 100 μM, hybridized with 200 nM target DNA for 30 min at ambient conditions, and evaluated via fluorescence microscopy. The fluorescence micrographs of Figures 4.5a to d illustrate a gradual increase in fluorescence intensity as probe DNA concentration increased from 1 to 50 μM. The particles were monodisperse and

their fluorescence was relatively uniform in this probe range. Figures 4.5e and f show that the fluorescence intensity reached a plateau at probe concentrations above 50 μM. At these higher probe concentrations, we believe the concentration of probe DNA, which has copolymerized within the hydrogel matrix, is greater than the target DNA concentration available for hybridization, 200 nM. The fluorescence intensity plateaus at probe concentrations above 50 μM because the hybridization of target and probe DNA reaches equilibrium with the available target DNA concentration of 200 nM.

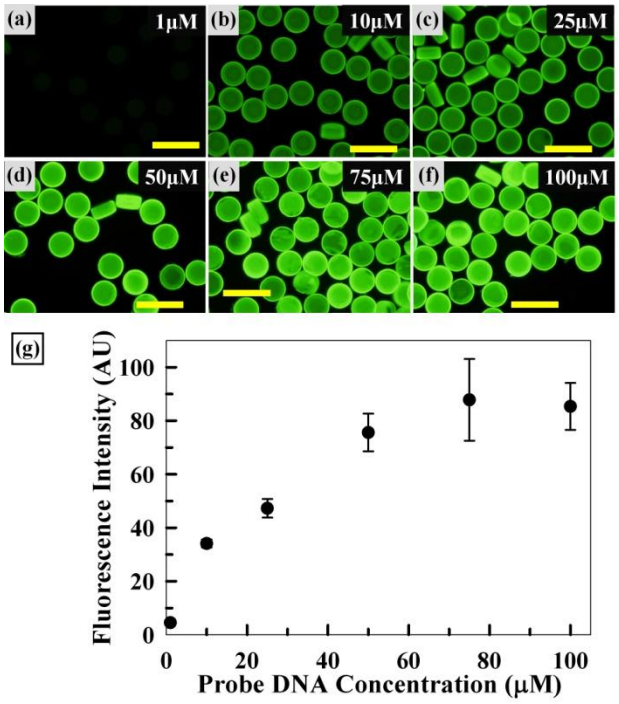

Figure 4.5. Effect of probe DNA concentration.
Fluorescence micrographs (a-f) of microparticles upon target DNA hybridization. Scale bars represent 200 μm. (g) Plot of average fluorescence intensity vs. probe DNA concentration. Error bars represent standard deviation from 5 particles.

To quantitatively compare the fluorescence intensity, average fluorescence intensity from five randomly selected particles was plotted as shown in Figure

4.5g. The plotted data display a linear trend up to a probe DNA concentration of 50 μM with small error bars, further confirming the uniformity of hybridization signals among particles. Within this linear region, the fluorescence intensity, representing the amount of target DNA hybridized to the microparticle, is proportional to the probe DNA concentration. The fluorescence intensity reaches saturation above 50 μM, where there is also less uniformity (i.e. larger error bars). Overall, this result provides a correlation between probe DNA concentration and fluorescence intensity following hybridization with 200 nM target DNA. Based on this result, 50 μM probe concentration was used throughout this study.

4.3.4 Effects of Photoinitiator (PI) Concentration

To evaluate the effects of photoinitiator (PI) concentration, square shaped microparticles with varying PI concentrations between 0.5 and 3% (v/v) were fabricated. Both particle formation and hybridization behavior was examined, as shown in Figure 4.6. First, the brightfield (Figure 4.6a) and fluorescence micrograph (Figure 4.6d) of particles with 0.5% PI show incomplete particle formation as well as minimal fluorescence upon hybridization. This result suggests that the quantity of free radicals generated at this PI concentration is not adequate to fully polymerize the preparticle solution or to incorporate sufficient probe DNA under the polymerization condition employed. At 1% PI, Figures 4.6b and e show complete and uniform particle formation with significant fluorescence. Among all the PI concentrations examined, 2% PI provides the strongest fluorescence intensity, as shown in Figure 4.6c. Finally, 3% PI yielded relatively dim fluorescence upon hybridization compared to lower PI

concentrations, as shown in Figure 4.6f. As expected, particle formation with sufficient PI (2 and 3%) remained consistent with the 1% condition (brightfield images not shown). To further assess the trend of fluorescence intensity quantitatively, the average fluorescence intensities from the particle centers were plotted as shown in Figure 4.6g. This plot confirms that 2% PI concentration provides the highest fluorescence intensity for the conditions examined.

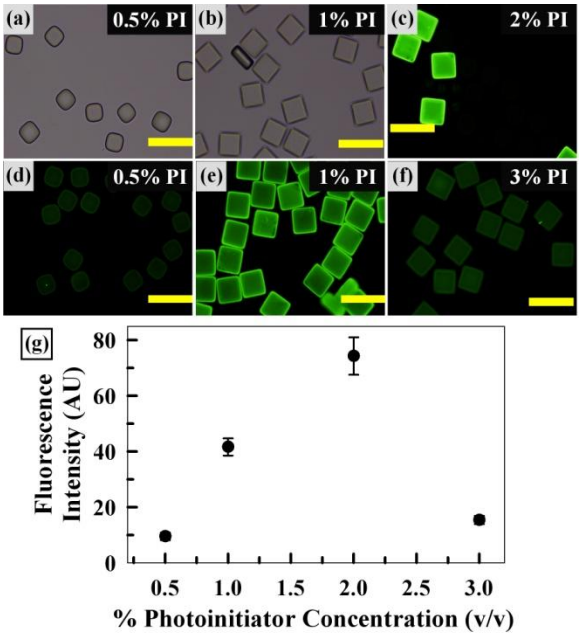

Figure 4.6. Effects of photoinitiator (PI) concentration.
Brightfield (a,b) and fluorescence (c-f) micrographs of microparticles following hybridization with target DNA (200 nM). Scale bars represent 200 μm. (g) Plot of average fluorescence intensity vs. PI concentration. Error bars represent standard deviation from 5 particles.

As shown in Equation 7, the concentration of PI affects the rate of polymerization, R_p, where increasing the concentration of PI increases R_p. Of all the PI concentrations examined, the 3% condition provides the most rapid polymerization kinetics. Interestingly, when considering both the rate of

conversion of monomer double bonds and the inhibition effects of oxygen for hydrogel micropatterns, Biswal and Hilt [52] found that increasing the concentration of PI increased monomer conversion and reduced the effects of oxygen inhibition. The results shown in Figure 4.6, with support from the findings of Biswal and Hilt, suggest that high PI concentration provides rapid polymerization and increases the crosslinking density on the hydrogel microparticle surfaces, despite the inhibition effects of oxygen. Physically, this results in a smaller hydrogel mesh size, which does not accommodate the penetration of 10 to 14 nm fluorescently labeled target DNA to hybridize with probe DNA within the microparticles, providing microparticles with lower levels of fluorescence.

Others describe an important relationship between PI concentration and depth of curing for UV photopolymerization procedures [44, 45, 51]. In particular, Lee et al. [51] derive a model which predicts an optimal PI concentration that maximizes the depth of cure. They also find that high PI concentrations results in lower cure depths. While the relationship between PI concentration and depth of cure is based on UV photopolymerization systems with thick (> 200 μm) samples where UV light attenuates through the sample, the results of these studies demonstrates that increasing PI concentration alters the polymerization kinetics in a way that changes the physical features of the polymerized sample, especially the outer surface. Though UV light attenuation does not occur for this study, the results indicate that PI concentration affects the polymerization kinetics and therefore the microparticle mesh size, particularly on

the exterior surface of the microparticles. A general observation is that small changes in PI concentration can significantly affect the physical features of samples whether or not the sample thickness causes attenuation of UV light. For the hydrogel microparticles examined in this study, lower fluorescence at 3% PI concentration occurred from the inability of target DNA to thoroughly penetrate the tightly crosslinked hydrogel network. Among the PI concentrations examined, 2% PI provided the brightest fluorescence and was used to carry out the remaining studies in this work.

4.3.5 DNA Sequence Specificity

To further confirm the sequence-specific hybridization along with consistency and equivalent capacity among particles, three types of particles differing by probe DNA sequence and shape (Table 4.1) were investigated, as shown in Figure 4.7. All three particle types were mixed and divided into three batches, then hybridized with one of three fluorescently labeled complementary target DNAs. The brightfield micrographs of Figures 4.7a to c show the presence of three uniform microparticle types despite their difference in shape. The fluorescence micrographs of Figures 4.7d to f show that target DNA hybridization occurs only with particles containing complementary probe DNA. Importantly, minimal fluorescence from particles with non-complementary sequences hybridized under ambient conditions and minimal rinsing (i.e. 30 min, room temperature, TE buffer) clearly illustrates a highly selective hybridization assay afforded by the suspension array format with 3D hydrogel scaffolds unlike planar arrays [67, 176]. In addition, the fluorescence images show highly uniform and

consistent fluorescence within each batch of hybridized particles as well as for different shapes. Average fluorescence intensities acquired from the particle centers for each shape (thus sequence) were also compared in a bar graph format, as shown in Figure 4.7g, indicating equivalent hybridization for each shape and sequence evaluated. This result is consistent with previous studies [18, 37, 67, 141] on encoded particle-based suspension assays, and further attests to the robust nature of batch processing-based RM fabrication for rapid and selective assays via 3D hydrogel arrays.

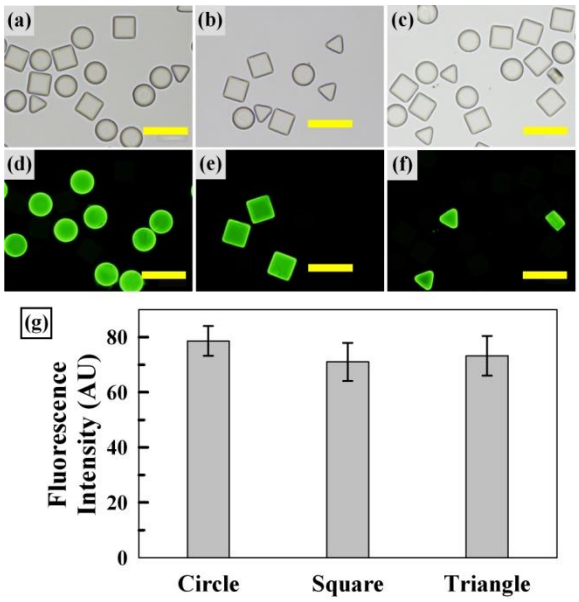

Figure 4.7. Replica molding (RM) sequence specificity.
Brightfield micrographs (a-c) of three microparticle types, all differing by the conjugated probe DNA sequence. Fluorescence micrographs (d-f) following hybridization with fluorescently labeled target DNA (200 nM) complementary to each particle type. Scale bars represent 200 μm. (g) Average fluorescence intensity graph for each particle shape. Error bars represent standard deviation from 3 particles.

4.3.6 Target DNA Sensitivity

Finally, we examined the responsiveness and sensitivity of the DNA-PEG microparticles produced under optimized fabrication conditions for target DNA, as shown in Figure 4.8. Probe DNA-conjugated microparticles were fabricated with 30% (v/v) PEG-DA, 50 μM probe DNA, 2% PI, 10% PEG 200, and hybridized with target DNA concentrations ranging between 0.01 nM and 2 μM. As shown in the fluorescence micrographs of Figures 4.8a to e, fluorescence intensity upon hybridization increased with target DNA concentration. In addition, Figures 4.8e and f show that fluorescence intensity reached saturation above 1 μM. Importantly, all of the micrographs clearly show uniformity among the microparticles and throughout their cross-sections. Overall, these images clearly show that the particles are responsive to target DNA concentrations and that low concentration target DNA is readily detectable.

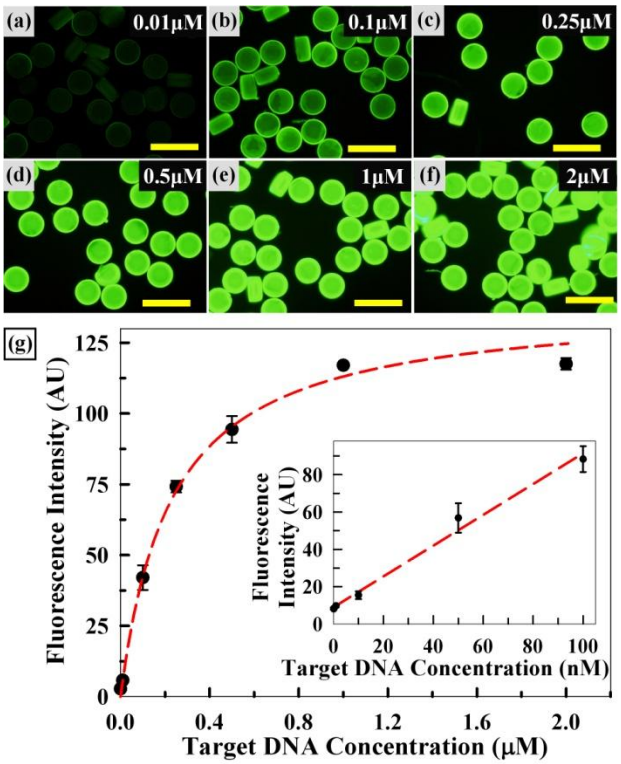

Figure 4.8. Target DNA sensitivity.
Fluorescence micrographs (a-f) of microparticles upon target DNA hybridization. Scale bars represent 200 μm. (g) Plots of average fluorescence intensity vs. target DNA concentration. The dotted red lines indicate the equilibrium binding model and linear fit for the main plot and inset, respectively. Error bars represent standard deviation from 5 particles.

To quantitatively assess the sensitivity, the average fluorescence intensities were plotted and then fitted to an equilibrium binding model (Section 4.2.6), as shown in Figure 4.8g. First, each data point shows a small error bar throughout the target DNA range examined, confirming the uniformity of the particles and the robust nature of replica molding (RM)-based particle fabrication under optimized conditions. Second, the results illustrate typical equilibrium binding behavior where the response is linear at low target concentrations and reaches saturation at high target concentrations, similar to monolayer surface adsorption behavior represented by the Langmuir isotherm. The dashed red curve

in Figure 4.8g represents the equilibrium binding model constructed from the fluorescence intensity measurements via a double reciprocal plot, and indicates a reasonably good fit of the data to the model. The trend of the data suggests that the hydrogel network provides favorable solution kinetics [32] as well as confining nanoenvironments [39] which may enable the probe DNA sites to behave like equal monolayer binding sites for hybridization. Third, the red linear regression line in the inset of Figure 4.8g further indicates the linear response behavior at low target concentrations. The exposure time used to obtain the images of Figures 4.8a to f was relatively low (0.5 s) in order to ensure that the fluorescence was not at a saturating level for the higher target concentrations. Thus the strong fluorescence and saturation obtained at high target concentrations represents the extent of hybridization and not saturation of the microscope camera's CCD detector (Olympus DP70).

Furthermore, distinct uniformity and linear responses down to single nanomolar concentrations (i.e. high femtomole quantities) are readily detectable under the standard conditions employed in this study, involving one fluorescein molecule per target DNA and a 0.5 s exposure time (1 s exposure for Figure 4.8g inset) with a standard epifluorescence microscope. Additionally, the actual time required to reach equilibrium with low concentrations of target DNA is much longer than the 30 min incubation time used for this study [177]. Further examination of longer incubation times with low target DNA concentrations may demonstrate increased sensitivity for these microparticle assays. The sensitivity may be further increased by increasing the probe DNA concentration in the

preparticle solution which should increase the concentration of probe DNA conjugated within the microparticles. In conclusion, the results shown in Figure 4.8 indicate robust, uniform, and sensitive features of particles fabricated via RM for potential biosensing applications based on nucleic acid hybridization.

4.4 CONCLUSIONS

Soft-lithographic fabrication of polymeric structures via replica molding (RM) possesses many inherent advantages including simple, robust, and inexpensive procedures as well as scalability and reliable duplication of complex structures with nanometer resolution. The simplicity of the microparticle fabrication strategy via RM presented in this chapter is highlighted by the use of a handheld UV lamp for photopolymerization rather than requiring delicate alignment and control of a high intensity UV source and other equipment necessary for photolithographic or microfluidic fabrication procedures [12, 18, 155, 178, 179]. In addition, the RM procedure allows for simple collection of particles without the presence of unreacted monomer or prepolymer solution or other immiscible fluids. Extensive rinsing of particles fabricated via photolithography or microfluidics is required due to the presence of unreacted monomer or prepolymer solution or a continuous phase material, such as oil, with the fully polymerized particles [4, 18, 22, 67]. The robust nature of RM arises from the ability to examine of a wide range of parameters while not being limited by the viscosity, phase separation, or flow rate, which must be accounted for with microfluidic methods. Further, the ability to reuse excess preparticle solution

along with all other components (e.g. silicon master molds, PDMS micromolds, etc.) attests to the cost efficiency of this procedure when considering the expense of synthesized probe DNAs for biosensing applications. For the RM procedure described here, 100 µL of preparticle solution will provide over 100 batches (1600 particles per batch) of particles where photolithographic and microfluidic applications would require significantly more preparticle solution to produce the same number of particles.

Several important parameters toward fabrication of uniform DNA-conjugated microparticles were presented in this chapter. Specifically, a simple humidity controlled environment minimized negative effects of rapid evaporation and showed the potential utility of in-mold hybridization for evaluating microparticles. Total fluorescence and 2D profiles of the hybridized particles showed how PEG-DA concentration affects hybridization and target DNA penetration depth. Probe DNA and photoinitiator (PI) concentrations were also examined to evaluate their effects on target DNA hybridization along with particle formation. Clear uniformity, sequence-specificity, and responsiveness down to single nanomolar concentrations (i.e. high femtomole quantities) under the standard conditions employed in this study support the simple, robust, and controllable nature of the replica molding process for fabrication of nucleic acid hybridization assay platforms. We envision that the results presented in this work may be readily scaled-up and/or applied to other systems involving other pre-polymers (e.g. acrylamide, methacrylates, etc.) and low micrometer dimensions for rapid and high throughput assays.

5 CONCLUSIONS AND FUTURE PROSPECTS

Presented in this dissertation were three fabrication strategies for poly(ethylene glycol) (PEG)-based hydrogel microparticles and their utility for exploiting the advantages of viral nanotemplates and DNA oligonucleotides. As described in Section 1.2.1, hydrogel microparticles have several advantages arising from the benefits of a particle-based platform as well as those for hydrogel substrates. These benefits are especially advantageous for nucleic acid hybridization-based assays where the highly porous 3D network of hydrogel microparticles offers more favorable solution kinetics than 2D surfaces. The ability to conjugate Acrydite^{TM} modified probe DNA within the matrix of hydrogels is the key component for enabling nucleic acid hybridization-based assays with microparticles. Additionally, these chemically conjugated DNA oligonucleotides provide other features for the microparticles, as described in Section 1.4. Meanwhile, viral nanotemplates offer high capacity templates where chemical or genetic modifications confer precisely spaced functionalities for synthesis of metal nanoparticles, conjugation of antibodies, proteins, or drugs, among others, as shown in Figure 1.8. Yet, a significant challenge is aggregation of these functional viral nanotemplates and the lack of a method to employ their utility in a readily useable format. The fabrication strategies presented in this dissertation focus to address this need through continuous and batch fabrication of

hydrogel microparticles. Overall, this work demonstrates novel techniques for creating viral-synthetic composite or DNA-conjugated microparticles in a rapid format while enabling exploitation of nanofunctional materials. Applications of this work include biomolecule detection for bioprocess monitoring, disease diagnostics, food safety, biological threat detection, or environmental monitoring. Yet, future work may be completed to further improve the approaches developed and to expand upon the applications of these functional microparticles. The remainder of this chapter discusses these future prospects in more detail.

5.1 MULTIPLEXED AND MULTIFUNCTIONAL HYBRID MICROPARTICLES

In Chapter 2, I described nucleic acid hybridization-based assembly of fluorescently labeled TMV nanotemplates on the outer surface of hydrogel microparticles. The microparticles used for this strategy were fabricated via SFL, which also provides particles containing discrete regions of different chemical functionalities. The multiplexing and multifunctional capabilities of these microparticles may be further examined with a few simple experiments:

First, the potential for functionalizing the sulfhydryl groups on the genetically modified TMV1cys nanotemplate surfaces with antibodies may be investigated. As highlighted in Section 1.3.3, genetically modified TMV nanotemplates (e.g. TMV1cys) offer precisely spaced functional groups at high density. Assuming each functional group may be conjugated with antibody, these nanotemplates may be functionalized at high density. This feature may be

beneficial in comparison to traditional immunoassay techniques that suffer from low signal intensities. For example, Soto et al. demonstrated that fluorescently labeled cow pea mosaic virus (CPMV) enhanced sensitivity for a DNA sensor platform as a result of the brighter fluorescence provided by the fluorescently labeled CPMV scaffold [101]. While antibody functionalization has yet to be demonstrated with TMV (to our knowledge at this point in time), genetically modified cow pea mosaic virus (CPMV), which also displays sulfhydryl groups on the viral capsid outer surface, has successfully been functionalized with antibody [88]. These results by Sapsford et al. demonstrate the potential for functionalizing TMV with antibody using a similar approach with heterobifunctional crosslinkers, such as N-(g-maleimidobutyryloxy) succinimide ester (GMBS). Antibody functionalization of TMV would provide an opportunity to be the first to demonstrate this procedure successfully. Importantly, antibody functionalized TMV would form a high capacity probe for a variety of targets, which is would be especially useful for biosensing applications.

Second, fabrication of microparticles containing discrete regions of different conjugated probe DNA sequences as well as an encoded sample identification region would provide a platform for antibody functionalized and programmed TMV assembly. Multiple batches of TMV could be functionalized with antibodies specific for different targets of interest while TMV could also be programmed to hybridize onto specified regions on the microparticle surfaces. Finally, successful one-pot hybridization of the particles with different targets of interest would demonstrate the significant potential of these multifunctional

hybrid microparticles and their multiplexing capabilities. Direct comparison of these hybrid microparticles to similar microparticles containing antibodies conjugated directly to the probe DNA within the hydrogel matrices may also provide useful information for comparing the utility of the high density coupling sites on the viral nanotemplates to molecules individually conjugated within a hydrogel matrix.

5.2 DIRECT EMBEDDING OF Pd-TMV COMPLEXES

In Chapter 3, I described a microfluidic procedure for direct embedding of functionalized TMV nanotemplates in hydrogel microparticles. This technique enabled rapid fabrication of microparticles containing readily exploitable Pd nanoparticles in a 3D format. Fabrication of Janus particles containing Pd-TMV complexes and magnetic nanoparticles within discrete regions of the microparticles demonstrated the potential for multifunctional microparticles containing functional nanomaterial throughout the matrices of hydrogel microparticles. However, the Janus particle symmetry was not consistent throughout this procedure, as evident in the brightfield image of Figure 3.4f. Additional work, which focuses to ensure that the rates of polymerization are the same for the prepolymer streams containing Pd-TMV complexes and magnetic nanoparticles, could eliminate this flaw from the particle shapes. Part of this work would involve improving the way in which the droplets are photopolymerized within the microfluidic device. Because UV light is exposed only to one side of the disc-shaped droplets, as shown in Figure 3.3a, the UV

intensity is not the same on each side of the droplets. Placement of a reflective material, such as a mirror or aluminum foil may alleviate this problem by providing reflection of UV light to the side of the disc droplet in which UV light is not facing directly. Additionally, the photoinitiator concentrations for each of the prepolymer solutions could be altered in order to match their rates of polymerization. Adjustment of photoinitiator concentrations should be completed in combination an instrument that would provide data on the polymerization rate of each prepolymer solution, such as fourier transform infrared (FTIR) spectroscopy.

In Chapter 3, we also demonstrated catalytic activity of the dichromate reduction reaction with the microparticles containing Pd-TMV complexes. The dichromate reduction reaction is predominantly used for environmental remediation by reducing highly toxic hexavalent chromium (Cr^{6+}) to non-toxic and immobile trivalent chromium (Cr^{3+}). While we demonstrated promising results with PEG-based microparticles containing Pd-TMV complexes, it is also important to consider the stability of the PEG-based microparticles with regard to the desired application. PEG is known for its hydrophilic, biocompatible, and non-fouling properties. While these properties are beneficial for other applications, they may not be perfectly suitable for conditions of hazardous environmental waste. However, the application of microparticles containing Pd-TMV complexes for environmental remediation applications may be better understood by investigating the stability of the PEG-based microparticles compared to an alternative monomer or prepolymer that is known to withstand

harsh environmental conditions. This work would also require examining the functionality of Pd-TMV complexes following encapsulation in the alternative monomer or prepolymer.

5.3 APPLICATIONS OF MICROPARTICLES FABRICATED VIA RM

In Chapter 4, I described the features of batch fabricated and DNA-conjugated microparticles using replica molding. The utility of these batch fabricated particles may be further examined by assembling TMV on these particles via nucleic acid hybridization, as described in Chapter 2. The results of TMV assembly on these microparticles may then be used to directly compare the microfluidic and batch fabricated microparticles. Since the composition of the microfluidic and batch fabricated microparticles is similar, this comparison would provide insight on the similarities and differences between the microfluidic and batch microfluidic fabrication techniques. These insights would provide valuable information when considering the advantage of tailoring microparticles with more specific features for particular applications.

The application of the batch fabricated microparticles described in Chapter 4, may also be examined in more detail. A direct measuring tool for bioprocess monitoring of physiological events, such as transcription and translation, during production of biopharmaceuticals and functional proteins is currently lacking. Batch fabricated microparticles may be used to address this need by investigating their capability for monitoring physiological events in bacterial cell cultivation

processes. This may be achieved by directly assaying mRNA transcription of heterologous protein production. For this procedure, the probe DNA sequences in the microparticles should be complementary to the RNA sequences, which signify protein production or regulation. Hybridization of these DNA-conjugated microparticles with bacterial cell RNA extract will enable the target RNA sequences to bind to the particles. A fluorescently labeled sandwich DNA probe complementary to a different region of the target RNA sequences should provide a detection signal, which may be evaluated with fluorescence microscopy. Additionally, the shape encoding feature of these batch fabricated microparticles may be used to demonstrate the ability to examine multiple target RNA sequences in one-pot while the microparticles shapes provide identification of the samples under examination.

The "glue" capability of the conjugated DNA within the batch fabricated microparticles provides another opportunity further examine the application of these particles. Similar to the 3D nanoarchitectures described in Section 1.4, constructing 3D micro-architectures may also be useful for larger scaled electronic devices or for sophisticated biosensing applications. Creation of 3D micro-architectures would utilize the microparticles as building blocks for complex structures. The DNA sequences conjugated within the microparticles would need to be designed such that they were complementary to one another depending on the desired final structure. Longer DNA sequences or linker DNA may also be required to extend the mobility and number of bases involved for particle-particle hybridization.

6 BIBLIOGRAPHY

1. Choi, C.-H.; Lee, J.; Yoon, K.; Tripathi, A.; Stone, H. A.; Weitz, D. A.; Lee, C.-S., Surface-Tension-Induced Synthesis of Complex Particles Using Confined Polymeric Fluids. *Angew. Chem., Int. Ed.* **2010,** *49* (42), 7748-7752.

2. Dendukuri, D.; Doyle, P. S., The Synthesis and Assembly of Polymeric Microparticles Using Microfluidics. *Adv. Mater.* **2009,** *21* (41), 4071-4086.

3. Choi, C.-H.; Jung, J.-H.; Kim, D.-W.; Chung, Y.-M.; Lee, C.-S., Novel one-pot route to monodisperse thermosensitive hollow microcapsules in a microfluidic system. *Lab Chip* **2008,** *8* (9), 1544-1551.

4. Yuet, K. P.; Hwang, D. K.; Haghgooie, R.; Doyle, P. S., Multifunctional Superparamagnetic Janus Particles. *Langmuir* **2009,** *26* (6), 4281-4287.

5. Meiring, J. E.; Lee, S.; Costner, E. A.; Schmid, M. J.; Michaelson, T. B.; Willson, C. G.; Grayson, S. M., Pattern recognition of shape-encoded hydrogel biosensor arrays. *Opt. Eng.* **2009,** *48* (3), 037201-14.

6. Yi, H. M.; Nisar, S.; Lee, S. Y.; Powers, M. A.; Bentley, W. E.; Payne, G. F.; Ghodssi, R.; Rubloff, G. W.; Harris, M. T.; Culver, J. N., Patterned assembly of genetically modified viral nanotemplates via nucleic acid hybridization. *Nano Lett.* **2005,** *5* (10), 1931-1936.

7. Yi, H.; Rubloff, G. W.; Culver, J. N., TMV microarrays: Hybridization-based assembly of DNA-programmed viral nanotemplates. *Langmuir* **2007,** *23* (5), 2663-2667.

8. Campelo, Juan M.; Luna, D.; Luque, R.; Marinas, José M.; Romero, Antonio A., Sustainable Preparation of Supported Metal Nanoparticles and Their Applications in Catalysis. *ChemSusChem* **2009,** *2* (1), 18-45.

9. Steinmetz, N. F.; Evans, D. J.; Lomonossoff, G. P., Chemical Introduction of Reactive Thiols Into a Viral Nanoscaffold: A Method that Avoids Virus Aggregation. *ChemBioChem* **2007,** *8* (10), 1131-1136.

10. Nam, Y. S.; Magyar, A. P.; Lee, D.; Kim, J.-W.; Yun, D. S.; Park, H.; Pollom, T. S.; Weitz, D. A.; Belcher, A. M., Biologically templated photocatalytic nanostructures for sustained light-driven water oxidation. *Nat. Nanotechnol.* **2010,** *5* (5), 340-344.

11. Li, T.; Wu, L.; Suthiwangcharoen, N.; Bruckman, M. A.; Cash, D.; Hudson, J. S.; Ghoshroy, S.; Wang, Q., Controlled assembly of rodlike viruses with polymers. *Chem. Commun.* **2009,** (20), 2869-2871.

12. Dendukuri, D.; Gu, S. S.; Pregibon, D. C.; Hatton, T. A.; Doyle, P. S., Stop-flow lithography in a microfluidic device. *Lab Chip* **2007,** *7* (7), 818-828.

13. Dendukuri, D.; Pregibon, D. C.; Collins, J.; Hatton, T. A.; Doyle, P. S., Continuous-flow lithography for high-throughput microparticle synthesis. *Nat. Mater.* **2006,** *5* (5), 365-369.

14. Zhao, X. M.; Xia, Y. N.; Whitesides, G. M., Soft lithographic methods for nano-fabrication. *J. Mater. Chem.* **1997,** *7* (7), 1069-1074.

15. Xia, Y. N.; Whitesides, G. M., Soft lithography. *Annu. Rev. Mater. Sci.* **1998,** *28*, 153-184.

16. Qin, D.; Xia, Y. N.; Whitesides, G. M., Soft lithography for micro- and nanoscale patterning. *Nat. Protoc.* **2010,** *5* (3), 491-502.

17. Merkel, T. J.; Herlihy, K. P.; Nunes, J.; Orgel, R. M.; Rolland, J. P.; DeSimone, J. M., Scalable, Shape-Specific, Top-Down Fabrication Methods for the Synthesis of Engineered Colloidal Particles. *Langmuir* **2009,** *26* (16), 13086-13096.

18. Meiring, J. E.; Schmid, M. J.; Grayson, S. M.; Rathsack, B. M.; Johnson, D. M.; Kirby, R.; Kannappan, R.; Manthiram, K.; Hsia, B.; Hogan, Z. L.; Ellington, A. D.; Pishko, M. V.; Willson, C. G., Hydrogel Biosensor Array Platform Indexed by Shape. *Chem. Mater.* **2004,** *16* (26), 5574-5580.

19. Rolland, J. P.; Maynor, B. W.; Euliss, L. E.; Exner, A. E.; Denison, G. M.; DeSimone, J. M., Direct Fabrication and Harvesting of Monodisperse, Shape-Specific Nanobiomaterials. *J. Am. Chem. Soc.* **2005,** *127* (28), 10096-10100.

20. Zhang, H.; Nunew, J. K.; Gratton, S. E. A.; Herlihy, K. P.; Pohlhaus, P. D.; DeSimone, J. M., Fabrication of multiphasic and regio-specifically functionalized PRINT® particles of controlled size and shape. *New J. Phys.* **2009,** *11* (7), 075018.

21. Gratton, S. E. A.; Williams, S. S.; Napier, M. E.; Pohlhaus, P. D.; Zhou, Z.; Wiles, K. B.; Maynor, B. W.; Shen, C.; Olafsen, T.; Samulski, E. T.; DeSimone, J. M., The Pursuit of a Scalable Nanofabrication Platform for Use in Material and Life Science Applications. *Acc. Chem. Res.* **2008,** *41* (12), 1685-1695.

22. Merkel, T. J.; Herlihy, K. P.; Nunes, J.; Orgel, R. M.; Rolland, J. P.; DeSimone, J. M., Scalable, Shape-Specific, Top-Down Fabrication Methods for the Synthesis of Engineered Colloidal Particles. *Langmuir* **2009,** *In Press*, 10.1021/la903890h.

23. Ellington, A. A.; Kullo, I. J.; Bailey, K. R.; Klee, G. G., Antibody-Based Protein Multiplex Platforms: Technical and Operational Challenges. *Clin. Chem.* **2010,** *56* (2), 186-193.

24. Dunbar, S. A., Applications of Luminex® xMAP™ technology for rapid, high-throughput multiplexed nucleic acid detection. *Clin. Chim. Acta* **2006,** *363* (1-2), 71-82.

25. Rubina, A. Y.; Pan'kov, S. V.; Dementieva, E. I.; Pen'kov, D. N.; Butygin, A. V.; Vasiliskov, V. A.; Chudinov, A. V.; Mikheikin, A. L.; Mikhailovich, V. M.; Mirzabekov, A. D., Hydrogel drop microchips with immobilized DNA: properties and methods for large-scale production. *Anal. Biochem.* **2004,** *325* (1), 92-106.

26. Soto, C. M.; Patterson, C. H.; Charles, P. T.; Martin, B. D.; Spector, M. S., Immobilization and hybridization of DNA in a sugar polyacrylate hydrogel. *Biotechnol. Bioeng.* **2005,** *92* (7), 934-942.

27. Fan, A.; Cao, Z.; Li, H.; Kai, M.; Lu, J., Chemiluminescence Platforms in Immunoassay and DNA Analyses. *Anal. Sci.* **2009,** *25* (5), 587-597.

28. Ray, S.; Mehta, G.; Srivastava, S., Label-free detection techniques for protein microarrays: Prospects, merits and challenges. *Proteomics* **2010,** *10* (4), 731-748.

29. Miller, M. B.; Tang, Y.-W., Basic Concepts of Microarrays and Potential Applications in Clinical Microbiology. *Clin. Microbiol. Rev.* **2009,** *22* (4), 611-633.

30. Irizarry, R. A.; Wu, Z.; Jaffee, H. A., Comparison of Affymetrix GeneChip expression measures. *Bioinformatics* **2006,** *22* (7), 789-794.

31. Call, D. R., Challenges and opportunities for pathogen detection using DNA microarrays. *Crit. Rev. Microbiol.* **2005,** *31* (2), 91-99.

32. Fotin, A.; Drobyshev, A.; Proudnikov, D.; Perov, A.; Mirzabekov, A., Parallel thermodynamic analysis of duplexes on oligodeoxyribonucleotide microchips. *Nucleic Acids Res.* **1998,** *26* (6), 1515-1521.

33. Levicky, R.; Horgan, A., Physicochemical perspectives on DNA microarray and biosensor technologies. *Trends Biotechnol.* **2005,** *23* (3), 143-149.

34. Sorokin, N. V.; Chechetkin, V. R.; Pan'kov, S. V.; Somova, O. G.; Livshits, M. A.; Donnikov, M. Y.; Turygin, A. Y.; Barsky, V. E.; Zasedatelev, A. S., Kinetics of Hybridization on Surface Oligonucleotide Microchips: Theory, Experiment, and Comparison with Hybridization on Gel-Based Microchips. *J. Biomol. Struct. Dyn.* **2006,** *24* (1), 57-66.

35. Charles, P. T.; Goldman, E. R.; Rangasammy, J. G.; Schauer, C. L.; Chen, M.-S.; Taitt, C. R., Fabrication and characterization of 3D hydrogel microarrays to measure antigenicity and antibody functionality for biosensor applications. *Biosens. Bioelectron.* **2004,** *20* (4), 753-764.

36. Wilkins Stevens, P.; Wang, C. H. J.; Kelso, D. M., Immobilized Particle Arrays:Coalescence of Planar- and Suspension-Array Technologies. *Anal. Chem.* **2003,** *75* (5), 1141-1146.

37. Pregibon, D.; Toner, M.; Doyle, P. S., Multifunctional encoded particles for high-throughput biomolecule analysis. *Science* **2007,** *315*, 1393-1396.

38. Guschin, D.; Yershov, G.; Zaslavsky, A.; Gemmell, A.; Shick, V.; Proudnikov, D.; Arenkov, P.; Mirzabekov, A., Manual Manufacturing of Oligonucleotide, DNA, and Protein Microchips. *Anal. Biochem.* **1997,** *250* (2), 203-211.

39. Moorthy, J.; Burgess, R.; Yethiraj, A.; Beebe, D., Microfluidic Based Platform for Characterization of Protein Interactions in Hydrogel Nanoenvironments. *Anal. Chem.* **2007,** *79* (14), 5322-5327.

40. Vasiliskov, V. A.; Prokopenko, D. V.; Mirzabekov, A. D., Parallel multiplex thermodynamic analysis of coaxial base stacking in DNA duplexes by oligodeoxyribonucleotide microchips. *Nucleic Acids Res.* **2001,** *29* (11), 2303-2313.

41. Rubina, A. Y.; Kolchinsky, A.; Makarov, A. A.; Zasedatelev, A. S., Why 3-D? Gel-based microarrays in proteomics. *Proteomics* **2008,** *8* (4), 817-831.

42. Zubtsov, D. A.; Savvateeva, E. N.; Rubina, A. Y.; Pan'kov, S. V.; Konovalova, E. V.; Moiseeva, O. V.; Chechetkin, V. R.; Zasedatelev, A. S., Comparison of surface and hydrogel-based protein microchips. *Anal. Biochem.* **2007,** *368* (2), 205-213.

43. Hwang, D. K.; Dendukuri, D.; Doyle, P. S., Microfluidic-based synthesis of non-spherical magnetic hydrogel microparticles. *Lab Chip* **2008,** *8* (10), 1640-1647.

44. Decker, C., Photoinitiated Crosslinking Polymerisation. *Prog. Polym. Sci.* **1996,** *21* (4), 593-650.

45. Decker, C., The Use of UV Irradiation in Polymerization. *Polymer International* **1998,** *45* (2), 133-141.

46. Dendukuri, D.; Panda, P.; Haghgooie, R.; Kim, J. M.; Hatton, T. A.; Doyle, P. S., Modeling of Oxygen-Inhibited Free Radical Photopolymerization in a PDMS Microfluidic Device. *Macromolecules* **2008,** *41* (22), 8547-8556.

47. Odian, G., *Principles of Polymerization*. 4th ed.; John Wiley & Sons Inc.: Hoboken, 2004.

48. Decker, C.; Jenkins, A. D., Kinetic Approach of Oxygen Inhibition in Ultraviolet- and Laser-induced Polymerizations. *Macromolecules* **1985,** *18* (6), 1241-1244.

49. Bartolo, D.; Degre, G.; Nghe, P.; Studer, V., Microfluidic Stickers. *Lab Chip* **2008,** *8* (2), 274-279.

50. Goodner, M. D.; Bowman, C. N., Development of a comprehensive free radical photopolymerization model incorporating heat and mass transfer effects in thick films. *Chem. Eng. Sci.* **2002,** *57* (5), 887-900.

51. Lee, J. H.; Prud'homme, R. K.; Aksay, I. A., Cure depth in photopolymerization: Experiments and theory. *J. Mater. Res.* **2001,** *16* (12), 3536-3544.

52. Biswal, D.; Hilt, J. Z., Analysis of Oxygen Inhibition in Photopolymerizations of Hydrogel Micropatterns Using FTIR Imaging. *Macromolecules* **2009,** *42* (4), 973-979.

53. O'Brien, A. K.; Bowman, C. N., Impact of Oxygen on Photopolymerization Kinetics and Polymer Structure. *Macromolecules* **2006,** *39* (7), 2501-2506.

54. O'Brien, A. K.; Bowman, C. N., Modeling the Effect of Oxygen on Photopolymerization Kinetics. *Macromol. Theory Simul.* **2006,** *15* (2), 176-182.

55. Kim, D.-N.; Lee, W.; Koh, W.-G., Preparation of protein microarrays on non-fouling and hydrated poly(ethylene glycol) hydrogel substrates using photochemical surface modification. *J. Chem. Technol. Biotechnol.* **2009,** *84* (2), 279-284.

56. Sigma_Aldrich. Product Image. www.sigmaaldrich.com.

57. IDT_Technologies. http://www.idtdna.com/.

58. Decker, C.; Decker, D., Photoinitiated radical polymerization of vinyl ether-maleate systems. *Polymer* **1997,** *38* (9), 2229-2237.

59. Decker, C.; Moussa, K., Kinetic investigation of photopolymerizations induced by laser beams. *Makromol. Chem.* **1990,** *191* (4), 963-979.

60. Leprince, J. G.; Lamblin, G.; Devaux, J.; Dewaele, M.; Mestdagh, M.; Palin, W. M.; Gallez, B.; Leloup, G., Irradiation Modes' Impact on Radical Entrapment in Photoactive Resins. *J. Dent. Res.* **2010,** *89* (12), 1494-1498.

61. Sivergin, Y.; Ismailov, R.; Gaisin, F.; Usmanov, S., Simulation of the formation of a single three-dimensional structural unit in free-radical polymerization. *Polymer Science Series A* **2008,** *50* (1), 91-99.

62. Zhu, S.; Tian, Y.; Hamielec, A. E.; Eaton, D. R., Radical concentrations in free radical copolymerization of MMA/EGDMA. *Polymer* **1990,** *31* (1), 154-159.

63. IDT_Technologies. Strategies for Attaching Oligonucleotides to Solid Supports. http://www.idtdna.com/.

64. Kenney, M.; Ray, S.; Boles, T. C., Mutation Typing Using Electrophoresis and Gel-Immobilized Acrydite™ Probes. *BioTechniques* **1998,** *25* (3), 516-521.

65. Rehman, F. N.; Audeh, M.; Abrams, E. S.; Hammond, P. W.; Kenney, M.; Boles, T. C., Immobilization of acrylamide-modified oligonucleotides by co-polymerization. *Nucleic Acids Res.* **1999,** *27* (2), 649-655.

66. Anseth, K. S.; Wang, C. M.; Bowman, C. N., Reaction behaviour and kinetic constants for photopolymerizations of multi(meth)acrylate monomers. *Polymer* **1994,** *35* (15), 3243-3250.

67. Pregibon, D. C.; Doyle, P. S., Optimization of Encoded Hydrogel Particles for Nucleic Acid Quantification. *Anal. Chem.* **2009,** *81* (12), 4873-4881.

68. Jiang, Y.; Rabbi, M.; Kim, M.; Ke, C.; Lee, W.; Clark, R. L.; Mieczkowski, P. A.; Marszalek, P. E., UVA Generates Pyrimidine Dimers in DNA Directly. *Biophys. J.* **2009,** *96* (3), 1151-1158.

69. Steinmetz, N. F.; Evans, D. J., Utilisation of plant viruses in bionanotechnology. *Org. Biomol. Chem.* **2007,** *5* (18), 2891-2902.

70. Douglas, T.; Young, M., Viruses: Making Friends with Old Foes. *Science* **2006,** *312* (5775), 873-875.

71. Lee, L. A.; Wang, Q., Adaptations of nanoscale viruses and other protein cages for medical applications. *Nanomedicine: NBM* **2006,** *2* (3), 137.

72. Fischlechner, M.; Donath, E., Viruses as building blocks for materials and devices. *Angew. Chem., Int. Ed.* **2007,** *46* (18), 3184-3193.

73. Fischlechner, M.; Toellner, L.; Messner, P.; Grabherr, R.; Donath, E., Virus-Engineered Colloidal Particles-A Surface Display System. *Angew. Chem., Int. Ed.* **2006,** *45* (5), 784-789.

74. Douglas, T.; Young, M., Virus particles as templates for materials synthesis. *Adv. Mater.* **1999,** *11* (8), 679-310.

75. Manchester, M.; Singh, P., Virus-based nanoparticles (VNPs): Platform technologies for diagnostic imaging. *Adv. Drug Delivery Rev.* **2006,** *58* (14), 1505.

76. Merzlyak, A.; Lee, S.-W., Phage as templates for hybrid materials and mediators for nanomaterial synthesis. *Curr. Opin. Chem. Biol.* **2006,** *10* (3), 246.

77. Singh, P.; Gonzalez, M. J.; Manchester, M., Viruses and their uses in nanotechnology. *Drug Dev. Res.* **2006,** *67* (1), 23-41.

78. Gazit, E., Use of biomolecular templates for the fabrication of metal nanowires. *FEBS J.* **2007,** *274* (2), 317-322.

79. Dujardin, E.; Peet, C.; Stubbs, G.; Culver, J. N.; Mann, S., Organization of metallic nanoparticles using tobacco mosaic virus templates. *Nano Lett.* **2003,** *3* (3), 413-417.

80. Fowler, C. E.; Shenton, W.; Stubbs, G.; Mann, S., Tobacco mosaic virus liquid crystals as templates for the interior design of silica mesophases and nanoparticles. *Adv. Mater.* **2001,** *13* (16), 1266-1269.

81. Niu, Z. W.; Bruckman, M. A.; Li, S. Q.; Lee, L. A.; Lee, B.; Pingali, S. V.; Thiyagarajan, P.; Wang, Q., Assembly of tobacco mosaic virus into fibrous and macroscopic bundled arrays mediated by surface aniline polymerization. *Langmuir* **2007,** *23* (12), 6719-6724.

82. Balci, S.; Noda, K.; Bittner, A. M.; Kadri, A.; Wege, C.; Jeske, H.; Kern, K., Self-assembly of metal-virus nanodumbbells. *Angew. Chem., Int. Ed.* **2007,** *46* (17), 3149-3151.

83. Huang, Y.; Chiang, C. Y.; Lee, S. K.; Gao, Y.; Hu, E. L.; Yoreo, J. D.; Belcher, A. M., Programmable Assembly of Nanoarchitectures Using Genetically Engineered Viruses. *Nano Lett.* **2005,** *5* (7), 1429-1434.

84. Yoo, P. J.; Nam, K. T.; Qi, J.; Lee, S.-K.; Park, J.; Belcher, A. M.; Hammond, P. T., Spontaneous assembly of viruses on multilayered polymer surfaces. *Nat. Mater.* **2006,** *5* (3), 234.

85. Chiang, C. Y.; Mello, C. M.; Gu, J.; Silva, E.; Van Vliet, K.; Belcher, A., Weaving Genetically Engineered Functionality into Mechanically Robust Virus Fibers. *Adv. Mater.* **2007,** *19,* 826-832.

86. Steinmetz, N. F.; Findlay, K. C.; Noel, T. R.; Parker, R.; Lomonossoff, G., P.; Evans, D. J., Layer-By-Layer Assembly of Viral Nanoparticles and Polyelectrolytes: The Film Architecture is Different for Spheres Versus Rods. *ChemBioChem* **2008,** *9,* 1662-1670.

87. Klem, M. T.; Young, M.; Douglas, T., Biomimetic synthesis of β-TiO2 inside a viral capsid. *J. Mater. Chem.* **2008,** *18* (32), 3821-3823.

88. Sapsford, K. E.; Soto, C. M.; Blum, A. S.; Chatterji, A.; Lin, T.; Johnson, J. E.; Ligler, F. S.; Ratna, B. R., A cowpea mosaic virus nanoscaffold for multiplexed antibody conjugation: Application as an immunoassay tracer. *Biosens. Bioelectron.* **2006,** *21* (8), 1668-1673.

89. Hooker, J. M.; Kovacs, E. W.; Francis, M. B., Interior Surface Modification of Bacteriophage MS2. *J. Am. Chem. Soc.* **2004,** *126* (12), 3718-3719.

90. Huang, Y.; Chiang, C.-Y.; Lee, S. K.; Gao, Y.; Hu, E. L.; Yoreo, J. D.; Belcher, A. M., Programmable Assembly of Nanoarchitectures Using Genetically Engineered Viruses. *Nano Lett.* **2005,** *5* (7), 1429-1434.

91. Avery, K. N.; Schaak, J. E.; Schaak, R. E., M13 Bacteriophage as a Biological Scaffold for Magnetically-Recoverable Metal Nanowire Catalysts: Combining Specific and Nonspecific Interactions To Design Multifunctional Nanocomposites. *Chem. Mater.* **2009,** *21* (11), 2176-2178.

92. Miller, R. A.; Presley, A. D.; Francis, M. B., Self-Assembling Light-Harvesting Systems from Synthetically Modified Tobacco Mosaic Virus Coat Proteins. *J. Am. Chem. Soc.* **2007,** *129* (11), 3104-3109.

93. Knez, M.; Sumser, M.; Bittner, A. M.; Wege, C.; Jeske, H.; Martin, T. P.; Kern, K., Spatially Selective Nucleation of Metal Clusters on the Tobacco Mosaic Virus. *Adv. Funct. Mater.* **2004,** *14* (2), 116-124.

94. Niu, Z.; Liu, J.; Lee, L. A.; Bruckman, M. A.; Zhao, D.; Koley, G.; Wang, Q., Biological Templated Synthesis of Water-Soluble Conductive Polymeric Nanowires. *Nano Lett.* **2007,** *7* (12), 3729-3733.

95. Abedin, M. J.; Liepold, L.; Suci, P.; Young, M.; Douglas, T., Synthesis of a Cross-Linked Branched Polymer Network in the Interior of a Protein Cage. *J. Am. Chem. Soc.* **2009,** *131* (12), 4346-4354.

96. Plascencia-Villa, G.; Saniger, J. M.; Ascencio, J. A.; Palomares, L. A.; Ramírez, O. T., Use of recombinant rotavirus VP6 nanotubes as a

multifunctional template for the synthesis of nanobiomaterials functionalized with metals. *Biotechnol. Bioeng.* **2009,** *104* (5), 871-881.

97. Manchester, M.; Steinmetz, N. F.; Strable, E.; Finn, M. G., Chemical Modification of Viruses and Virus-Like Particles. In *Viruses and Nanotechnology*, Springer Berlin Heidelberg: 2009; Vol. 327, pp 1-21.

98. Smolenska, L.; Roberts, I. M.; Learmonth, D.; Porter, A. J.; Harris, W. J.; Wilson, T. M. A.; Santa Cruz, S., Production of a functional single chain antibody attached to the surface of a plant virus. *FEBS Lett.* **1998,** *441* (3), 379.

99. Schwyzer, R.; Kriwaczek, V. M., Tobacco mosaic virus as a carrier for small molecules: Artificial receptor antibodies and superhormones. *Biopolymers* **1981,** *20* (9), 2011-2020.

100. Werner, S.; Marillonnet, S.; Hause, G.; Klimyuk, V.; Gleba, Y., Immunoabsorbent Nanoparticles Based on a Tobamovirus Displaying Protein A. *Proc. Natl. Acad. Sci. U. S. A.* **2006,** *103* (47), 17678-17683.

101. Soto, C. M.; Blum, A. S.; Vora, G. J.; Lebedev, N.; Meador, C. E.; Won, A. P.; Chatterji, A.; Johnson, J. E.; Ratna, B. R., Fluorescent Signal Amplification of Carbocyanine Dyes Using Engineered Viral Nanoparticles. *J. Am. Chem. Soc.* **2006,** *128* (15), 5184-5189.

102. Culver, J. N., Tobacco mosaic virus assembly and disassembly: Determinants in pathogenicity and resistance. *Annu. Rev. Phytopathol.* **2002,** *40*, 287-310.

103. Zaitlin, M., Tobacco mosaic virus. *AAB Descriptions of Plant Viruses* **2000,** *370*.

104. Klug, A., The tobacco mosaic virus particle: structure and assembly. *Philos. Trans. R. Soc., B* **1999,** *354* (1383), 531-535.

105. Lebeurier, G.; Nicolaieff, A.; Richards, K. E., Inside-Out Model for Self-Assembly of Tobacco Mosaic Virus. *Proc. Natl. Acad. Sci. U. S. A.* **1977,** *74* (1), 149-153.

106. Namba, K.; Stubbs, G., Structure of Tobacco Mosaic Virus at 3.6A Resolution - Implications for Assembly. *Science* **1986,** *231* (4744), 1401-1406.

107. Knez, M.; Sumser, M.; Bittner, A. M.; Wege, C.; Jeske, H.; Martin, T. P.; Kern, K., Spatially selective nucleation of metal clusters on the tobacco mosaic virus. *Advanced Functional Materials* **2004,** *14* (2), 116-124.

108. Stubbs, G., *Semin. Virol.* **1990,** *1*, 405-412.

109. Lee, S.-Y.; Lim, J. S.; Culver, J. N.; Harris, M. T., Coagulation of tobacco mosaic virus in alcohol-water-LiCl solutions. *J. Colloid Interface Sci.* **2008,** *324* (1-2), 92-98.

110. Dawson, W. O.; Beck, D. L.; Knorr, D. A.; Grantham, G. L., cDNA Cloning of the Complete Genome of Tobacco Mosaic Virus and Production of Infectious Transcripts. *Proc. Natl. Acad. Sci. U. S. A.* **1986,** *83* (6), 1832-1836.

111. Liu, W. L.; Alim, K.; Balandin, A. A.; Mathews, D. M.; Dodds, J. A., Assembly and characterization of hybrid virus-inorganic nanotubes. *Appl. Phys. Lett.* **2005,** *86* (25), 253108-3.

112. Fonoberov, V. A.; Balandin, A. A., Phonon Confinement Effects in Hybrid Virus-Inorganic Nanotubes for Nanoelectronic Applications. *Nano Lett.* **2005,** *5* (10), 1920-1923.

113. Tseng, R. J.; Tsai, C.; Ma, L.; Ouyang, J.; Ozkan, C. S.; Yang, Y., Digital memory device based on tobacco mosaic virus conjugated with nanoparticles. *Nat. Nanotechnol.* **2006,** *1* (1), 72-77.

114. Royston, E.; Ghosh, A.; Kofinas, P.; Harris, M. T.; Culver, J. N., Self-Assembly of Virus-Structured High Surface Area Nanomaterials and Their Application as Battery Electrodes. *Langmuir* **2008,** *24* (3), 906-912.

115. Chen, X.; Gerasopoulos, K.; Guo, J.; Brown, A.; Wang, C.; Ghodssi, R.; Culver, J. N., Virus-Enabled Silicon Anode for Lithium-Ion Batteries. *ACS Nano* **2010,** *4* (9), 5366-5372.

116. Bruckman, M. A.; Kaur, G.; Lee, L. A.; Xie, F.; Sepulveda, J.; Breitenkamp, R.; Zhang, X.; Joralemon, M.; Russell, T. P.; Emrick, T.; Wang, Q., Surface Modification of Tobacco Mosaic Virus with ldquoClickrdquo Chemistry. *ChemBioChem* **2008,** *9* (4), 519-523.

117. Lee, S.-Y.; Roysten, E.; Culver, J. N.; Harris, M. T., Improved metal cluster deposition on a genetically engineered tobacco mosaic virus template. *Nanotechnology* **2005,** *16* (7), S435-S441.

118. Thermo_Scientific. Chemistry of Crosslinking. www.piercenet.com/proteomics.

119. Thermo_Scientific. Fluorescein-5-maleimide, Product 46130 Instructions. www.thermo.com/pierce.

120. Rogers, K., Principles of affinity-based biosensors. *Mol. Biotechnol.* **2000,** *14* (2), 109-129.

121. Aldaye, F. A.; Palmer, A. L.; Sleiman, H. F., Assembling Materials with DNA as the Guide. *Science* **2008,** *321* (5897), 1795-1799.

122. Feldkamp, U.; Niemeyer, C. M., Rational Design of DNA Nanoarchitectures. *Angew. Chem., Int. Ed.* **2006,** *45* (12), 1856-1876.

123. Lin, C.; Liu, Y.; Rinker, S.; Yan, H., DNA Tile Based Self-Assembly: Building Complex Nanoarchitectures. *ChemPhysChem* **2006,** *7* (8), 1641-1647.

124. Lin, C.; Liu, Y.; Yan, H., Designer DNA Nanoarchitectures. *Biochemistry* **2009,** *48* (8), 1663-1674.

125. Tanaka, K.; Shionoya, M., Bio-Inspired Programmable Self-Assembly on DNA Templates. *Chem. Lett.* **2006,** *35* (7), 694-699.

126. Shih, W. M.; Lin, C., Knitting complex weaves with DNA origami. *Curr. Opin. Struct. Biol.* **2010,** *20* (3), 276-282.

127. Fiorini, C.; Charra, F., Self-assembly: mastering photonic processes at nanoscale. *Opto-Electron. Rev.* **2010,** *18* (4), 376-383.

128. Boozer, C.; Ladd, J.; Chen, S.; Yu, Q.; Homola, J.; Jiang, S., DNA Directed Protein Immobilization on Mixed ssDNA/Oligo(ethylene glycol) Self-Assembled Monolayers for Sensitive Biosensors. *Anal. Chem.* **2004,** *76* (23), 6967-6972.

129. Wang, Z.; Lu, Y., Functional DNA directed assembly of nanomaterials for biosensing. *J. Mater. Chem.* **2009,** *19* (13), 1788-1798.

130. Endo, M.; Hidaka, K.; Kato, T.; Namba, K.; Sugiyama, H., DNA Prism Structures Constructed by Folding of Multiple Rectangular Arms. *J. Am. Chem. Soc.* **2009,** *131* (43), 15570-15571.

131. Chomski, E.; Ozin, G., Panoscopic Silicon-A Material for "All" Length Scales. *Adv. Mater.* **2000,** *12* (14), 1071-1078.

132. Correia, A.; Perez, M.; Saenz, J. J.; Serena, P. A., Nanotechnology applications: a driving force for R&D investment. *Phys. Status Solidi A.* **2007,** *204*, 1611-1622.

133. Lehn, J.-M., Toward Self-Organization and Complex Matter. *Science* **2002,** *295* (5564), 2400-2403.

134. Ozin, G. A., Panoscopic materials: synthesis over all length scales. *Chem. Commun.* **2000**, 419-432.

135. Ungar, G.; Liu, Y.; Zeng, X.; Percec, V.; Cho, W.-D., Giant Supramolecular Liquid Crystal Lattice. *Science* **2003,** *299* (5610), 1208-1211.

136. Zuo, L.; Wei, W.; Morris, M.; Wei, J.; Gorbounov, M.; Wei, C., New Technology and Clinical Applications of Nanomedicine. *Med. Clin. N. Am.* **2007,** *91* (5), 845.

137. Whitesides, G. M.; Grzybowski, B., Self-Assembly at All Scales. *Science* **2002,** *295* (5564), 2418-2421.

138. Lakes, R., Materials with Structural Hierarchy. *Nature* **1993,** *361*, 511-515.

139. Sanchez, C.; Arribart, H.; Giraud Guille, M. M., Biomimetism and bioinspiration as tools for the design of innovative materials and systems. *Nat. Mater.* **2005,** *4* (4), 277-288.

140. Scheck, R. A.; Francis, M. B., Regioselective Labeling of Antibodies through N-Terminal Transamination. *ACS Chem. Biol.* **2007,** *2* (4), 247-251.

141. Tan, W. S.; Lewis, C. L.; Horelik, N. E.; Pregibon, D. C.; Doyle, P. S.; Yi, H., Hierarchical Assembly of Viral Nanotemplates with Encoded Microparticles via Nucleic Acid Hybridization. *Langmuir* **2008,** *24* (21), 12483-12488.

142. Rasband, W. S., ImageJ. In *http://rsb.info.nih.gov/ij/*, U.S. National Institutes of Health: Bethesda, Maryland, USA, 1997-2009.

143. Couch, G. S.; Hendrix, D. K.; Ferrin, T. E., Nucleic acid visualization with UCSF Chimera. *Nucleic Acids Res.* **2006,** *34* (4), e29.

144. Goddard, T. D.; Huang, C. C.; Ferrin, T. E., Software Extensions to UCSF Chimera for Interactive Visualization of Large Molecular Assemblies. *Structure* **2005,** *13* (3), 473-482.

145. Pettersen, E. F.; Goddard, T. D.; Huang, C. C.; Couch, G. S.; Greenblatt, D. M.; Meng, E. C.; Ferrin, T. E., UCSF Chimera - A visualization System for Exploratory Research and Analysis. *J. Comput. Chem.* **2004,** *25*, 1605-1612.

146. Namba, K.; Pattanayek, R.; Stubbs, G., Visualization of protein-nucleic acid interactions in a virus : Refined structure of intact tobacco mosaic virus at 2.9 A resolution by X-ray fiber diffraction. *J. Mol. Biol.* **1989,** *208* (2), 307-325.

147. Berman, H. M.; Westbrook, J.; Feng, Z.; Gilliland, G.; Bhat, T. N.; Weissig, H.; Shindyalov, I. N.; Bourne, P. E., The Protein Data Bank. *Nucleic Acids Res.* **2000,** *28* (1), 235-242.

148. Schmatulla, A.; Maghelli, N.; Marti, O., Micromechanical properties of tobacco mosaic viruses. *Journal of Microscopy-Oxford* **2007,** *225* (3), 264-268.

149. Tseng, R. J.; Tsai, C.; Ma, L.; Ouyang, J.; Ozkan, C. S.; Yang, Y., Digital memory device based on tobacco mosaic virus conjugated with nanoparticles. *Nat Nano* **2006,** *1* (1), 72-77.

150. Kalinin, S. V.; Jesse, S.; Liu, W.; Balandin, A. A., Evidence for possible flexoelectricity in tobacco mosaic viruses used as nanotemplates. *Applied Physics Letters* **2006,** *88* (15), 153902-3.

151. Yang, C.; Manocchi, A. K.; Lee, B.; Yi, H., Viral templated palladium nanocatalysts for dichromate reduction. *Appl. Catal., B* **2010,** *93* (3-4), 282-291.

152. Gerasopoulos, K.; McCarthy, M.; Banerjee, P.; Fan, X.; Culver, J. N.; Ghodssi, R., Biofabrication methods for the patterned assembly and synthesis of viral nanotemplates. *Nanotechnology* **2010,** *21* (5), 11.

153. Kuncicky, Daniel M.; Naik, Rajesh R.; Velev, Orlin D., Rapid Deposition and Long-Range Alignment of Nanocoatings and Arrays of Electrically Conductive Wires from Tobacco Mosaic Virus13. *Small* **2006,** *2* (12), 1462-1466.

154. Lin, Y.; Balizan, E.; Lee, L. A.; Niu, Z.; Wang, Q., Self-Assembly of Rodlike Bio-nanoparticles in Capillary Tubes13. *Angew. Chem., Int. Ed.* **2010,** *49* (5), 868-872.

155. Dendukuri, D.; Tsoi, K.; Hatton, T. A.; Doyle, P. S., Controlled Synthesis of Nonspherical Microparticles Using Microfluidics. *Langmuir* **2005,** *21* (6), 2113-2116.

156. Fujibayashi, T.; Okubo, M., Preparation and Thermodynamic Stability of Micron-Sized, Monodisperse Composite Polymer Particles of Disc-like Shapes by Seeded Dispersion Polymerization. *Langmuir* **2007,** *23* (15), 7958-7962.

157. Manocchi, A. K.; Horelik, N. E.; Lee, B.; Yi, H., Simple, Readily Controllable Palladium Nanoparticle Formation on Surface-Assembled Viral Nanotemplates. *Langmuir* **2010,** *26* (5), 3670-3677.

158. Lewis, C. L.; Lin, Y.; Yang, C.; Manocchi, A. K.; Yuet, K. P.; Doyle, P. S.; Yi, H., Microfluidic Fabrication of Hydrogel Microparticles Containing Functionalized Viral Nanotemplates. *Langmuir* **2010,** *26* (16), 13436-13441.

159. Gooding, G. V.; Hebert, T. T., A Simple Technique for Purification of Tobacco Mosaic Virus in Large Quantities. *Phytopathology* **1967,** *57* (11), 1285.

160. McDonald, J. C.; Duffy, D. C.; Anderson, J. R.; Chiu, D. T.; Wu, H.; Schueller, O. J. A.; Whitesides, G. M., Fabrication of microfluidic systems in poly(dimethylsiloxane). *Electrophoresis* **2000,** *21* (1), 27-40.

161. Vincent, T.; Guibal, E., Chitosan-Supported Palladium Catalyst. 1. Synthesis Procedure. *Ind. Eng. Chem. Res.* **2002,** *41* (21), 5158-5164.

162. Christopher, G. F.; Anna, S. L., Microfluidic methods for generating continuous droplet streams. *J. Phys. D: Appl. Phys.* **2007,** *40* (19), R319-R336.

163. Manocchi, A. K.; Seifert, S.; Lee, B.; Yi, H., On the Thermal Stability of Surface-Assembled Viral-Metal Nanoparticle Complexes. *Langmuir* **2010,** *26* (10), 7516-7522.

164. Lewis, C. L.; Choi, C.-H.; Lin, Y.; Lee, C.-S.; Yi, H., Fabrication of Uniform DNA-Conjugated Hydrogel Microparticles via Replica Molding for Facile Nucleic Acid Hybridization Assays. *Anal. Chem.* **2010,** *82* (13), 5851-5858.

165. Yi, H.; Wu, L.-Q.; Ghodssi, R.; Rubloff, G. W.; Payne, G. F.; Bentley, W. E., A Robust Technique for Assembly of Nucleic Acid Hybridization Chips Based on Electrochemically Templated Chitosan. *Anal. Chem.* **2003,** *76* (2), 365-372.

166. McHale, G.; Rowan, S. M.; Newton, M. I.; Banerjee, M. K., Evaporation and the Wetting of a Low-Energy Solid Surface. *J. Phys. Chem. B* **1998,** *102* (11), 1964-1967.

167. Berthier, E.; Warrick, J.; Yu, H.; Beebe, D. J., Managing evaporation for more robust microscale assays. Part 1: Volume loss in high throughput assays. *Lab Chip* **2008,** *8* (6), 852-859.

168. Jackman, R. J.; Duffy, D. C.; Ostuni, E.; Willmore, N. D.; Whitesides, G. M., Fabricating Large Arrays of Microwells with Arbitrary Dimensions and Filling Them Using Discontinuous Dewetting. *Anal. Chem.* **1998,** *70* (11), 2280-2287.

169. Warrick, A. W.; Broadbridge, P.; Lomen, D. O., Approximations for diffusion from a disc source. *Applied Mathematical Modelling* **1992,** *16* (3), 155-161.

170. Mills, J. B.; Vacano, E.; Hagerman, P. J., Flexibility of single-stranded DNA: use of gapped duplex helices to determine the persistence lengths of Poly(dT) and Poly(dA). *J. Mol. Biol.* **1999,** *285* (1), 245-257.

171. Murphy, M. C.; Rasnik, I.; Cheng, W.; Lohman, T. M.; Ha, T., Probing Single-Stranded DNA Conformational Flexibility Using Fluorescence Spectroscopy. *Biophys. J.* **2004,** *86* (4), 2530-2537.

172. Olson, W. K., Configurational Statistics of Polynucleotide Chains. A Single Virtual Bond Treatment. *Macromolecules* **1975,** *8* (3), 272-275.

173. Smith, S. B.; Cui, Y.; Bustamante, C., Overstretching B-DNA: The Elastic Response of Individual Double-Stranded and Single-Stranded DNA Molecules. *Science* **1996,** *271* (5250), 795-799.

174. Cruise, G. M.; Scharp, D. S.; Hubbell, J. A., Characterization of permeability and network structure of interfacially photopolymerized poly(ethylene glycol) diacrylate hydrogels. *Biomaterials* **1998,** *19* (14), 1287-1294.

175. Mellott, M. B.; Searcy, K.; Pishko, M. V., Release of protein from highly cross-linked hydrogels of poly(ethylene glycol) diacrylate fabricated by UV polymerization. *Biomaterials* **2001,** *22* (9), 929-941.

176. Yershov, G.; Barsky, V.; Belgovskiy, A.; Kirillov, E.; Kreindlin, E.; Ivanov, I.; Parinov, S.; Guschin, D.; Drobishev, A.; Dubiley, S.; Mirzabekov, A., DNA analysis and diagnostics on oligonucleotide microchips. *Proc. Natl. Acad. Sci. U. S. A.* **1996,** *93* (10), 4913-4918.

177. Stevens, P. W.; Henry, M. R.; Kelso, D. M., DNA hybridization on microparticles: Determining capture-probe density and equilibrium dissociation constants. *Nucleic Acids Res.* **1999,** *27* (7), 1719-1727.

178. Revzin, A.; Russell, R. J.; Yadavalli, V. K.; Koh, W.-G.; Deister, C.; Hile, D. D.; Mellott, M. B.; Pishko, M. V., Fabrication of Poly(ethylene glycol) Hydrogel Microstructures Using Photolithography. *Langmuir* **2001,** *17* (18), 5440-5447.

179. Xu, S.; Nie, Z.; Seo, M.; Lewis, P.; Kumacheva, E.; Stone, H. A.; Garstecki, P.; Weibel, D. B.; Gitlin, I.; Whitesides, G. M., Generation of Monodisperse Particles by Using Microfluidics: Control over Size, Shape, and Composition13. *Angew. Chem., Int. Ed.* **2005,** *44* (5), 724-728.